Dissertations, Master's Theses and Master's Reports

2016

FIRST-PRINCIPLES STUDIES OF GROUP IV AND GROUP V RELATED TWO DIMENSIONAL MATERIALS

Gaoxue Wang
Michigan Technological University, gaoxuew@mtu.edu

FIRST-PRINCIPLES STUDIES OF GROUP IV AND GROUP V RELATED

TWO DIMENSIONAL MATERIALS

By

Gaoxue Wang

A DISSERTATION

Submitted in partial fulfillment of the requirements for the degree of

DOCTOR OF PHILOSOPHY

In Physics

MICHIGAN TECHNOLOGICAL UNIVERSITY

2016

This dissertation has been approved in partial fulfillment of the requirements for the Degree of DOCTOR OF PHILOSOPHY in Physics.

Department of Physics

Dissertation Advisor: *Dr. Ravindra Pandey*

Committee Member: *Dr. Max Seel*

Committee Member: *Dr. Ranjit Pati*

Committee Member: *Dr. Loredana Valenzano*

Department Chair: *Dr. Ravindra Pandey*

Contents

List of Figures

List of Tables

Preface

This thesis is submitted in partial fulfillment of the requirements for Degree of Doctor of Philosophy in Physics. I have worked on applying density functional theory in exploring the electronic properties of novel 2D materials. All the work in the thesis was supervised by Prof. Ravindra Pandey in Department of Physics, and has been published in 10 peer reviewed papers. I conducted the calculations and analysis of the results. Prof. Ravindra Pandey and Prof. Shashi P Karna from Army Research Laboratory were also involved in the data analysis and manuscript revision.

The work on graphyne in Chapter 3 is reproduced from the paper (*Appl. Phys. Lett., 2014, 104, 213107*) with the permission of AIP Publishing.

The section 4.2 on adatoms decorated phosphorene in Chapter 4 is reproduced from the paper (*Appl. Phys. Lett.*, 2015, 106, 173104) with the permission of AIP Publishing.

The section 4.3 on strain engineering of phosphorene in Chapter 4 is reproduced from the paper (*Nanotechnology*, 2016, 27, 055701) with the permission of IOP Publishing.

The section 5.2 on phosphorene oxide in Chapter 5 is reproduced from the paper (*Nanoscale*, 2015, 7, 524-531) with the permission of The Royal Society of Chemistry.

The section 5.3 on degradation of phosphorene in Chapter 5 is reproduced from the paper (*2D Mater*, 2016, 3, 025011) with the permission of IOP Publishing.

Chapter 6 on antimonene is reproduced from the paper (*ACS Appl. Mater. Interfaces*, 2015, 7, 11490–11496) with the permission from American Chemical Society.

Chapter 7 on carbon phosphide monolayers is reproduced from the paper (*Nanoscale*, 2016, 8, 8819-8825) with the permission of The Royal Society of Chemistry.

Acknowledgements

Abstract

Two dimensional (2D) materials have been extensively studied due to their novel properties and technologically important applications. Especially, the discovery of graphene has stimulated an avalanche of investigations to exploit its novel properties for applications at nanoscale. In the post-silicon era, graphene has been widely regarded as the most promising building blocks for the electronic devices. However, its metallic nature together with sensitivity to the environment leads to somewhat limited scope of applications. A finite band gap in a material is known to be essential for the fabrication of devices such as transistors. Such a limitation associated with graphene has led to the exploration of 2D materials beyond graphene. My work in this thesis can be broadly classified into two parts. The first part is focused on exploring the properties of some new 2D materials that have been synthesized in experiments using *first-principles* calculations based on density functional theory. Specifically, the electronic properties of group IV monolayer graphyne and group V monolayer phosphorene, engineering of their properties with external strain and defects, and the oxidation and degradation of phosphorene in air are investigated. The second part is focused on computational design of new 2D materials that have not been synthesized in experiments yet. For example, the structure and stability of antimonene and carbon phosphide monolayers are studied. These theoretical investigations in the present thesis not only improve our understandings on the physics and chemistry of existing 2D materials, but also lead to the fabrication of novel 2D materials for future applications.

Chapter 1   Introduction

1.1.   Graphene and related 2D materials

It was long believed in history that crystals with a single layer of atoms would not exist because they are thermodynamically unstable [1-3]. The discovery of graphene, a one-atom-thick sheet of carbon atoms, by Konstantin Novoselov, Andre Geim and their colleagues in 2004 took the world by surprise [4]. Due to its fundamental importance and amazing properties such as flexible, transparent, stronger than steel, and more conductive than copper, graphene was immediately rising as a star in material science and condensed matter physics.

Table 1.1. 2D library summarized in 2013. (Reprinted with permission from reference [5]. Copyright 2013 Nature Publishing Group. See Appendix B for documentation of permission to republish this material.)

Graphene family	Graphene	hBN 'white graphene'		BCN	Fluorographene	Graphene oxide
2D chalcogenldes	MoS_2, WS_2, $MoSe_2$, WSe_2	Semiconducting dichalcogenides: $MoTe_2$, WTe_2, ZrS_2, $ZrSe_2$ and so on			Metallic dichalcogenides: $NbSe_2$, NbS_2, TaS_2, TiS_2, $NiSe_2$ and so on	
					Layered semiconductors: GaSe, GaTe, InSe, Bi_2Se_3 and so on	
2D oxides	Micas, BSCCO	MoO_3, WO_3	Perovskite-type: $LaNb_2O_7$, $(Ca,Sr)_2Nb_3O_{10}$, $Bi_4Ti_3O_{12}$, $Ca_2Ta_2TiO_{10}$ and so on			Hydroxides: $Ni(OH)_2$, $Eu(OH)_2$ and so on
	Layered Cu oxides	TiO_2, MnO_2, V_2O_5, TaO_3, RuO_2 and so on				Others

Soon after the discovery of graphene, it was assumed that graphene could replace silicon in modern electronic circuits [6]. However, the group IV elemental monolayers, including graphene, silicene and germanene [7], are not suitable for application in transistors due to the well-known 'switch-off' problem. They are found to be semi-metallic with zero band gaps, thus cannot be used to make

transistors with a perfect switch-off state. This limitation on group IV elemental monolayers has led to the exploration of new two dimensional (2D) materials that go beyond graphene [8].
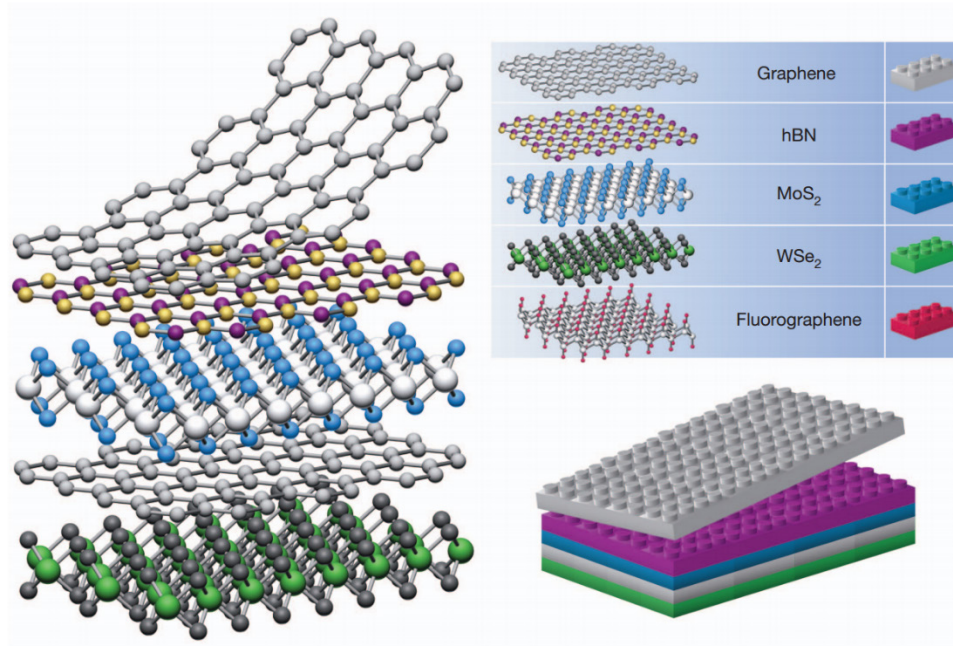
Figure 1.1 Building van der Waals heterostructures from 2D materials. (Reprinted with permission from reference [5]. Copyright 2013 Nature Publishing Group. See Appendix B for documentation of permission to republish this material.)

Hundreds of 2D materials have been discovered during the past decades [8]. Table 1.1 is a summary of some of them that have been reported up to 2013. These materials can exhibit unique and fascinating electronic, mechanical, and transport properties, thus enable the fabrication of electronic and optoelectronic devices. More interestingly, these 2D materials can be considered as Lego bricks. We can assemble these bricks together to design materials with completely different functionalities, known as the van der Waals heterostructures as illustrated in Figure 1.1 [5].

1.2.   Group V elemental monolayers
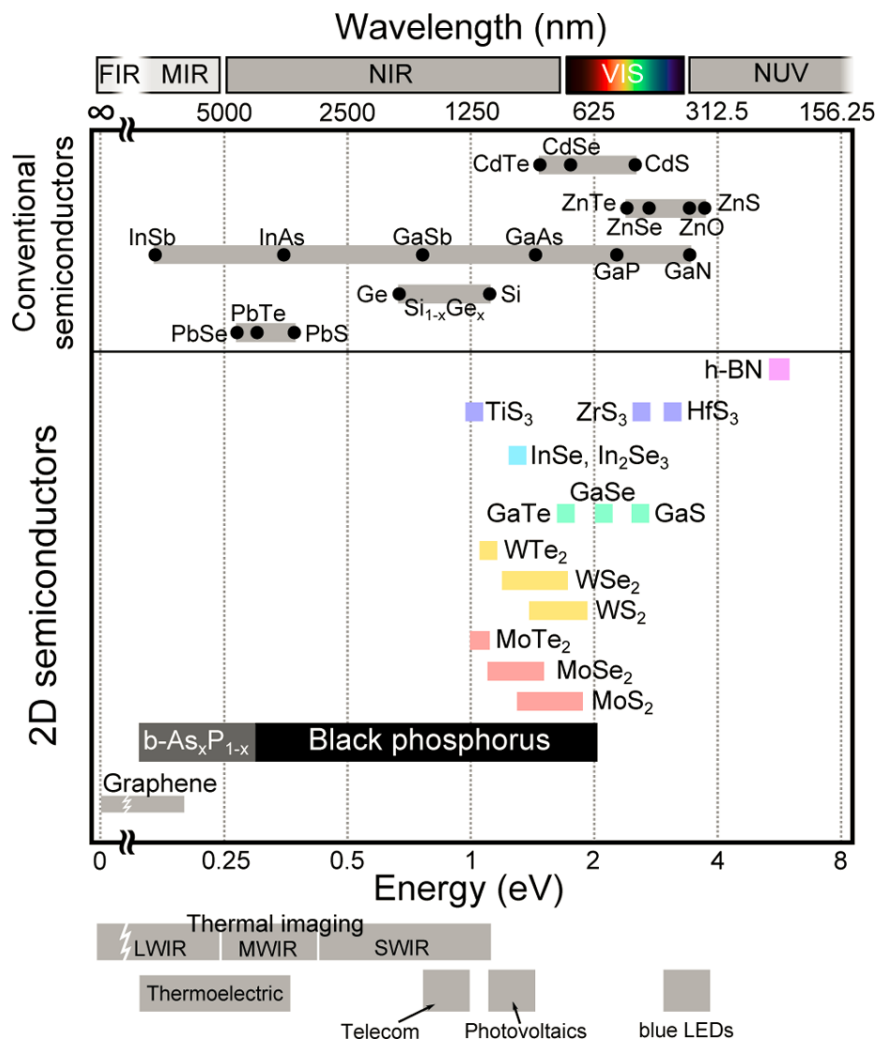
Figure 1.2 Comparison of the band gap values of a few 2D materials. (Reprinted with permission from reference [9]. Copyright 2015 American Chemical Society. See Appendix B for documentation of permission to republish this material.)

The group V elemental monolayers join the 2D material family since 2014. The monolayer form of black phosphorus, also known as phosphorene, has drawn considerable attention as a novel 2D semiconducting material with a fundamental band gap [10, 11]. Since the interlayer interaction in the bulk black phosphorus is dominated by the van der Waals forces, phosphorene could be obtained

3

by exfoliating from the bulk lattice. In fact, a few layer of phosphorene has been successfully isolated by mechanical or liquid exfoliation and exploited for applications in electronic devices [12, 13]. It has been demonstrated that phosphorene-based transistors possess a larger current on/off ratio compared to graphene-based transistors and higher charge mobility than MoS_2-based devices [14]. Furthermore, the tunable band gap [15, 16], directional dependent conductance [17], and fast photo-response have been predicted for phosphorene [18, 19], thereby inducing interest amongst scientists for its novel applications in devices at nanoscale [20, 21].

More importantly, as shown in Figure 1.2, the band gap values of black phosphorus related materials span a wide energy range from 0.3 eV in the bulk form to 2.0 eV in the monolayer, which is not covered by other 2D materials [9]. Thus, phosphorene bridges the gap between zero band gap material graphene and other semiconducting 2D materials [9]. This band gap range is particularly suitable for applications such as thermal imaging, thermoelectric and photovoltaic applications [9].

1.3.   Motivation of this thesis

Although large amounts of 2D materials have been discovered, the elemental monolayers are relatively rare. The discovered elemental monolayers include the group III element (B), the group IV elements (C, Si, Ge, Sn). The group V elemental monolayer, phosphorene, just joined the 2D materials family, its physical and chemical properties have not been fully understood. For example, previous experiments have demonstrated the degradation of phosphorene in air, however, the degradation mechanism has not been discussed due to the difficulties in characterizing the chemical processes at atomic level. In the meantime, considering the chemical similarity of elements belonging to the same group in the periodic table, it is natural to consider the other group V elemental monolayers such as monolayers of arsenic, antimony and bismuth. However, their

structure and electronic properties are still open due the challenges in the exfoliation in experiments.

Based on this background, the first motivation of this thesis is to explore group IV and group V related 2D elemental monolayers using *first-principles* calculations. Theoretical studies can be performed readily and can provide atomic level insights into the physics and chemistry of materials. Additionally, we will computationally design new 2D materials that have not been synthesized in experiments, and explore their stability and electronic properties. These theoretical studies will not only contribute to the interpretation of the experimental data, but also lead to the synthesis of new 2D materials for future applications.

Chapter 2   Computational methods

2.1.   Density functional theory (DFT)

Density functional theory (DFT) is an approximate practical method to get the ground state of a many-body system [22]. The number of publications related to DFT increases dramatically since 1990 (see Figure 2.1), and reaches more than 15,000 each year. The success of DFT roots in the availability of accurate exchange-correlation functional and sufficient computational resources since the past twenty years. In this section, some of the basic ideas and practical methods related to DFT are introduced.
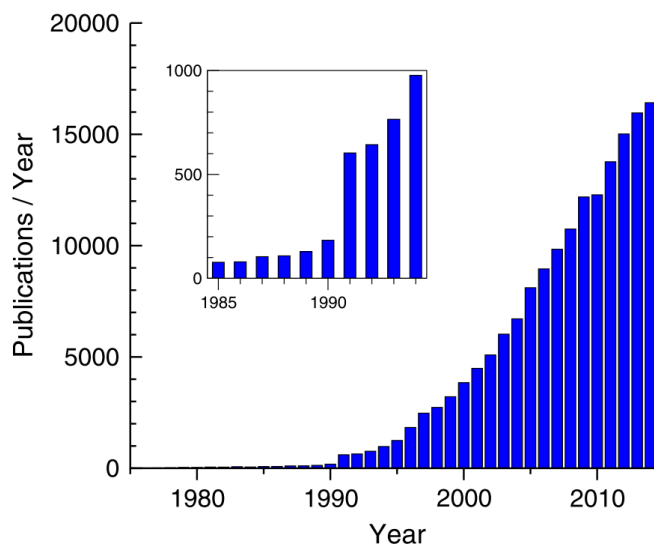
Figure 2.1 Number of publications per year (1975–2014) on topics of "density functional" or "DFT", according to the Web of Science Core Collection (February 2015). (Reprinted with permission from reference [22]. Copyright 2015 American Physical Society. See Appendix B for documentation of permission to republish this material.)

2.1.1. Schrödinger equation for many-body systems

Quantum mechanics is one of the most fundamental theory in physics that governs the motion of microparticles. To begin with, let's look at the time-independent Schrödinger equation for a many-body system with electrons and nuclei

$$H\Psi(\boldsymbol{r}) = E\Psi(\boldsymbol{r}), \tag{1.1}$$

H is the Hamiltonian for the many-body system,

$$H = -\frac{\hbar^2}{2m_e}\sum_i \nabla_i^2 - \sum_{i,I}\frac{Z_I e^2}{|\boldsymbol{r}_i - \boldsymbol{R}_I|} + \frac{1}{2}\sum_{i\neq j}\frac{e^2}{|\boldsymbol{r}_i - \boldsymbol{r}_j|} - \frac{\hbar^2}{2M_I}\sum_I \nabla_I^2 + \frac{1}{2}\sum_{I\neq J}\frac{Z_I Z_J e^2}{|\boldsymbol{R}_I - \boldsymbol{R}_J|}, \tag{1.2}$$

where the electrons are represented by lower case subscripts, and the nuclei are represented with upper case subscripts.

According to the Born-Oppenheimer/adiabatic approximation [23], the motion of nuclei and electrons can be decoupled due to the fact that nuclei are much heavier than electrons and they move much slowly than the electrons. The electrons can be considered to respond instantaneously to the motion of the nuclei. Thus, the Hamiltonian for the many-body system in Equation 1.2 could be decoupled into two parts [24]

$$H_e = -\frac{\hbar^2}{2m_e}\sum_i \nabla_i^2 + \frac{1}{2}\sum_{i\neq j}\frac{e^2}{|\boldsymbol{r}_i - \boldsymbol{r}_j|} - \sum_{i,I}\frac{Z_I e^2}{|\boldsymbol{r}_i - \boldsymbol{R}_I|}, \tag{1.3}$$

$$H_n = -\frac{\hbar^2}{2M_I}\sum_I \nabla_I^2 + U(\boldsymbol{R}), \tag{1.4}$$

where H_e is the Hamiltonian for the electrons, and H_n is the Hamiltonian for the nuclei. The total potential of the nuclei is defined as

$$U(\boldsymbol{R}) = \frac{1}{2}\sum_{I\neq J}\frac{Z_I Z_J e^2}{|\boldsymbol{R}_I - \boldsymbol{R}_J|} + E(\boldsymbol{R}), \tag{1.5}$$

where $E(R)$ is the total energy of the electrons within the set of coordinates R for the nuclei. The force on each nucleus can be calculated with

$$\boldsymbol{F}_I = M_I \frac{d^2 \boldsymbol{R}_I}{dt^2} = -\frac{\partial U}{\partial \boldsymbol{R}_I}. \qquad (1.6)$$

The equilibrium geometry of the nuclei is given by the condition that the force acting on individual nucleus is zero.

2.1.2. The Kohn-Sham equations

Due to the computational complexity of solving the many-body Schrödinger equation for a system with large amount of electrons, Paul Dirac made a famous announcement [25]

> "*The general theory of quantum mechanics is now almost complete,…*
>
> *The underlying physical laws necessary for the mathematical theory of*
>
> *a large part of physics and the whole of chemistry are thus completely*
>
> *known, and the difficulty is only that the exact application of these laws*
>
> *leads to equations much too complicated to be soluble. It therefore*
>
> *becomes desirable that approximate practical methods of applying*
>
> *quantum mechanics should be developed, which can lead to an*
>
> *explanation of the main features of complex atomic systems without too*
>
> *much computation.*"

As stated by Dirac, the difficulty of solving the many body Schrödinger equation lies in developing an 'approximate practical method' to get the wave functions and energy eigenvalues for complex systems, such as atoms, molecules and solids. To this end, density functional theory (DFT) was born, and it has now become a well-established tool in physics, chemistry and materials science.

8

The theoretical foundations of DFT were laid by Hohenberg, Kohn, and Sham in 1964 and 1965 [26, 27]. The Hohenberg-Kohn theorem I states that

> *For any system of interacting particles in an external potential $V_{ext}(\boldsymbol{r})$, the potential $V_{ext}(\boldsymbol{r})$ is uniquely determined by the ground state particle density $n_0(\boldsymbol{r})$.*

The Hohenberg-Kohn theorem II states that

> *A universal functional for the energy $E[n(\boldsymbol{r})]$ can be defined in terms of the density $n(\boldsymbol{r})$. The ground state energy of the system is the global minimum value of this functional, and the density that minimizes the functional is the exact ground state density $n_0(\boldsymbol{r})$.*

The Hohenberg-Kohn theorems describe the electron density as a basic variable, thus reduces a N-electron many-body problem with 3N spatial coordinates to a problem with only 3 spatial coordinates, and the ground state can be obtained by minimizing the total energy with respect to the density. However, the Hohenberg-Kohn theorems do not provide a prescription for calculating ground state density $n_0(\mathbf{r})$ of a system in practice.

$$V_{ext}(\boldsymbol{r}) \underset{}{\overset{HK}{\Longleftarrow}} n_0(\boldsymbol{r}) \underset{}{\overset{KS}{\Longleftrightarrow}} n_0(\boldsymbol{r}) \underset{}{\overset{HK}{\Longrightarrow}} v_{KS}(\boldsymbol{r})$$

$$\Downarrow \qquad \Uparrow \qquad \Uparrow \qquad \Downarrow$$

$$\Psi_i(\{\boldsymbol{r}\}) \Longrightarrow \Psi_0(\{\boldsymbol{r}\}) \qquad \psi_{i=1,Ne}(\boldsymbol{r}) \Longleftarrow \psi_i(\boldsymbol{r})$$
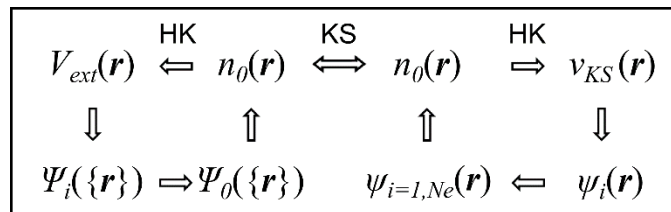
Figure 2.2 Schematic representation of Kohn-Sham ansatz.

A practical approach to obtain the ground state density was achieved by the *ansatz* made by Kohn and Sham in 1965 [27]. A schematic representation of the Kohn-Sham *ansatz* is given in Figure 2.2. According to Kohn-Sham *ansatz*, an auxiliary non-interacting system can be constructed to replace the interacting many-body system. The auxiliary system has the same ground state density as the original system, but the complexity in the equations for the original system is greatly reduced in the equations for the non-interacting system. One finds the ground state density and energy for the original system by solving the Kohn-Sham equations for the non-interacting system,

$$\left(-\frac{\hbar^2}{2m}\nabla^2 + v_{eff}\right)\psi_i(\boldsymbol{r}) = \varepsilon_i\psi_i(\boldsymbol{r}), \tag{1.7}$$

$$v_{eff} = v_{ext}(\boldsymbol{r}) + v_{Hartree}(\boldsymbol{r}) + v_{xc}(\boldsymbol{r}), \tag{1.8}$$

$$v_{ext} = -\sum_I \frac{Z_I}{|\boldsymbol{r}-\boldsymbol{R_Z}|}, \tag{1.9}$$

$$v_{Hartree} = \frac{\delta E_{Hartree}}{\delta n(r)}, \tag{1.10}$$

$$v_{xc} = \frac{\delta E_{xc}}{\delta n(r)}, \tag{1.11}$$

where $E_{ext}(\boldsymbol{r})$ is the potential energy due to the nuclei and any other external field, and $E_{Hartree}(\boldsymbol{r})$ is the Hartree energy which describes the classical Coulomb interaction of the electron density $n(\mathbf{r})$. The exact formula of $E_{ext}(\boldsymbol{r})$ and $E_{Hartree}(\boldsymbol{r})$ are already known, the only unknown term in the Kohn-Sham equations is the *exchange-correlation functional $E_{xc}(\boldsymbol{r})$*. If the universal functional $E_{xc}(\boldsymbol{r})$ were known, the exact ground state density and energy of the real interacting system can be obtained by solving the Kohn-Sham equations for the auxiliary non-interacting system.

Since a universal functional $E_{xc}(r)$ is unknown, different approximations have been proposed for $E_{xc}(r)$. These different flavors for $E_{xc}(r)$ form the well-known "Jacob's ladder" of density functional approximations as shown in Figure 2.3 [28]. Local density approximation (LDA) is the simplest form for the exchange-correlation functional, and it is the first rung of the Jacob's ladder. At this level of theory, it is assumed that the exchange-correlation energy density to be the same as a homogeneous electrons gas, and the exchange-correlation functional depends only on the density at the coordinate where the functional is evaluated

$$E_{xc}^{LDA} = \int \epsilon_{xc}^{hom}(n)n(r)\, d^3r. \tag{1.12}$$

The second rung of the Jacob's ladder is the generalized gradient approximation (GGA) which introduces the gradients of the density $\nabla n(r)$ as additional ingredients in the exchange-correlation functional

$$E_{xc}^{GGA} = \int \epsilon_{xc}^{GGA}(n, \nabla n)n(r)\, d^3r. \tag{1.13}$$

The third rung of the Jacob's ladder is meta-GGA which involves the Laplacian of the density ($\nabla^2 n(r)$), and/or the Kohn-Sham kinetic energy density ($\tau = \frac{1}{2}\sum_k^{occ} |\nabla\psi_k|^2$) [28]

$$E_{xc}^{MGGA} = \int \epsilon_{xc}^{MGGA}(n, \nabla n, \nabla^2 n(r), \tau)n(r)\, d^3r. \tag{1.14}$$

The fourth rung of the Jacob's ladder includes the exact exchange information, which are known as hybrid functionals. These functionals mix a fraction of Hartree-Fock exchange with a fraction of DFT exchange and full DFT correlation

$$E_{xc}^{HGGA} = \alpha E_x^{HF}[\{\psi_i\}] + (1-\alpha)E_x^{DFT} + E_c^{DFT}. \tag{1.15}$$

The fifth rung of the Jacob's ladder is the functional related to random phase approximation (RPA) which involves the unoccupied Kohn-Sham orbitals. This level of theory is not involved in the current work due to the huge computational costs.

HEAVEN OF CHEMICAL ACCURACY

unoccupied $\{\phi_i\}$		generalized RPA
ε_x		hyper-GGA
τ and/or $\nabla^2 n$		meta-GGA
∇n		GGA
n		LSD

HARTREE WORLD
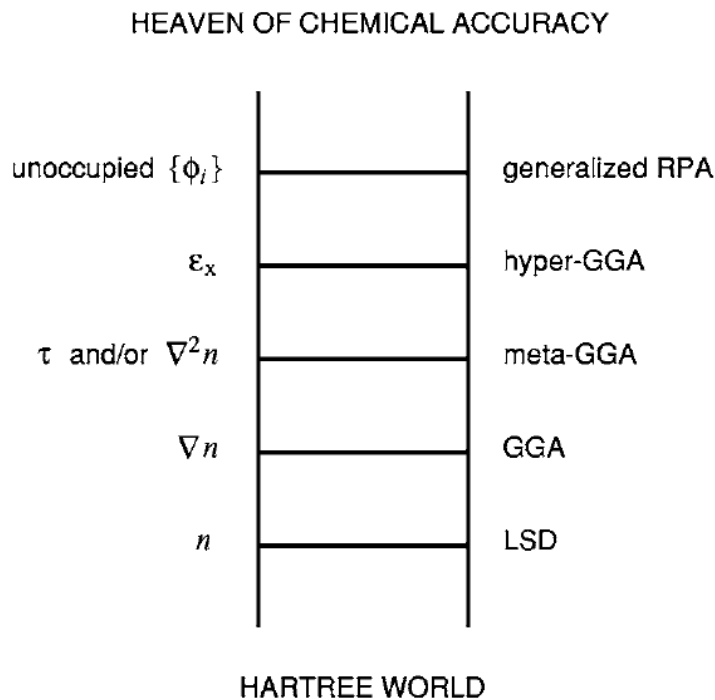
Figure 2.3 Jacob's ladder of density functional approximations to the exchange-correlation energy. (Reprinted with permission from reference [28]. Copyright 2005 AIP Publishing LLC. See Appendix B for documentation of permission to republish this material.)

The LDA/GGA is a local/semilocal functional of the density, which is computationally efficient for most calculations and is widely used for electronic structure calculations in material science, condensed mater physics, and quantum chemistry. The hybrid functional evolves the nonlocal exchange term, which is computationally more expensive than the LDA/GGA functional, but provides improvements on band gap values for most semiconductors. In this work, the LDA/GGA

functional is mainly used for the structure, stability and electronic property calculations. The hybrid

functional HSE06 [29] will be used to get the band gap values for a few 2D materials.

2.1.3. Self-consistent approach to the Kohn-sham equations

Initial Guess
$n(\mathbf{r})$

Calculate Effective Potential
$v_{eff} = v_{ext}(\mathbf{r}) + v_{Hartree}(\mathbf{r}) + v_{xc}(\mathbf{r})$

Solve Kohn-Sham Equations
$(-\frac{\hbar^2}{2m}\nabla^2 + v_{eff})\psi_i(\mathbf{r}) = \epsilon_i\psi_i(\mathbf{r})$

Evaluate the Electron Density and Total Energy
$n_0(\mathbf{r}) = \Sigma_i|\psi_i(\mathbf{r})|^2 \rightarrow E_{tot}[n(\mathbf{r})]$

Converged? No

Yes

Output Quantities
$n_0(\mathbf{r}), E_i[n_0(\mathbf{r})] \rightarrow$ Eigenvalues, Forces,...
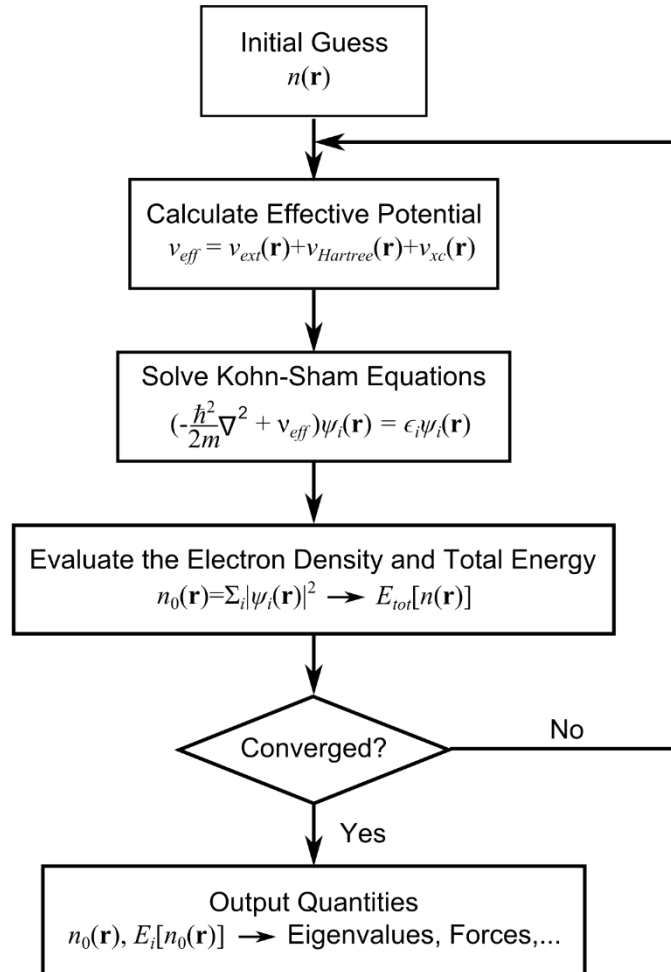
Figure 2.4 A flow chart of the self-consistent approach to solve the Kohn-Sham equations.

The Kohn-Sham equations are solved self-consistently as illustrated in Figure 2.4. One starts from

the initial guess for $n(\mathbf{r})$, for example, the superposition of atomic charge densities, to construct

the effective potential of the system. Then, the eigenvalues ε_i and eigenstates $\psi_i(\mathbf{r})$ is obtained by

13

solving the Kohn-Sham equations. The charge density is subsequently evaluated to check if the convergence criterion is fulfilled. If it is not fulfilled, the effective potential is evaluated based on the new charge density in replacement of the initial guess, and the diagonalization of the Kohn-Sham equations is performed again. This loop is repeated until the convergence criterion is satisfied, the properties of the system are then calculated with the ground state charge density $n_0(\boldsymbol{r})$.

2.1.4. Basis sets

The use of basis sets for expanding the wave functions is an important step towards solving the Kohn-Sham equations. The central idea of basis set is to represent the unknown wave function of the system as a linear combination of a set of known basis function $\varphi_i(\boldsymbol{r})$

$$\psi(\boldsymbol{r}) = \sum_i c_i \varphi_i(\boldsymbol{r}), \tag{1.16}$$

where c_i is the expansion coefficient. With this linear expansion, the eigenvalue problem of the Kohn-Sham equation is transformed to a linear algebra problem of finding the solution for the secular equation. Some of the widely used basis sets include plane waves, localized atomic orbitals, numerical basis sets, and augmented plane wave methods. Each of these methods has its own advantages and pitfalls.

The plane wave approach is widely used in solid state physics, the wave function is expressed as the sum of plane waves

$$\psi(\boldsymbol{r}) = \frac{1}{\sqrt{\Omega}} \sum_{\boldsymbol{G}} c_i(\boldsymbol{G}) \, e^{i(\boldsymbol{k}+\boldsymbol{G})\cdot\boldsymbol{r}}, \tag{1.17}$$

where $\boldsymbol{G}$ is the reciprocal lattice vector, $\boldsymbol{k}$ is the crystal wave vector in the first Brillouin zone, and Ω is the volume of the unit cell in real space. The plane wave basis set is the natural choice for a

periodic system such as a perfect crystal. In practical implementation, the number of plane waves is determined by the cutoff kinetic energy E_{cut}, only reciprocal lattice vectors satisfied the following condition are included in the expansion

$$\frac{\hbar^2}{2m}|\boldsymbol{k} + \boldsymbol{G}|^2 \leq E_{cut}.$$ (1.18)

Thus, the mathematical form of the plane wave basis set is quite simple, which merits the practical implementation in calculations. The quality of the plane wave basis set is only determined by the cutoff energy. However, large amounts of plane waves are normally required to accurately represent the Kohn-Sham orbitals, especially for the orbitals near the core of atoms. The plane wave basis sets are implemented in Vienna *ab initio* simulation package (VASP) [30, 31].

In the localized atomic orbitals approach, the wave function is written as the sum of atomic-like orbitals χ_i

$$\psi(\boldsymbol{r}) = \sum_i c_i \chi_i.$$ (1.19)

Slator Type Orbitals (STOs) and Gaussian Type Orbitals (GTOs), which are written as the product of spherical harmonics $Y_{l,m}(\theta, \varphi)$ and a radical function, are two basis functions traditionally used in molecular quantum chemistry. The STOs are represented as

$$\chi(r, \theta, \varphi) = N Y_{l,m}(\theta, \varphi) r^{n-1} e^{-\zeta r},$$ (1.20)

and the GTOs are represented as

$$\chi(r, \theta, \varphi) = N Y_{l,m}(\theta, \varphi) r^{2n-2-l} e^{-\zeta r^2},$$ (1.21)

where N is the normalization factor. The localized atomic orbitals give direct insights into the atomic states, and small amounts of basis functions are usually required for describing the Kohn-Sham orbitals.

In the numerical approach, the basis orbitals are products of a numerical radial function and spherical harmonic [32]. For atom I, the basis orbitals are written as

$$\varphi_{Ilmn}(r, \theta, \varphi) = \varphi_{Iln}(r)Y_{l,m}(\theta, \varphi), \tag{1.22}$$

where n is the index for different orbital, and (l, m) is the index for angular momentum. There will be several orbitals with same angular dependence, but different radial dependence, which is conventionally called a multiple-ζ basis. The radial functions $\varphi_{Iln}(r)$ are defined by a cubic spline interpolation from the values given on a fine radial mesh. Each radial function may have a different cutoff radius, up to that radius, its shape is completely free can be introduced by the user in an input file. Beyond that cutoff radius, the radial function is forced to zero. This essentially enables the Hamiltonian and overlap matrix elements to vanish beyond a certain distance. The numerical basis sets are implemented in the SIESTA (Spanish Initiative for Electronic Simulations with Thousands of Atoms) program [33].

In the augmented plane wave approach, the real space is partitioned into the region close to each atom and the interstitial region. The wave function close to an atom is represented with localized atomic-like orbitals, and the interstitial region is represented by plane waves. The matching of wave functions at the interface between the two regions is required.

2.1.5. Pseudopotential

As mentioned in the previous section, large amounts of basis functions are required to represent the rapidly varying core states. The goal of pseudopotential is to replace the all-electron potential by an effective potential such that core states are eliminated and the valence electrons are described by pseudo-wavefunctions with significantly fewer nodes as illustrated in Figure 2.5. The pseudopotential is constructed such that it matches the true potential outside a designated core radius r_c. Similarly, each pseudowavefunction must match the corresponding true wavefunction beyond this distance. In addition, the charge densities obtained outside the core region must be identical to the true charge density. The pseudopotential approach works well due to the fact that most physical and chemical properties of atoms are determined by the structure and dynamics of valence electrons. This is particular true for the formation of chemical bonds, thus the details of the core states can be neglected. Norm-conserving [34, 35] and ultrasoft pseudopotentials [36, 37] are two forms of pseudopotentials which are widely used in modern quantum chemistry community.
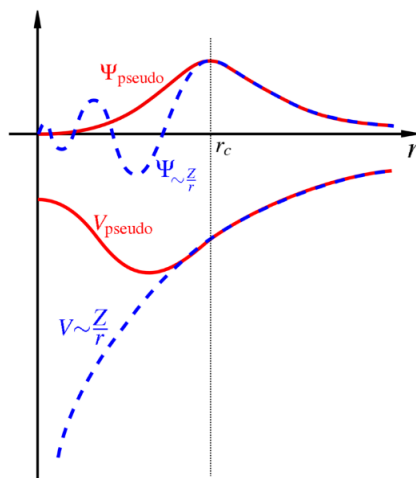
Figure 2.5 Comparison of a wavefunction in the Coulomb potential of the nucleus (blue) to the one in the pseudopotential (red). The real and the pseudo wavefunction and potentials match above a certain cutoff radius.

Norm-conserving pseudopotential was proposed by Hamann, Schluter, and Chiang[34, 35], which requires the charge enclosed within the radius r_c must be the same for the pseudo wavefunction $\varphi_{l\epsilon}^{ps}(r)$ and the all-electron wavefunction $\varphi_{l\epsilon}^{AE}(r)$ (known as the norm-conserving condition)

$$\int_0^{r_c} r^2 \varphi_{l\epsilon}^{ps}(r)^2 dr = \int_0^{r_c} r^2 \varphi_{l\epsilon}^{AE}(r)^2 \, dr. \tag{1.23}$$

Norm-conserving condition benefits the accuracy and transferability of the pseudopotential at the cost of sofeness. An alternative choice is the ultrasoft pseudopotential proposed by Vaderbilt in early 1990 [36, 37]. This approach releases the norm-conserving constraint thus offers greater flexibility in the construction of pseudopotentials which needs a much smaller size of basis functions.

2.2. Lattice dynamics from DFT

Up to this point, we have assumed that the crystal lattice to be completely rigid and nuclei stay at the positions of a perfect lattice without any displacements. However, this is not actually the case as the nuclei are always vibrating around their equilibrium positions even at very low temperature. The quanta of lattice vibrations are known as *phonons* which are extremely important for understanding the thermal properties of materials, such as heat capacity, thermal expansion, and thermal conductivity.

Assuming the equilibrium position of a nucleus j in the unit cell l is written as

$$\boldsymbol{R}(lj) = \boldsymbol{R}_l + \boldsymbol{R}_j. \tag{1.24}$$

A small displacement of the nucleus from its equilibrium position is $\boldsymbol{u}(lj)$, and U is potential energy of the system. Then, the equation of motion for this nucleus is

$$M_I \frac{\partial^2 \boldsymbol{u}(lj)}{\partial t^2} = -\frac{\partial U}{\partial \boldsymbol{u}(lj)}. \tag{1.25}$$

We can perform a Taylor expansion for the potential energy U of the nuclei with respect to $u_\alpha(lj)$

$$U = U_0 + \sum_{lj\alpha} \Phi_\alpha(lj)u_\alpha(lj) + \frac{1}{2!} \sum_{lj\alpha} \sum_{l'j'\beta} \Phi_{\alpha\beta}(lj; l'j')u_\alpha(lj)u_\beta(l'j')$$

$$+ \frac{1}{3!}\sum_{lj\alpha}\sum_{l'j'\beta}\sum_{l''j''\gamma} \Phi_{\alpha\beta\gamma}(lj; l'j'; l''j'')u_\alpha(lj)u_\beta(l'j')u_\gamma(l''j'') + O(u^4), \tag{1.26}$$

where, α, β, and γ are the indices for the Cartesian coordinates, $\Phi_\alpha(lj)$, $\Phi_{\alpha\beta}(lj; l'j')$, and $\Phi_{\alpha\beta\gamma}(lj; l'j'; l''j'')$ are the first, second and third order derivatives of the total potential as expressed as

$$\Phi_\alpha(lj) = \left.\frac{\partial U}{\partial u_\alpha(lj)}\right|_{u=0}, \tag{1.27}$$

$$\Phi_{\alpha\beta}\left(lj; l'j'\right) = \left.\frac{\partial^2 U}{\partial u_\alpha(lj)\partial u_\beta(l'j')}\right|_{u=0}, \tag{1.28}$$

$$\Phi_{\alpha\beta\gamma}\left(lj; l'j'; l''j''\right) = \left.\frac{\partial^3 U}{\partial u_\alpha(lj)\partial u_\beta(l'j')\partial u_\beta(l''j'')}\right|_{u=0}, \tag{1.29}$$

$\Phi_\alpha(lj)$ is the force on the nucleus j in the unit cell l, $\Phi_{\alpha\beta}\left(lj; l'j'\right)$, and $\Phi_{\alpha\beta\gamma}\left(lj; l'j'; l''j''\right)$ are also known as the harmonic and cubic force constants, respectively. Since the nuclei are vibrating around their equilibrium positions, the first derivative of the potential energy $\Phi_\alpha(lj)$ equals to zero. Within the harmonic approximation [38], we neglect the higher order force constants than the harmonic ones, the equation of motion in Equation 1.25 is written as

$$m_j \frac{d^2 u_\alpha(lj)}{dt^2} = -\sum_{l'j'\beta} \Phi_{\alpha\beta}(lj; l'j')u_\beta(l'j'). \tag{1.30}$$

Considering the periodic structures of crystals, we can write the displacements in terms of a plane wave with respect to cell coordinates

$$u_\alpha(lj) = \frac{1}{\sqrt{m_j}}\eta_{mq\alpha}(j)e^{iq\cdot R_l}e^{-iw_{mq}t}, \tag{1.31}$$

where m is the index for different vibrational mode, q is the wave vector, and $\eta_{mq\alpha}(j)$ is the component along direction α of the normal mode. Substituting this trial solution into the equation of motion, we obtain the dynamical equation

$$w_{mq}^2\eta_{mq\alpha}(j) = \sum_{j'\beta} D_{j\alpha,j'\beta}(q)\eta_{mq\beta}(j'), \tag{1.32}$$

where the dynamical matrix is defined as

$$D_{j\alpha,j'\beta}(q) = \frac{1}{\sqrt{m_j m_{j'}}}\sum_{l'} \Phi_{\alpha\beta}(0j; l'j')e^{iq\cdot R_{l'}}. \tag{1.33}$$

We can write the dynamical equation in 1.32 into the matrix form

$$D(q)\,\boldsymbol{\eta}(q) = w^2(q)\boldsymbol{\eta}(q). \tag{1.34}$$

Solving the above eigenvalue equation yields the phonon dispersion relation $w(q)$. The dynamic matrix can be calculated with finite displacement method or the density functional perturbation theory (DFPT) in practice. Since the dynamical matrix is Hermitian [39], the eigenvalues which are the vibrational frequencies w^2, can only be positive. Imaginary frequencies are indicative of a dynamical instability of the crystal. This law can be used to check the stability of the proposed 2D materials.

In this work, the phonon dispersion curves were calculated with Phonopy code [40]. One starts from the ground state geometry of a material, displacements of the atoms or supercells are created during

the pre-processing stage. Then, DFT calculations are performed to obtain the interatomic force constants. Finally, Phonopy will collect the force constants and do the subsequent phonon related calculations.

2.3. Molecular dynamics

Molecular dynamics is a powerful technique to study the kinetic and thermodynamic properties of complex systems. It is based on numerical integration of the classical equations of motion, and can be considered as 'computational experiment' to the system. The positions and velocities of atoms are updated from the initial state according to the Newton's equations of motion

$$m_i \frac{d^2 r_i}{dt^2} = f_i.$$

(1.35)

The force acting on an atom is calculated from the potential energy

$$f_i = -\frac{\partial U}{\partial r_i}.$$

(1.36)

The commonly used numerical integration for the Newton's equations is the so-called Verlet algorithm [41]. The basic idea of this algorithm can be derived from the Talyor's expansion for $r_i(t + \Delta t)$ and $r_i(t - \Delta t)$

$$r_i(t + \Delta t) \cong r_i(t) + \dot{r}_i(t)\Delta t + \frac{1}{2}\ddot{r}_i(t)\Delta t^2 + \frac{1}{6}\dddot{r}_i(t)\Delta t^3 + O(\Delta t^4),$$

(1.37)

$$r_i(t - \Delta t) \cong r_i(t) - \dot{r}_i(t)\Delta t + \frac{1}{2}\ddot{r}_i(t)\Delta t^2 - \frac{1}{6}\dddot{r}_i(t)\Delta t^3 + O(\Delta t^4),$$

(1.38)

adding Equation 1.37 and Equation 1.38 yields

$$r_i(t + \Delta t) \cong 2r_i(t) - r_i(t - \Delta t) + \ddot{r}_i(t)\Delta t^2 + O(\Delta t^4).$$

(1.39)

In classical molecular dynamics, the potential energy U is described with an empirical model, known as the force field, which includes the bond, bend, and dihedral angle potential as well as van der Waals and electrostatic interactions between atoms. The force field is parameterized by fitting to experimental data or *ab initio* calculations. Although classical molecular dynamics has been widely used in the treatment of liquids and solids, the force field model is not able to describe the chemical bond breaking and forming events. This is where *ab initio* molecular dynamics (AIMD) comes in. In AIMD, the force acting on an atom is obtained from electronic structure calculations such as DFT, which overcomes the limitations of classical molecular dynamics. AIMD has becoming increasingly popular for the study of a wide range of problems in materials science, chemistry, and biology. In this work, I will touch a little bit of classical molecular dynamics simulations to get the buckling structures of phosphorene. Some AIMD simulations will be employed to study the interaction of O_2 and H_2O molecules with phosphorene and to verify the stability of novel 2D materials at finite temperature.

2.4. Crystal structure prediction

Crystal structure prediction for materials plays significant role in accelerating the discovery of new materials. Once the crystal structure of a material is known, one can easily obtain its properties with DFT calculations before the material is synthesized in experiments. In addition, crystal structure prediction is valuable for investigating the materials under extreme conditions which are difficult for experiments. However, crystal structure prediction involves the searching of stable structures among huge amounts of energy minima on the crystal energy surface, which is a difficult task. A lot of efforts have been undertaken for crystal structure prediction, some practical methods available nowadays include simulated annealing [42, 43], minima hopping [44], basin hopping [45],

metadynamics [46], the genetic algorithm [47, 48], random sampling method [49], hybrid evolutionary algorithm USPEX (Universal Structure Predictor: Evolutionary Xtallography) [50], and the particle-swarm optimization CALYPSO (Crystal structure AnaLYsis by Particle Swarm Optimization) [51].

In this work, the CALYPSO code is used for the prediction of novel 2D materials. PSO is a method for multidimensional optimization which is inspired by the social behavior of birds flocking [52]. CALYPSO contains three main steps as illustrated in Figure 2.6: the generation of initial structures with the constraint of symmetry; local optimization of structures using DFT code, such as VASP [30, 31] in this work; and the evolution of structures based on PSO algorithm.
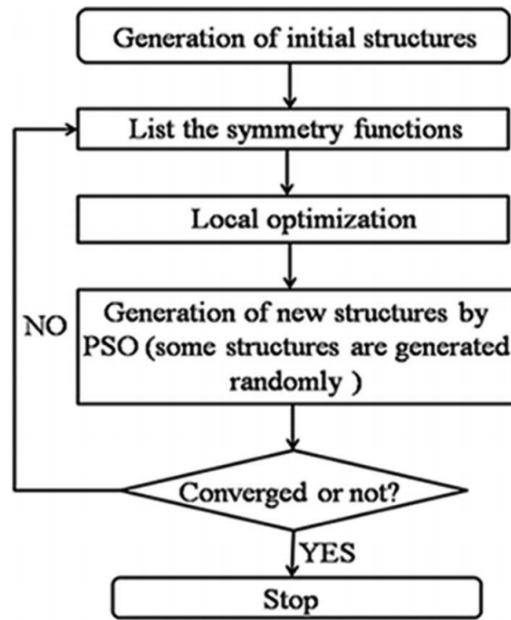
Figure. 2.6 The flow chart of 2D materials searching using CALYPSO. (Reprinted with permission from reference [53]. Copyright 2012 AIP Publishing LLC. See Appendix B for documentation of permission to republish this material.)

With this algorithm, the positions of the particle (e.g. each structure) are updated according to the following equation[49]

$$x_{i,j}^{t+1} = x_{i,j}^t + v_{i,j}^{t+1}, \tag{1.40}$$

where x and v are the positon (e.g. lattice parameters and atomic coordinates) and velocity, respectively. i represents the atomic index, j is the dimension of the structure, and t is the index of generation (e.g. a set of structures). The velocity of the particle depends on the previous unrelaxed positions $x_{i,j}^t$, the previous velocity $v_{i,j}^t$, the atomic positions of the optimized structure (*pbest*), and the atomic positions of the lowest structure (*gbest*) that has been found so far

$$v_{i,j}^{t+1} = wv_{i,j}^t + c_1 r_1 \left(pbest_{i,j}^t - x_{i,j}^t\right) + c_2 r_2 (gbest_{i,j}^t - x_{i,j}^t), \tag{1.41}$$

where w is the inertia weight defined in the range of 0.9 to 0.4 [54]. $c_1 = c_2 = 2$ has been demonstrated to give the overall best performance [55]. r_1 and r_1 are two random number in the range of 0 to 1. This code has good interface to a few DFT codes, and has been successfully utilized to predict the crystal structures of lithium-boron compounds at high pressure [56] and other 2D materials [53, 57].

Chapter 3   Group IV elemental 2D materials – 6,6,12-graphyne and engineering of its properties[*]

3.1. Introduction

Graphene remains one of the most extensively investigated 2D materials and has offered a wealth of information on the exotic physics and potential technological applications [4, 58-62]. Graphene has a honeycomb structure with two carbon atoms in the unit cell. The carbon atoms are connected through σ bonds with sp^2 hybridized character. The out-of-plane p_z orbital forms the π bands which endows the observed linear dispersion near Fermi level [63]. Graphene can be synthesized by top-down strategy such as exfoliation from bulk graphite [58, 64], or bottom-up strategy such as chemical vapour deposition (CVD) [65-68]. There are a few comprehensive reviews on the fabrication, characterization, and application of graphene [69-71].

As the closest cousin of graphene belonging to the group IV elemental monolayers and being compatible with Si-based electronics, silicene has also attracted a great deal of attention from theorists and experimentalists [72-74]. The stronger spin orbit coupling in silicene compared to graphene makes it a potential candidate for the study of quantum spin Hall effect (QSHE) [75-77]. The chemical bonds in silicene are different from those in the bulk: bulk Si is composed of sp^3 hybridized Si atoms; whereas silicene has a low buckled structure with mixed sp^2-sp^3 hybridized Si atoms [78, 79]. Free-standing silicene is predicted to have linear dispersive band structure near Fermi level similar to that in graphene [80, 81]. The buckled structure and sp^2-sp^3 hybridized bonds impart novel physical and chemical properties to silicene differentiating it from graphene [82]. Due to the

---

[*] The contents in this chapter were previously published in Appl. Phys. Lett., 2014, 104, 213107. Refer Appendix C for granted permission to be republished.

non-existence of a layered bulk counterpart, silicene cannot be isolated by exfoliation methods. Silicene has been grown by depositing Si atoms on Ag(111) [73], $ZrB_2(0001)$ [83] , and MoS_2 [84] substrates.

Germanene is another analogue of graphene belonging to group IV elemental monolayers. The structure of germanene is similar to that of silicene with a buckled lattice [80]. The Ge-Ge bonds in germanene show mixed sp^2-sp^3 hybridized character [78]. The electronic properties of germanene have been extensively studied using DFT [80, 85, 86].   Atomically thin germanene has been recently synthesized on Au(111), Al(111) or Pt(111) surface [7, 87, 88].

All these group IV elemental monolayers are found to be semi-metallic with Dirac cone like band structures. New allotropes of group IV elemental monolayers have also been proposed, for example graphyne. In this section, the electronic properties of graphyne and the engineering of its properties with external strain is explored.

Owing to the flexibility of forming sp, sp^2 or sp^3 bonds [89], carbon can form abundant allotropes including three dimensional (3D) (e.g. diamond and graphite), two dimensional (2D) (e.g. graphene) [90], one dimensional (1D) (e.g. nanotubes [91] and nanoribbons [92]), and even zero dimensional (0D) fullerenes [93]. Graphyne, another 2D carbon allotrope which is formed by inserting a carbon triple bond (-C≡C-) into C-C bond (Figure 3.1), has attracted increasing attention in recent years. For example, strategies for synthesizing graphyne were proposed [94, 95]. Theoretical calculations on $α$, $β$, and $γ$-graphyne were performed to predict their stability and electronic properties [96]. Synthesis of graphdiyne, a 2D carbon allotrope which has two tripe bonds (-C≡C-) inserted into C-C bond, has also motivated attention on the several forms of 2D carbon allotrope [97]. It was predicted that $α$-, $β$-, and 6,6,12-graphyne have graphene-like Dirac cone band structures

[98]. Thus, existence of Dirac cones for 6,6,12-graphyne which has a rectangular lattice is a significant prediction since it has long been assumed that Dirac cone is unique for the hexagonal 2D materials or topological insulators [99]. Moreover, 6,6,12-graphyne has two nonequivalent anisotropic Dirac cones making it to be even more fascinating than graphene for device applications.

Applying external strain is one of the approaches to tailor electronic properties of materials. Strain could be induced by the mismatch of lattice constant and thermal expansion between the substrate and the film, which has been widely used to achieve tunable properties in functional oxide films[100, 101]. In graphene, it has been shown that its Dirac band structure is invariant under a symmetric strain and a band gap could open by applying an asymmetric strain [102]. The tunable energy gap could be realized in a bilayer graphene by changing the strength and direction of strain [103]. Local strain could be utilized to integrate graphene for all carbon electronics [104]. Experimentally, it is also possible to apply large strain by stretchable substrates [105]. Considering the importance of the relationship between strain and the electronic properties of 2D materials, we will investigate such relationship for monolayer and bilayer of 6,6,12-graphyne using density functional theory, and will show that Dirac cones can be tuned independently with the strain applied to graphyne.

3.2. Computational methods

Electronic structure calculations were performed using a norm-conserving pseudopotential [106] as implemented in the SIESTA package [33]. In our calculations, van der Waals (vdW) interactions [107, 108] were included in density functional theory (DFT). We used a 11×11×1 Monkhorst-Pack grid [109] for *k*-point sampling in the Brillouin Zone (BZ). The mesh cutoff energy is 400 Ry and the vacuum distance perpendicular to the monolayer is larger than 25 Å in the supercell model employed. The

geometric structure was obtained by relaxing all the atoms with residual force smaller than 0.01 eV/Å on each atom.

3.3. Results and discussions

The 6,6,12-graphyne monolayer is defined by the number of carbon atoms along the rings as shown in Figure 3.1. The (average) length of sp^2 hybridized C bond is 1.447 Å, and that of the sp hybridized C bond is 1.257 Å in the ground state configuration of 6,6,12-graphyne obtained at the vdW-DFT level of theory. To keep the consistency with calculations for the bilayer where the vdW interaction is necessary, vdW interaction is also included in the calculations for the monolayer. The calculated bond lengths are slightly larger than those obtained at PBE-DFT level of theory [110].
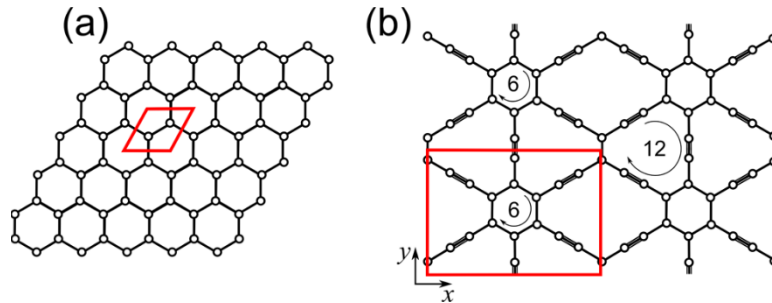
Figure 3.1 Schematic representations of (a) graphene and (b) 6,6,12-graphyne. 6,6,12-graphyne is defined by the number of carbon atoms along the rings as shown in (b). (Reprinted with permission from reference [111]. Copyright 2014 AIP Publishing.)

Figure 3.2 shows the calculated band structure of the monolayer of 6,6,12-graphyne. In the first BZ, there exists two kinds of anisotropic Dirac cones. One of the Dirac points is slightly above the Fermi energy, and the other is slightly below the Fermi energy suggesting that 6,6,12-graphyne is self-doped [98]. The cone I is located at the high symmetric direction from Γ to X', and the cone II is at X point. These cones are anistropic based on the absolute derivative of the π band (right panels of Figures 3.2 (c) and (d)). The cone I shows a linear dispersion with the group velocities of $v_{kx} =$

0.49×10^6 m/s and $v_{ky} = 0.58 \times 10^6$ m/s which are about 40% smaller than that of graphene (v_F $=0.85 \times 10^6$ m/s)[112, 113]. The cone II is parabolic near the center of the cone, so the group velocity goes to zero. Note that the group velocity is defined by the derivative of energy dispersion $v_k = (1/\hbar)(\partial E_k / \partial k)|_{E_k=E_F}$.

In our case, the cone II has a band gap of 43 meV, which is different from the previous results [98]. This is due to the fact that the exchange-correlation functional form in this study includes the effect of vdW interactions which are important in predicting accurate interlayer spacing for bilayers of carbon-based systems [114].
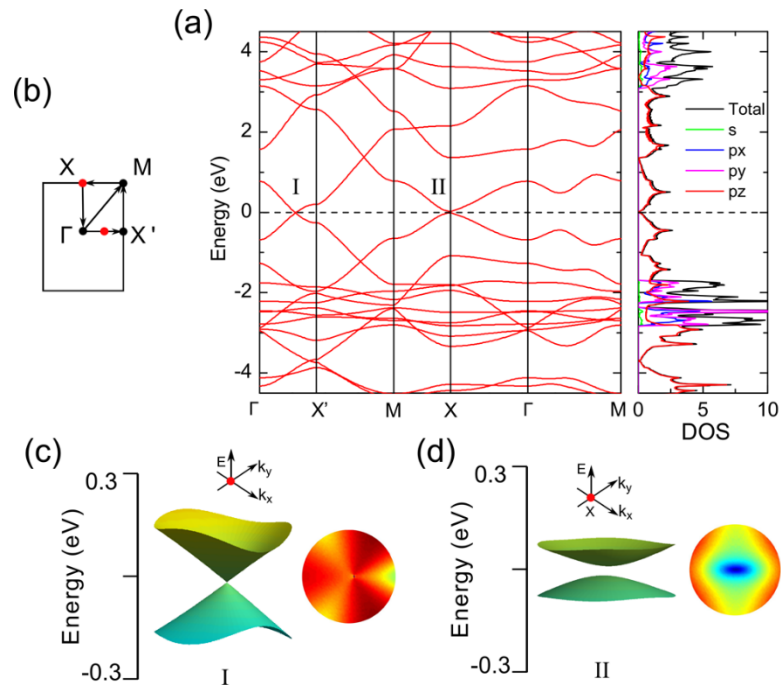
Figure 3.2 (a) Band structure of 6,6,12-graphyne monolayer; (b) The illustration of first BZ and high symmetry points; (c) 2D band structure of the cone I (left panel) and the absolute derivative (right panel) of the corresponding π band; (d) 2D band structure of the cone II (left panel) and the absolute derivative (right panel) of the corresponding π band. Fermi energy is set to zero. The 2D band structure are ploted within a circle of radius 0.2*pi/a. (Reprinted with permission from reference [111]. Copyright 2014 AIP Publishing.)

Figure 3.3 shows the band structure of graphyne with tensile strain applied along x direction. The strain drives movement of Dirac points in the momentum space. With increasing strain, the cone I moves towards X', and the two conical dispersions of the bands merge into a single cone at applied strain of 6.3%. The merged cone shows the linear dispersion along k_y and the parabolic dispersion along k_x. This is also accompanied by opening of the energy gap for strains larger than 6.3%. Such transition from zero gap to finite gap band structure was also predicted for the pristine graphene under the application of external strain, though the critical strain for the merging of Dirac cones was reported to be larger that 20% [115, 116]. Thus, 6,6,12-graphyne could be a potential candidate material to study the merging of Dirac cones without using complex techniques involving molecular graphene [117] or cold atoms [118]. The position of the cone II does not change with tensile strain up to 8% along x direction. For the tensile strain along y direction, the gap at the cone II increases whereas the position of cone I is not affacted.
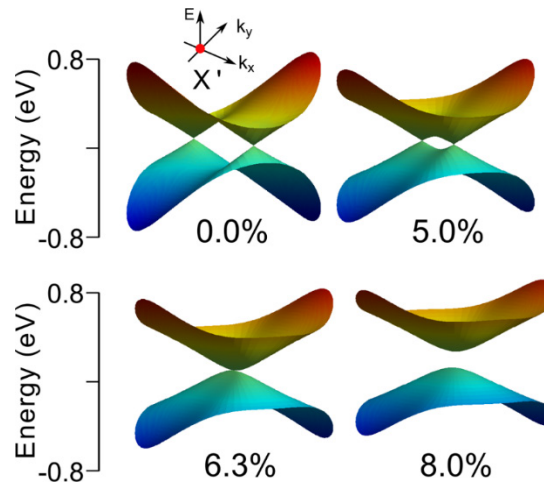
Figure 3.3 Variation of the calculated 2D band structures of the cone-I with strain along x. The band structures are plotted within a circle of radius 0.5*π/a centered at X'. (Reprinted with permission from reference [111]. Copyright 2014 AIP Publishing.)

The effects of compressive strain on the band structure of the monolayer are shown in Figure 3.4. With the compressive strain applied along *x* direction, the cone I shifts above Fermi energy, and the cone II shifts below Fermi energy. Thus, shifting of the Dirac points causes n-type doping at the cone I, and p-type doping at the cone II. We notice that the strain induced self-doping effect has also been reported for silicene and germanece [119] for which there only exits one kind of a charge carrier. This is not the case with 6,6,12-graphyne for which both negative and positive charge carriers coexist in the lattice. The Dirac points shift almost linearly with compresive strain (Figure 3.4(b)), which means the concentration of charge carriers can be tuned effectively. The application of compressive strain along *y* direction has similar effects, however, the cone I is p-type doped and the cone II is n-type doped.
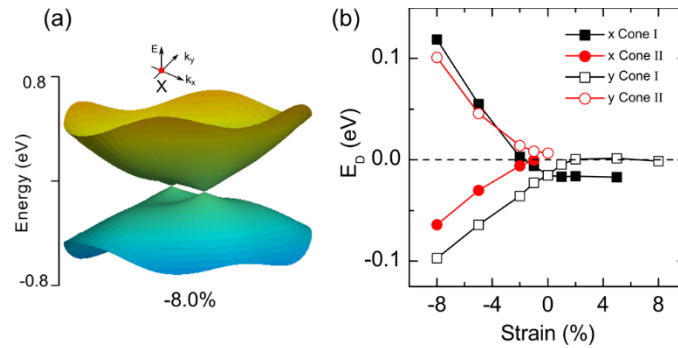
Figure 3.4 (a) The calculated 2-D band structure of the cone-II; (b) variation of the energy of the two Dirac points with strain along x and y. Fermi energy is set to zero. The band structure is plotted within a circle of radius 0.5*π/a centered at X. (Reprinted with permission from reference [111]. Copyright 2014 AIP Publishing.)

Since the cone II is parabolic near the center of the cone, its group velocities go to zero if no tensile strain is applied. The group velocities appear when the applied compressive strain pushes the cone to be duplicate (Figure 3.4(a)). For the uniaxial strain along *x* direction, the group velocity v_{kx} of the cone I decreases gradually, and goes to zero with the merging of the Dirac cones; the velocity v_{ky} of the cone I increases slightly and vanishes when the band gap opens up as shown in Figure

3.5(a). The increased discrepancy between v_{kx} and v_{ky} with the tensile strain along x implies that the anisotropy of the cone I is greatly increased. The anisotropy of the group velocity may lead to the observable resistance anisotropy [105]. For the strain along y, the group velocities of the cone I nearly remains the same (Figure 3.5 (b)).

Bilayers of graphene-like systems can possess the properties which are not exhibited by monolayers such as tunability of the band gap in graphene bilayer by the external electric field [120]. Also, synthesis of a bilayer is likely to be easier than that of a monolayer; multilayer graphidyne was first synthesized before monolayer could be produced [97]. We will now consider 6,6,12-graphyne bilayer focusing on its equilibrium stacking configuration and the effect of strain on its electronic properties. The calculated results find the AB-stacked configuration to be most stable bilayer configuration with the interlayer spacing of 3.416 Å. The calculated interlayer distance is consistence with the one predicted for the α-graphyne [121].
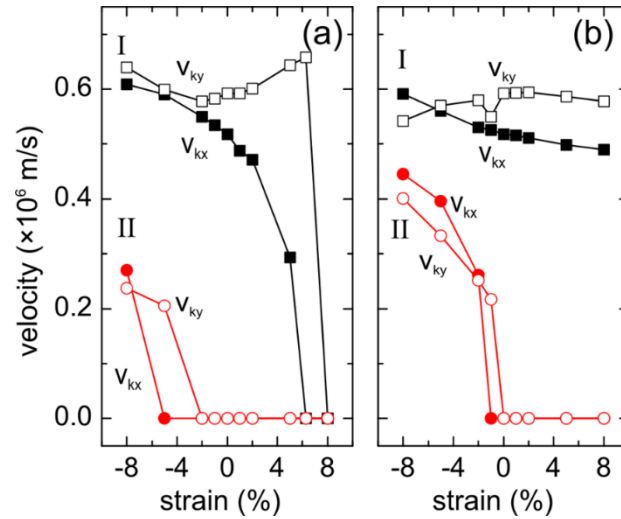
Figure 3.5 Variation of the group velocities of π electrons of the cones I and II with the uniaxial strain (a) along x, and (b) along y. (Reprinted with permission from reference [111]. Copyright 2014 AIP Publishing.)
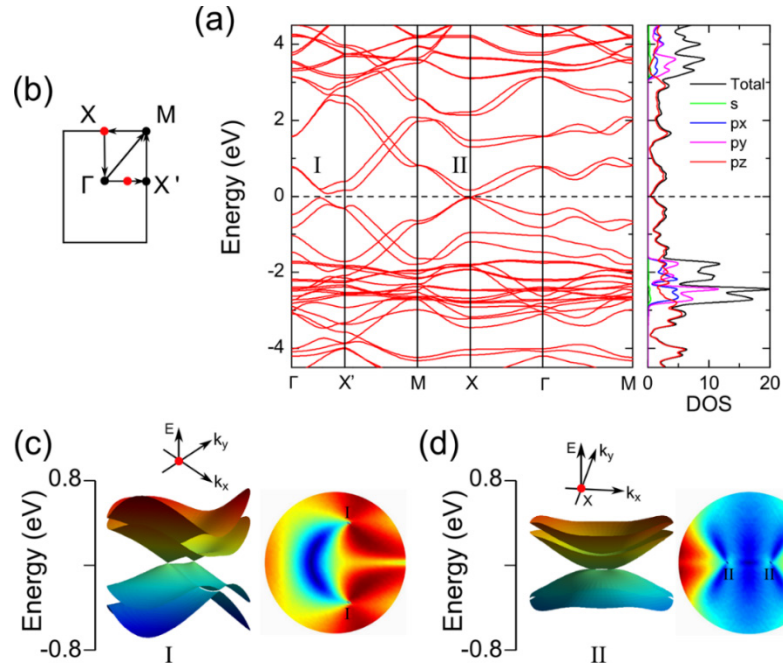
Figure 3.6 (a) Band structure of AB-stacked 6,6,12-graphyne bilayer; (b) Illustration of the first BZ; (c) 2D band structure around Cone I (left panel) and the absolute derivative (right panel) of the corresponding π band; (d) 2D band structure around Cone II (left panel) and the absolute derivative (right panel) of the corresponding π band. Fermi energy is set to zero. The 2D band structure are ploted within a circle of radius 0.5*π/a. (Reprinted with permission from reference [111]. Copyright 2014 AIP Publishing.)

Figure 3.6 shows the band structure of the AB stacked bilayer showing the splitting of highly anisotropic Dirac cones (Figures 3.6 (c) and (d)) due to appearance of the interlayer interaction in the bilayer system. The group velocities of the cone I are $v_{kx} = 0.24 \times 10^6$ m/s and $v_{ky} = 0.55 \times 10^6$ m/s showing the enhancement in anistropy relative to that of the monolayer. The π and π* bands at cone II meet together and result into two Dirac points near X (Figure 3.6(d)). The splitting of Dirac cones is associated with overlapping of p_z orbitals of the two layers. This is confirmed by taking the interlayer distance to be large enough (~6 Å) to exclude interactions between monolayers; the band structure is exactly the same as that of the monolayer. On the other hand, a bilayer with a interlayer distance of 2.5 Å shows opening of the band gap of 43.5 meV due to relatively large overlap of the

p_z orbitals. This implies the possibility of tuning electronic properties with the application of the perpendicular strain to the bilayers.

The effects of the in-plane strains on 6,6,12-graphyne bilayer are similar to the effects predicted for the monolayer. A small tensile strain along x direction will cause the shifting of the cone I in the BZ. The gap opens up with a larger strain, but the strain along x has little influence on the cone II. Likewise, the unixial strain along y will open up the gap at the cone II, but it does not affect the cone I. The compressive strain shifts Dirac points either above or below Fermi surface, which indicates that the self-doping effect in 6,6,12-graphyne bilayer could also be achieved under a compressive strain.

The elastic properties can be characterized by Young's modulus and Poisson's ration which are critical for the strain engineering of electronic properties of materials. As it is ambiguous to define the volume of the sheet with atomic thickness, the in-plane stiffness constant C is generally used. In the limit of small deformations, the strain energy is simply a quadratic function of strain [122], so the stiffness constant C can be expressed as

$$C = \frac{1}{S_0}\frac{\partial^2 E_S}{\partial \varepsilon^2},\tag{3.1}$$

where S_0 is the equilibrium area, the strain energy E_S is the energy difference between the strained and strain relaxed system. The stiffness constant can be obtained by fitting the strain energy curves within the elastic region.

The calculated stiffness constants of 6,6,12-graphyne are 183 and 136 N/m along x and y directions, respectively. These values are slightly larger than the values of ~142 and ~112N/m (obtained by converting the data obtained by molecular dynamics calculations in units of GPa using the thickness

of 3.2 Å) [123, 124]. Due to the weak interlayer vdW interactions, the stiffness constants for AB stacking bilayer are approximately twice that of the monolayer. The stiffness of 6,6,12-graphyne is just one half of the experimental value for graphene (340 ± 40 N/m [125]), which implies that 6,6,12-graphyne is softer than graphene. The softness facilitates the strain engineering of electronic properties and makes the realization of the merging of Dirac cones possible in 2D materials [115, 118, 126].

3.4. Summary

First principles calculations were performed on 6,6,12-graphyne monolayer and bilayer systems. Both monolayer and bilayer systems are semi-metals with Dirac cones in first Brillouin zone. Uniaxial tensile strain along x will induce shifting of the cone I, and the merging of two conical bands at X' is predicted. The tensile strain along y will increase the energy gap at the cone II. The compressive strain shifts the energy of the Dirac points almost linearly which results into coexistence of positive and negative charge carriers in the lattice. The large anisotropy in stiffness is also being predicted for the monolayer graphyne. The energetically preferred structure of the graphyne bilayer is similar to the Bernal's AB stacking of two adjacent graphene layers. The anisotropy of the Dirac cone is largely enhanced in the bilayer, which implies a possibility of increased anisotropy in its electron transport properties. We believe that the predicted tunability of electronic properties makes 6,6,12-graphyne to be a candidate 2D material for theoretical studies and applications at nanoscale.

Chapter 4   Group V elemental 2D materials – phosphorene and engineering of its properties[*]

4.1. Introduction

As discussed in the previous chapter, the group IV elemental monolayers have a zero band gap which limits their applications in transistors. Although tremendous efforts have been done to open the band gap in graphene, for examples by patterning graphene into nanoribbons or applying perpendicular electric field to multilayer graphene, the band gap value is still too small (less than 0.2 eV) for applications where a suitable band gap is necessary [9, 120, 127, 128]. Different from the group IV elemental monolayers, a fundamental band gap exists in group V elemental monolayer phosphorene. And the band gap value can be effectively tuned from 0.3 eV in the bulk form to 2.0 eV in the monolayer form, which is attracting from an application point of view. In this section, the possibility of tuning the electronic properties of phosphorene with external defects and strain is explored. The results may guide the design of phosphorene based electronic devices for future applications.

4.2. Engineering phosphorene with adatoms

4.2.1. Introduction

It is well-known that the exfoliation or growth processes can introduce defects and impurities in 2D materials, which can dramatically alter the electronic, thermal and mechanical properties of the

---

[*] The contents in this chapter were previously published in Appl. Phys. Lett., 2015, 106, 173104 and Nanotechnology, 2016, 27, 055701. Refer Appendix C and D for granted permission to be republished.

pristine counterparts. Vice versa, a deliberate introduction of defects can be a possible approach to modify the properties of the pristine materials. For example, ion or electron irradiation can introduce intrinsic point defects, e.g. vacancies and Stone-Wales (SW) defect in graphene [129, 130], which could enrich its properties to act as a building block for devices with new functionalities [131, 132]. Besides intrinsic defects, extrinsic defects such as adatoms are shown to be important to design graphene based devices with dedicated properties [133].

Considering that the scientific work on investigating the properties of phosphorene has recently started, the role of extrinsic point-defects including surface adatoms is still undefined. The adsorption of several adatoms was considered recently [134, 135], but the underlying mechanism of the different behaviors of the adatom on phosphorene is not mentioned. In this section, we will focus on the adsorption of a series of adatoms from B, C, N, O, and F which provide an interesting variation in the number of valence electrons with a [He] core and the electronegativity. B is s^2p^1, C is s^2p^2, N is s^2p^3, O is s^2p^4 and F is s^2p^5. The values of electronegativity for B is 2.0, C is 2.5, N is 3.1, O is 3.5 and F is 4.1 [136]. The electronegativity of P is 2.1 [136]. We will calculate their geometric structure and electronic properties on phosphorene comparing the results with those on graphene and silicene to gain insights into the adsorption mechanism due to puckered nature of phosphorene [15]. We will see that the adsorption behavirour of B and C is totoally different from that of N, O and F adatom, and the adsorption mechanism is dorminated by the electronagetivity of the adatom and the surface electronic structure of phosphorene. In Sec 4.2.2 is a brief description of the computational model. Results and discussion are given in Sec. 4.2.3.

4.2.2. Computational methods

The electronic structure calculations were performed using the norm-conserving Troullier-Martins pseudopotential implemented in the SIESTA program package [33]. The Perdew-Burke-Ernzerhof (PBE) [137] exchange-correlation functional to density functional theory was employed, which has been shown to correctly describe the adsorption of adatom on graphene [138] and the adsorption of O adatom on phosphorene [139]. The energy convergence is set to 10^{-5} eV, and the residual force on each atom is smaller than 0.01 eV/Å during structural optimization. The mesh cutoff energy was chosen to be 500 Ry. A double-ζ basis including polarization orbitals were used.

The (4×5) supercell with 80 atoms was used to simulate the pristine phosphorene. The length of the supercell is 18.6 Å ×16.7 Å, and the vacuum distance normal to the 2D lattice was chosen to be 20 Å to eliminate interaction between the replicas. A single adatom is added in the supercell which corresponds to an adatom concentration of ~$3.23×10^{13}$/cm^2. The reciprocal space was sampled by a grid of (4×5×1) k points. The tunneling current calculations were based on Bardeen, Tersoff, and Hamann (BTH) formulism [140].

In order to benchmark the modeling elements, the results on the pristine phosphorene were compared with the previously reported results. The bond lengths are calculated to be 2.29 and 2.26 Å, which are consistent with the values of 2.28 and 2.24 Å obtained at the PBE-DFT level of theory [15, 19]. A direct band gap slightly less than 1 eV is predicted for the pristine phosphorene which is in excellent agreemnt with the previous thereoctical reports [16, 141].

4.2.3. Results and conclusions
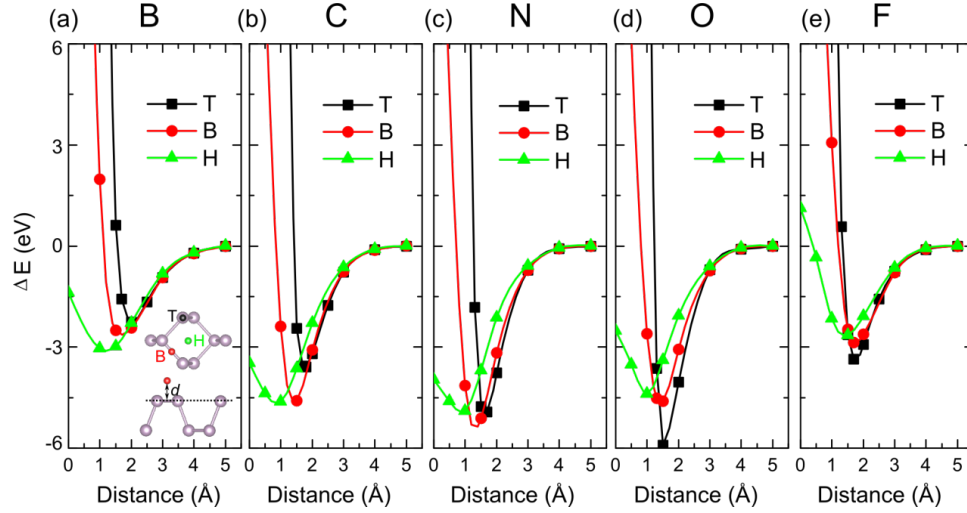
Figure 4.1 Energy profile of adatoms approaching the surface of phosphorene at the top (T), bridge (B), and hexagonal site (H): (a) B, (b) C, (c) N, (d) O, and (e) F. (Reprinted with permission from reference [142]. Copyright 2015 AIP Publishing.)

We begin with calculations to determine the energy profile of the adatom approaching surface sites of phosphorene (Figure 4.1). The surface sites considered are (i) hexagonal site (H) - site above the center of hexagonal ring, (ii) top site (T) - above the top phosphorus atom, and (iii) bridge site (B) - above the bridge of the top P-P bond. The energy profile was initially obtained by varying the distance of the adatom to the 'rigid' phosphorene. Later, a full structural optimization was performed to obtain the ground state configuration in which all atoms are allowed to relax.

The calculated ground state configurations of the adsorbed systems are shown in Figure 4.2. Interestingly, B and C adatoms break the native P-P bonds and enter the interstitial site of the 2D lattice. The configuration at the top site is found to be 0.75 and 1.27 eV higher in energy for B and C adatom, respectively, demonstrating that B and C atom prefer to penetrate into the pristine lattice. On the other hand, the interstitial site is found to have higher energy than the surface site for N, O

39

and F atoms. The results, therefore, show that N, O and F atoms tend to bind the surface P atom without breaking the P-P bonds. The (average) bond lengths of surface adatoms are R_{P-B} (1.96 Å), R_{P-C} (1.80 Å), R_{P-N} (1.68 Å), R_{P-O} (1.54 Å), and R_{P-F} (1.70 Å).
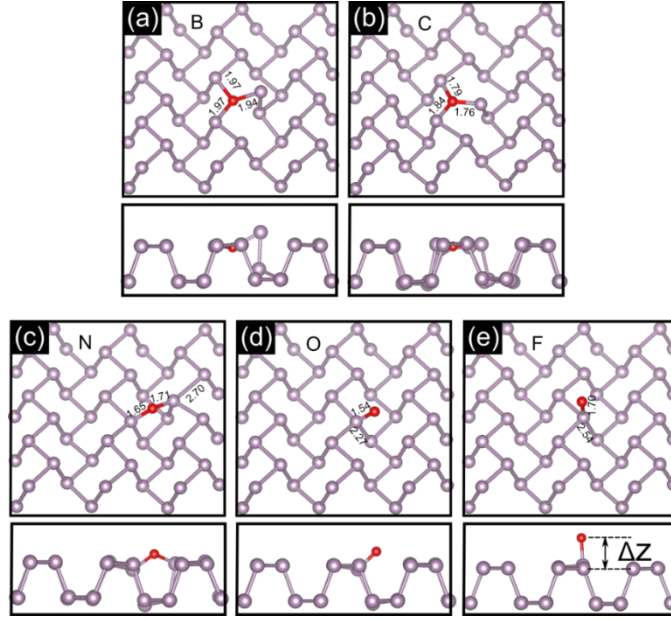
Figure 4.2 Adsorption of adatoms with a [He] core on phosphorene after structural optimization:
(a) B, (b) C, (c) N, (d) O, and (e) F. (Reprinted with permission from reference [142]. Copyright 2015 AIP Publishing.)

The height of the adatom from the surface (Δz) gradually increases in going from B to F (Table 4.1). In the equilibrium configurations, some of native P atoms are repelled away by B or C at the interstitial site resulting into significant lattice distortions. For N, O, or F surface adatoms, the overall lattice structure of phosphorene is maintained. Note that the P-P bond length in the pristine 2D lattice is 2.26 Å. The binding energy of the surface adatom is defined as

$$E_{binding} = E_{total} - (E_{pristine} + E_{atom}), \qquad (4.1)$$

where E_{total} is the total energy of phosphorene with surface adatom, $E_{pristine}$ is the energy of pristine phosphorene. E_{atom} is the energy of a single adatom in a 10 Å×10 Å ×10 Å cell, which are -97.10 eV, -153.12 eV, -271.94 eV, -440.22 eV, and -665.22 eV for B, C, N, O and F atom, respectively. The adsorption of these light elements is found to be exothermic with a negative binding energy which implies that these light elements could bind strongly on phosphorene (Table 4.1).

Table 4.1. Adsorption of adatoms with a [He] core on phosphorene: The prefered binding site, distance between adatom to the host P atom (R), binding energy ($E_{binding}$), Voronoi charge ($Q_{Voronoi}$) and magnetic moment (μ_B). Δz is the height of adatom from the surface. Negative Voronoi charge means excess of electron. (Reprinted with permission from reference [142]. Copyright 2015 AIP Publishing.)

Adatom	Preferred Site	$R_{host-adatom}$ (Å)	Δz (Å)	$E_{binding}$ (eV)	$Q_{Voronoi}$ (e)	Magnetic moment (μ_B)
B (s^2p^1)	Interstitial	1.96	≈0.0	-5.08	-0.19	1.00
C (s^2p^2)	Interstitial	1.80	≈0.0	-5.16	-0.21	0.00
N (s^2p^3)	Surface	1.68	0.51	-2.98	-0.31	1.00
O (s^2p^4)	Surface	1.54	0.87	-4.69	-0.33	0.00
F (s^2p^5)	Surface	1.70	1.78	-2.30	-0.15	1.00

In order to understand the site dependency of the light elements with a [He] core, the deformation charge density ($\rho=\rho_{total}-(\rho_{phosphorene}+\rho_{atom})$) of the adsorbed phosphorene is calculated (Figure 4.3). B and C at the interstitial sites clearly form bonds with three native P atoms. These sp^2–like bonds almost lie in a same plane, and the charge density increases in the region between the adatom and P (Figures 4.3 (a) and (b)). On the other hand, N, O and F adatoms appear to form bonds with one

or two native P atoms at the surface in their equilibrium configurations. Accumulation of the charge density around the adatom suggests that N, O and F atoms gain electrons from the host P atoms (Figures 4.3 (c), (d) and (e)).
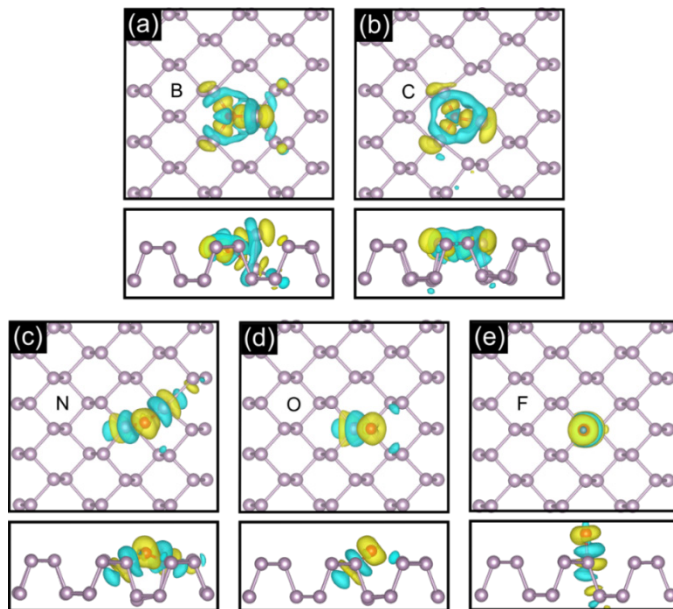
Figure 4.3 Deformation charge density of adsorption of adatoms with a [He] core on phosphorene: (a) B, (b) C, (c) N, (d) O, and (e) F. The yellow (blue) region represents accumulation (depletion) of electrons. The isovalue is 0.003 e/Å³. (Reprinted with permission from reference [142]. Copyright 2015 AIP Publishing.)

A schematic illustration explaining the adsorption of light elements with a [He] core on phosphorene is given in Figure 4.4. In phosphorene, each P atom (with s^2p^3 valence electron configuration) shares three of its valence electrons with the neighboring P atoms forming sp^3 bonds while the remaining valence electrons form a lone pair at the surface. Since N, O, and F atoms are more electronegative than the host P atoms, these adatoms tend to attract electrons from the native P atom. For example, F has s^2p^5 valence electron configuration and will attract one electron of the lone pair forming bond with one native P atom. O has s^2p^4 electron configuration attracting the lone

pair of P atom, possibly form P=O bond with the bond length of 1.54 Å [134]. N has s^2p^3 configuration and will form bond with two native P atoms. This scenario is clearly reflected in Table 4.1 showing the calculated bond lengths ($R_{host\text{-}adatom}$) in the equilibrium configurations of the adsorbed systems. B and C atoms are close to P atom in terms of the electronegativity, they prefer to form sp^2 bonds with the native P atoms by breaking the native sp^3 bonds of the pristine phosphorene.
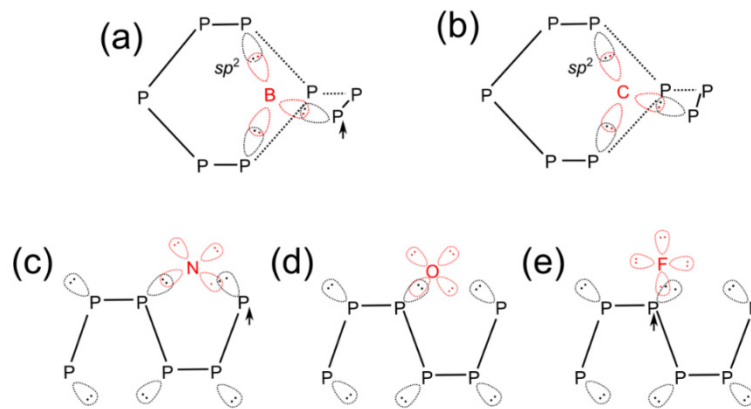
Figure 4.4 A schematic illustration of adsorption of adatoms with a [He] core on phosphorene: (a) B, (b) C, (c) N, (d) O and (e) F. The arrow represents upaired electron around the atom. (Reprinted with permission from reference [142]. Copyright 2015 AIP Publishing.)

Comparing our results on phosphorene with those obtained for graphene [143-145], we find that adatoms prefer surface sites on graphene due to robustness of the sp^2 network; B, C, N and O adatoms prefer the bridge site whereas F adatom prefers the top site. The calculated binding energies of B, C, N, O, and F adatoms on graphene are -1.77 [143], -1.4 [144], -0.88 [145], -2.41 [145], -2.01 eV [145], respectively. Note that sp^3 bonds tend to be more reactive leading to higher binding energies of surface adatoms on phosphorene (Table 4.1). This is also true for silicene where the sp^3-like lattice structure is highly reactive [146], the adsorption of adatom such as C could result in the local

reconstruction in silicene [147]. Therefore, B, C, N, O or F adatom on silicene also has high binding energy, which is -5.85 [146], -5.88 [147], -5.54 [146], -6.16 [147], and -4.45 eV [148], respectively.
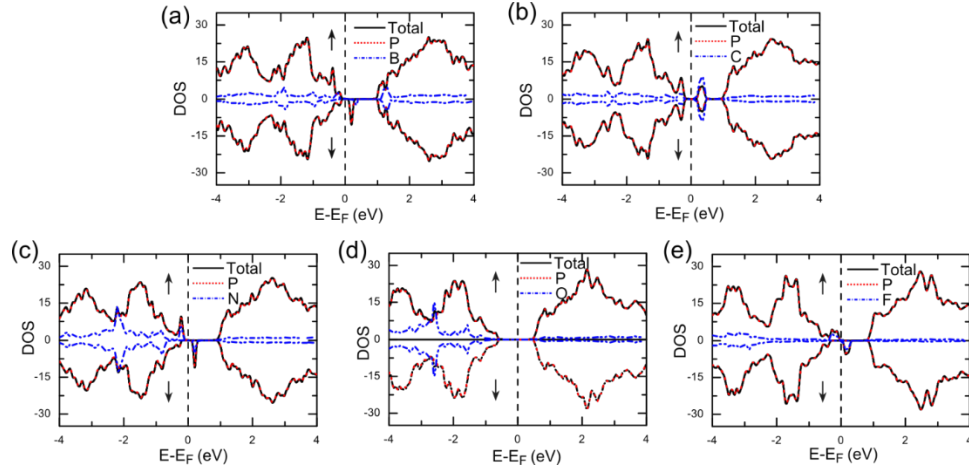
Figure 4.5 Spin polarized density of states of adatoms with a [He] core on phosphorene: (a) B, (b) C, (c) N, (d) O, and (e) F. The states related to the surface adatoms are magnified by a factor of 10. The up (or down) arrow represents spin up (or spin down) density of states. (Reprinted with permission from reference[142]. Copyright 2015 AIP Publishing.)

Figure 4.5 displays spin and atom resolved density of states (DOS) of the adsorbed systems. B, C, N, and F induce mid-gap states in the band gap of phosphorene. On the other hand, O induces states inside the valence band due to the possible formation of a stronger P=O bond. Adsorption of B, N, or F also results in spin polarized DOS which induces ~1 μ_B magnetic moment to the lattice. The spin polarized charge density is found to be localized on the distorted P atoms around the adatoms. B has three valence electrons which form sp^2-like bonds with three neighboring P atoms, one of the neighboring P atom (the one was repelled away from its original site) has an unpaired electron in the 2p orbit (Figure 4.4(a)) which induces magnetic moment in the system. The adsorption site of C is similar to that of B (Figure 4.4 (b)), however, C has one more valence electron than B, which could possibly pair with the electron of P resulting in zero net magnetic moment. N and F adatoms

will attract the electron from the lone pair of P, and left an unpaired electron on the $2p$ orbit of the native P atom, which contributes to the observed magnetic moment (Figure 4.4). O adatom will attract both of the electrons of a lone pair which will not introduce magnetic moment to the system.

Considering that the tunneling current is sensitive to the local electronic properties of surface atoms, we now investigate the tunneling characteristics of the adatom systems. The tunneling current from the sample to the tip at location $\vec{r}_t$ based on Tersoff and Hamann approximation [140] is

$$I(\vec{r}_t; V) \approx \frac{2\pi e}{\hbar} \int_{-\infty}^{+\infty} \rho_t \left(E - \frac{eV}{2} \right) \rho_s \left(\vec{r}_t; E + \frac{eV}{2} \right) F(E) dE, \tag{5.1}$$

where ρ_t is the electron density of the tip, ρ_s is the electron density of the sample at the location of the tip. $F(E)$ is the term to include the effect of thermally excited electrons as proposed by He *et al*. [149, 150] In order to mimic the scanning tunneling micriscope (STM) measurements, the tip was simulated by a Au_{13} cluster which was placed above the adatom with a distance 5 Å.
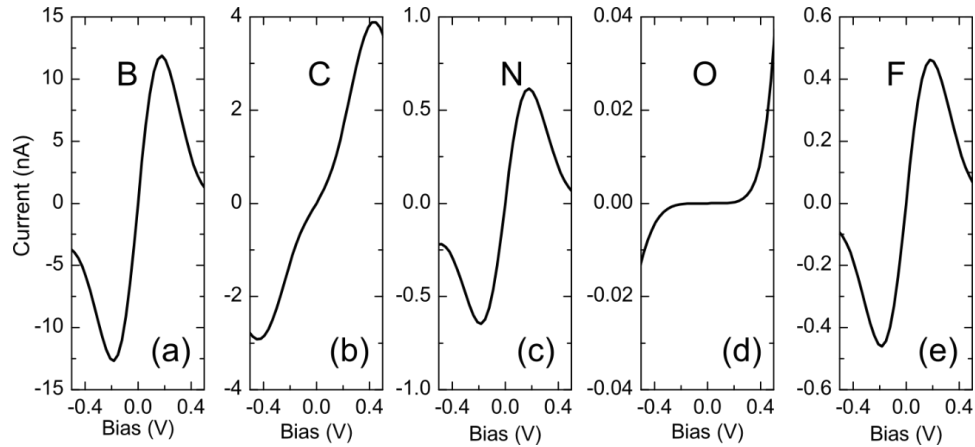
Figure 4.6 The tunneling characteristics of adatoms with a [He] core on phosphorene: (a) B, (b) C, (c) N, (d) O, and (e) F. (Reprinted with permission from reference[142]. Copyright 2015 AIP Publishing.)

B, C, N, and F atoms show metallic tunneling characteristics with abrupt increase in the current at a small bias (Figure 4.6). While the tunneling current above O adatom shows a diode like behavior with a gap in the small bias region. The tunneling characteristics are consistent with the calculated DOS where mid-gap states due to B, C, N and F contribute to the tunneling current at small bias. This is not the case with O adatom since it does not introduce any mid-gap states in phosphorene. Also, prominent negative differential resistance (NDR) is observed for B, C, N and F adatoms due to the mid-gap states near Fermi level.

4.2.4. Summary

In summary, adsorption of light elements with a [He] core on phosphorene is investigated by using density function theory. The results find that B and C prefer the interstitial site and N, O, F atoms prefer the surface site of phosphorene. The distinct preference of these adatoms on phosphorene is the result of the interplay between electronegativity values and electronic structure of phosphorene. B, C, N, and F adsorption will induce mid-gap states leading to metallic characteristics of the phosphorene. On the other hand, single oxygen adatom adsorption is not likely to modify the electronic properties of phosphorene, and a diode like tunneling behavior is observed. Our results therefore clearly offer a possible route to tailor the electronic and magnetic properties of phosphorene by the adatom functionalization, and will be helpful to experimentalists in evaluating the performance and aging effects of phosphorene-based electronic devices.

4.3. Engineering phosphorene with strain: the formation of buckling

4.3.1. Introduction

Buckling is one of the most important mechanical phenomena in 2D materials including graphene which has elicited broad scientific interests [151-154]. Graphene possesses a high in-plane Young's modulus with sp^2 bonded carbon atoms [125], while it can easily be warped in the out-of-plane direction enabling folding [155], bending [156], corrugating [157] or wrinkling [158] without loss of its structural integrity [159]. This structural flexibility facilitates the fabrication of graphene-based complex structures with distinct functionalities [158]. Furthermore, buckling often appears in graphene grown from chemical vapor deposition (CVD) [160-162], and can be controlled via thermally activated shape-memory polymer substrates [163]. Similar buckling has also been observed in other 2D materials, such as hexagonal boron nitride (h-BN) [164], and molybdenum disulphide (MoS_2) [165, 166].

The mechanical properties of phosphorene under tensile strains have been investigated using both DFT calculations [167] and classical MD simulations [168]. The formation of ripples in phosphorene under a compressive strain has also been investigated via DFT calculations [169]. However, the previous DFT study on the ripples [169] was unable to capture the dynamical aspect of phosphorene membrane at finite temperatures, and the ripples were limited to small surface curvatures.

In this section, the buckling and its effect on the electronic properties of phosphorene are studied by classical MD simulations complemented by first-principles calculations based on DFT. The MD simulations allow us to investigate the dynamical process of buckling at large scale with modest computational resources. For the buckled configurations obtained by MD simulations, the

47

electronic properties are further determined by DFT calculations. The calculated results find that the buckling behavior of phosphorene can be described by Euler's buckling rule. More importantly, phosphorene shows superior out-of-plane structural flexibility along the armchair direction. The semiconducting and direct band gap nature are retained with buckling at large curvatures, which facilitates its application in flexible electronics and optoelectronics.

4.3.2. Computational methods

The classical MD simulations were performed using the large-scale atomic/molecular massively parallel simulator (LAMMPS) code [170]. In phosphorene, the interatomic interactions were characterized by the Stillinger-Weber (SW) potential [171]. The SW potential has been previously parameterized to correctly describe the mechanical properties of phosphorene [168]. In MD simulations, phosphorene membranes with different dimensions were considered and the periodic boundary conditions were applied to both the armchair and the zigzag directions.
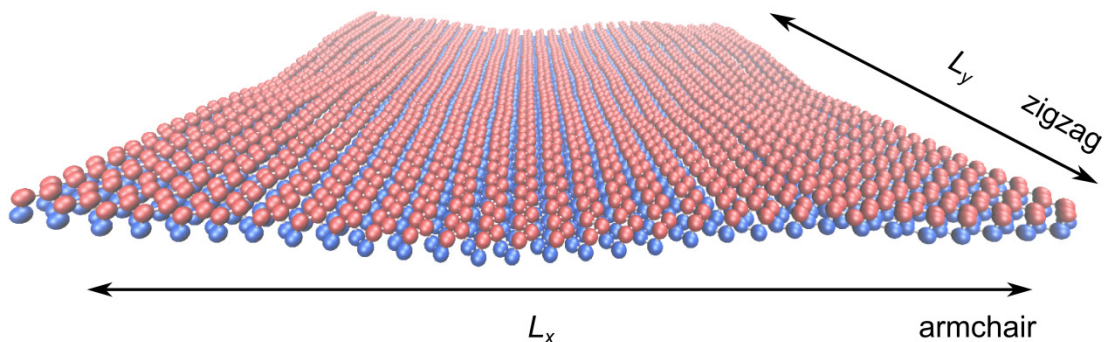
Figure 4.7 Snapshots of phosphroene at a thermally stable state at 300 K. L_x is the supercell size along the armchair direction, and L_y is the size along the zigzag direction. (Reprinted with permission from reference [172]. Copyright 2016 IOP Publishing.)

Figure 4.7 shows one snapshot of phosphorene membrane at a thermally stable state. Initially, the structure of phosphorene membrane was minimized using the SW potential. After minimization, the monolayer was equilibrated to a thermally stable state with the NVT (constant particle number, constant volume, and constant temperature) ensemble for 250 *ps*, followed by the NPT (constant particle number, constant pressure, and constant temperature) ensemble for 250 *ps*. After equilibration, phosphorene was compressed in either the armchair or zigzag direction with a strain rate of 10^{-4} *ps*$^{-1}$, while the stress in the lateral direction was allowed to relax. To eliminate the inter-layer interaction, simulation boxes with thickness of 10 nm were used. The temperature was set to 0.1 K or 300 K, the pressure to 0 bar, and the time step was set to 0.5 *fs*. The VMD [173] software package was used to visualize the simulation results. The strain is defined as the change of supercell size along the armchair or the zigzag direction ($\varepsilon = \frac{\Delta L_x}{L_x}, or \frac{\Delta L_y}{L_y}$).

Due to the structural anisotropy of phosphorene as shown in Figure 4.7, the buckling along the armchair and the zigzag direction is expected to be different. Thus, different samples with variable sizes as listed in Table 4.2 were used to simulate the buckling. The size of supercell along strain direction was varied from ~60 to 160 Å, while the size in the lateral direction was close to ~130 Å.

The electronic properties of the buckled phosphorene were obtained by DFT calculations using the norm-conserving Troullier-Martins pseudopotential as implemented in SIESTA [33]. The Perdew-Burke-Ernzerhof (PBE) [137] exchange correlation functional and a double-ζ basis including polarization functions were employed. Supercells of (30×1) and (1×30) were used for buckling along the armchair and the zigzag direction, respectively. The reciprocal space was sampled by a grid of (5×1×1) or (1×5×1) *k* points in the Brillouin zone, respectively. The buckled configurations with different curvatures obtained from the snapshots of LAMMPS simulations at 0.1 K were taken

as the initial configurations for DFT calculations. The energy convergence was set to 10^{-5} eV for electronic self-consistency steps. The mesh cutoff energy was 500 Ry. The geometry optimization was considered to converge when the residual force on each atom was smaller than 0.01 eV/Å. The atoms were allowed to relax during the structural optimization, while the size of the supercell was fixed. Note that lattice constants obtained by the SW potential along the armchair and the zigzag direction (4.38 Å and 3.31 Å, respectively) are in agreement to those obtained from the DFT calculations (4.57 Å and 3.31 Å, respectively).

Table 4.2. The size of the supercell in terms of L_x and L_y used for MD calculations. The unit is Å. (Reprinted with permission from reference [172]. Copyright 2016 IOP Publishing.)

	supercell	14×40	16×40	18×40	21×40	23×40	25×40	28×40	30×40	32×40	35×40
Armchair	L_x	61.2	69.9	79.0	92.3	100.5	109.1	122.4	131.3	139.8	153.3
	L_y	132.6	132.6	132.6	132.6	132.7	132.6	132.6	132.6	132.6	132.6
	supercell	30×19	30×22	30×25	30×28	30×31	30×34	30×37	30×40	30×43	30×47
Zigzag	L_x	131.2	131.2	131.4	131.8	131.1	131.1	131.2	131.3	131.2	131.3
	L_y	63.0	72.9	82.9	92.9	102.8	112.7	122.7	132.6	142.6	155.9

4.3.3. Results and conclusions

Figure 4.8 shows the structural evolution of phosphorene with the applied compressive strain (ε) along the armchair and the zigzag directions at 300 K. With small ε, phosphorene maintains a flat surface with small ripples due to thermal vibrations. Buckling starts with slightly larger strains applied along both directions. Further increasing the magnitude of ε results in the deformation of

phosphorene with enhancement of buckling height in the out-of-plane direction. Interestingly, the structural integrity of phosphorene is preserved even under a large strain along the armchair direction, while the bonds are broken at a large strain along the zigzag direction (Figure 4.8(b)).
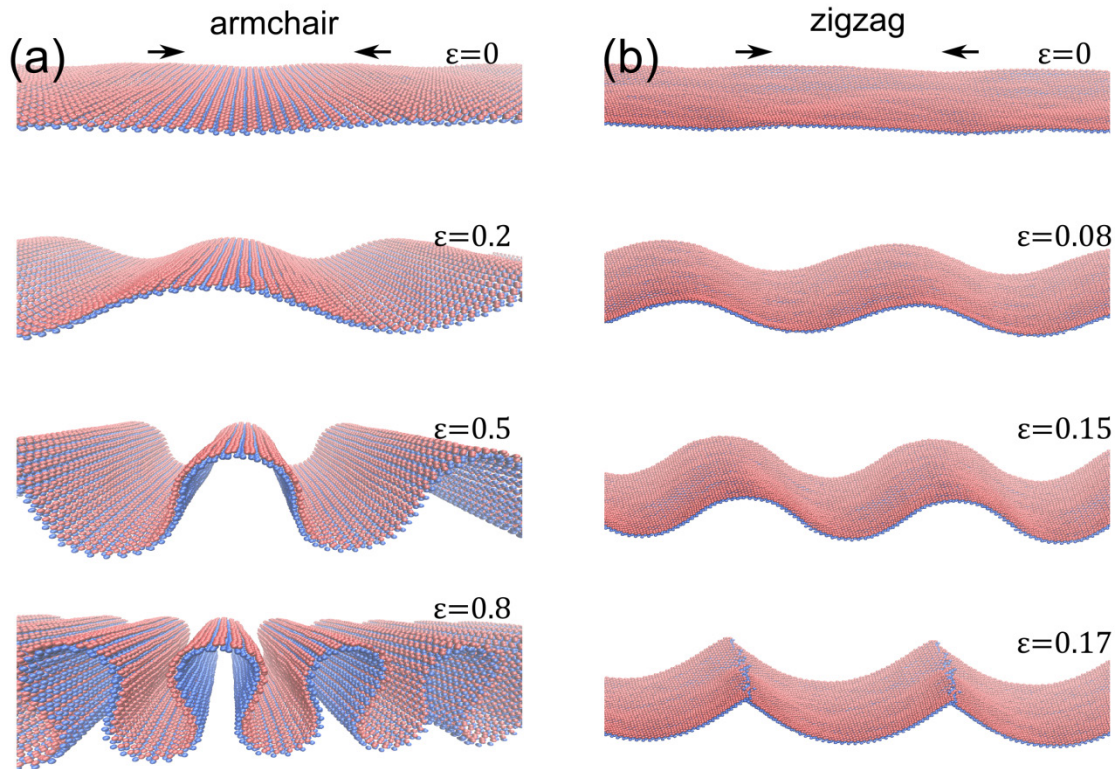
Figure 4.8 Snapshots of phosphroene (cell size=(30×40)) under in-plane compressive strain (ε) at 300 K: (a) strain along armchair direction, (b) strain along zigzag direction. The structures are shown in periodic manner along strain direction. (Reprinted with permission from reference [172]. Copyright 2016 IOP Publishing.)

The difference in buckling along the armchair and the zigzag direction stems from its structural anisotropy. As seen in Figure 4.7, the phosphorous atoms are arranged in a puckered lattice along the armchair direction. The puckered structure could accommodate external strains by changing the pucker angle without much distortion of the bond length, thereby giving rise to its structural flexibility. This is also the origin of the superior mechanical properties of phosphorene under tensile

strains [167]. However, in the zigzag direction, the phosphorus atoms are bonded into a zigzag chain like structure (Figure 4.7) which offers reduced flexibility.
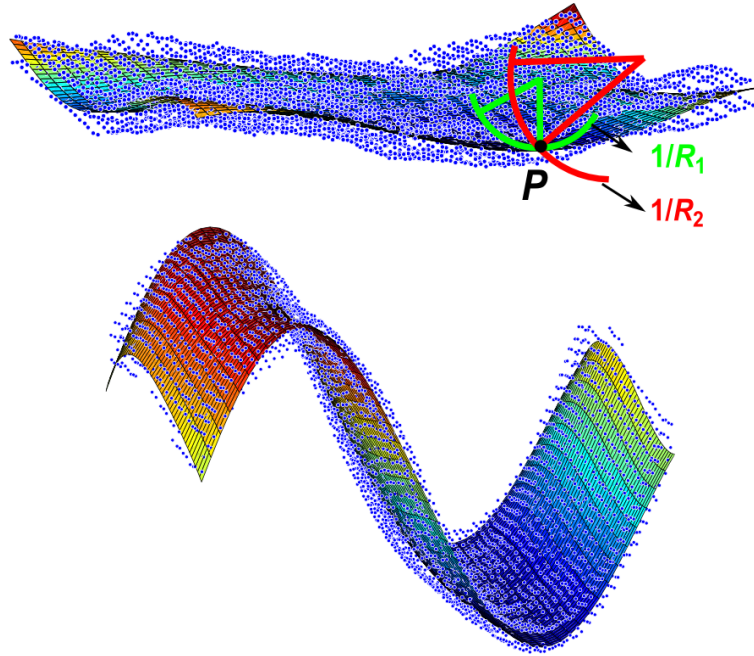
Figure 4.9 Polynomial fitting of phosphorene surface. The blue dots are phosphorus atoms. The mean curvature at each point P is calculated on the fitted surface. $1/R_1$ and $1/R_2$ are the principle curvatures at P point. The mean curvature is defined as $\frac{1}{2}\left(\frac{1}{R_1}+\frac{1}{R_2}\right)$ at each point. (Reprinted with permission from reference [172]. Copyright 2016 IOP Publishing.)

To quantitatively describe the buckling behavior, we calculate the curvature of phosphorene membrane as illustrated in Figure 4.9. Since phosphorene has two sub-layers of phosphorus atoms, a polynomial fitting of the surface yields the principle curvatures at each point of the surface. The mean curvature at each point (P) on the surface is defined as half of the sum of the principle curvatures, $\frac{1}{2}(\frac{1}{R_1}+\frac{1}{R_2})$, where $\frac{1}{R_1}$ and $\frac{1}{R_2}$ are the principle curvatures.
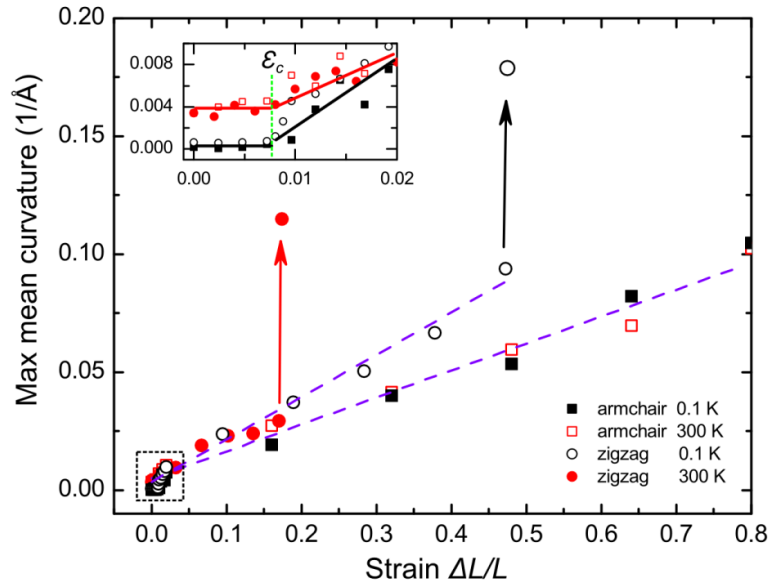
Figure 4.10. Maximum mean curvature of phosphorene (cell size=(30×40)) under compressive strains along the armchair (square) and the zigzag directions (circle) at a temperature of 0.1 K (black) or 300 K (red). The solid lines are guides to the eye. The arrow represents the break of the structure along zigzag direction with an abrupt increase of the maximum mean curvature. The inset is the zoomed in plot in the small strain region in the dashed box, the dashed line in the inset corresponds to the buckling critical strain. (Reprinted with permission from reference [172]. Copyright 2016 IOP Publishing.)

Figure 4.10 shows the change of maximum mean curvature of phosphorene under a compressive strain along the armchair and the zigzag directions. It has distinct trends for the cases of $\varepsilon < \varepsilon_c$ and $\varepsilon > \varepsilon_c$, where ε_c is the critical strain for the formation of buckling as illustrated by the vertical dashed line in the inset.

For $\varepsilon < \varepsilon_c$, as shown in the inset of Figure 4.10, the maximum mean curvature is almost unchanged along both the armchair and the zigzag directions, which corresponds to the elastic response of the membrane to external strain. During this process, the surface keeps almost flat with small vibrations due to thermally excited ripples. For $\varepsilon > \varepsilon_c$, the maximum mean curvature starts to increase, which corresponds to the formation of buckling. The mean curvature increases linearly with the strain on

phosphorene. The buckling critical strain ε_c is ~0.007 along armchair and zigzag directions for the sample with supercell size of (30×40).
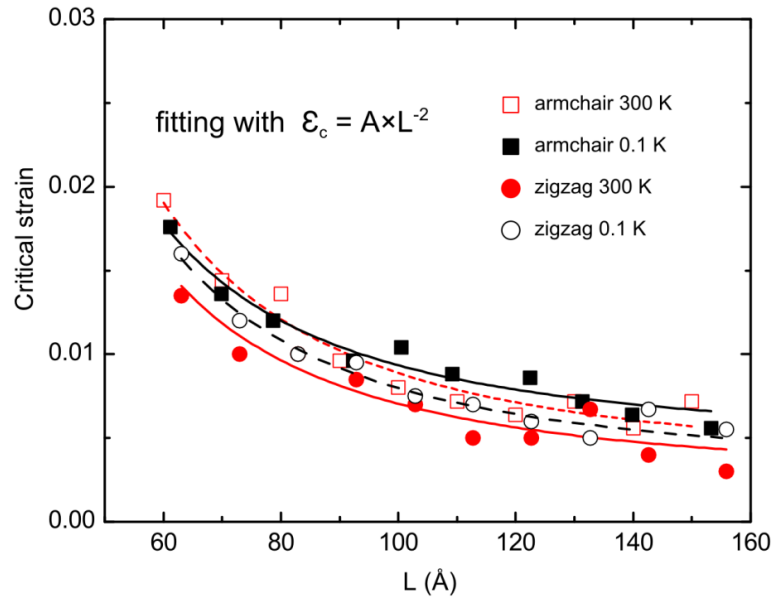
Figure 4.11 Buckling crictial strain vs the size of the simulation sample. The lines are fitted curve according to the Euler's buckling theory. (Reprinted with permission from reference [172]. Copyright 2016 IOP Publishing.)

The buckling curvature along the armchair direction linearly increases with ε up to 0.8 inducing the formation of folded phosphorene without breaking the structural integrity (see also in Figure 4.8(a)), which suggests its flexibility along the armchair direction. In the zigzag direction, an abrupt increase appears in the maximum mean curvature curve (illustrated by arrows in Figure 4.10), which corresponds to the breaking of the structure with abrupt release of stress (see also in Figure 4.8(b)). The breaking strain of the structure at 0.1 K is 0.47, which decreases to 0.17 at 300 K. Therefore, a large strain along the zigzag direction will break the structural integrity of phosphorene.
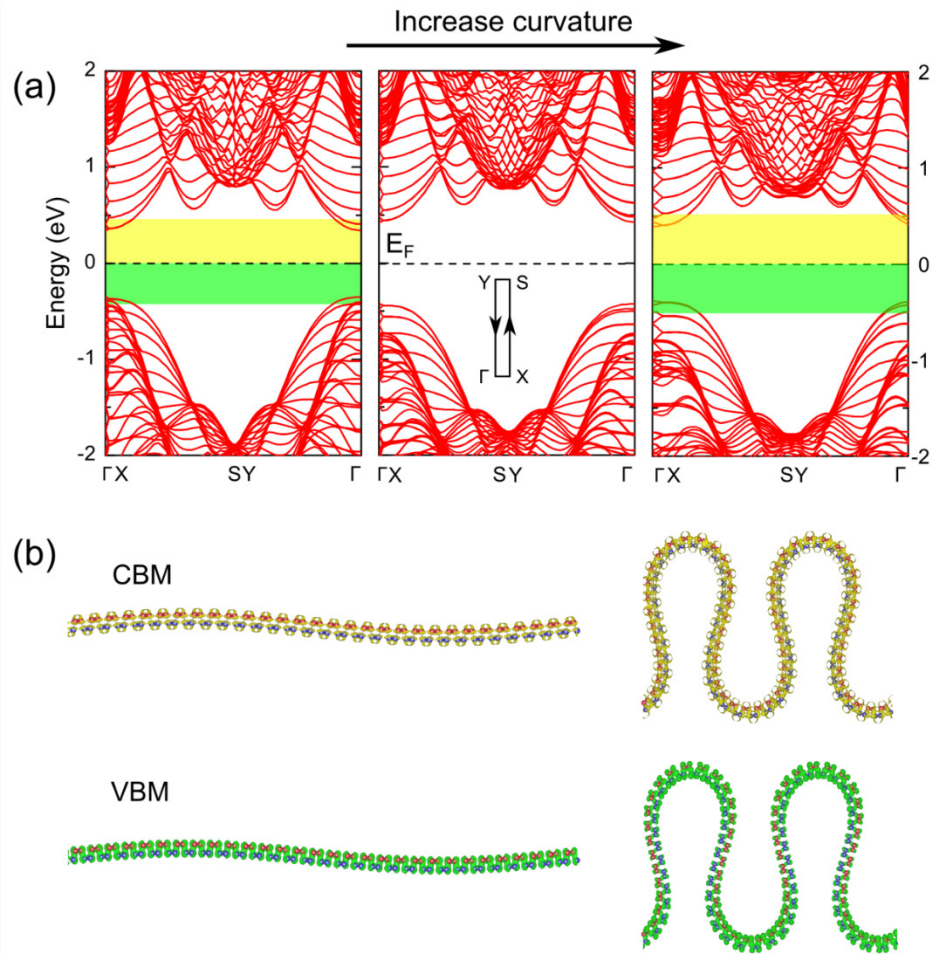
Figure 4.12 Electronic properties of phosphorene with buckling along armchair direction: (a) band structures at different curvature, (b) charge density at valence band maxiamim (VBM) and conduction band minimum (CBM). The inset is the Brillouin zone. (Reprinted with permission from reference [172]. Copyright 2016 IOP Publishing.)

According to Euler's buckling theory [174], a thin plate will experience buckling due to a compressive strain applied on it. The buckling critical strain is an inverse quadratic function of the length of the plate, $\varepsilon_c \propto -\frac{1}{L^2}$, where L is the length of the plate. The length dependence of buckling critical strain for various samples is summarized in Figure 4.11. The critical strain decreases with the increase of

the sample size in both the armchair and the zigzag directions, which can be well fitted with Euler's

buckling rule, $\varepsilon_c \propto -\frac{1}{L^2}$.
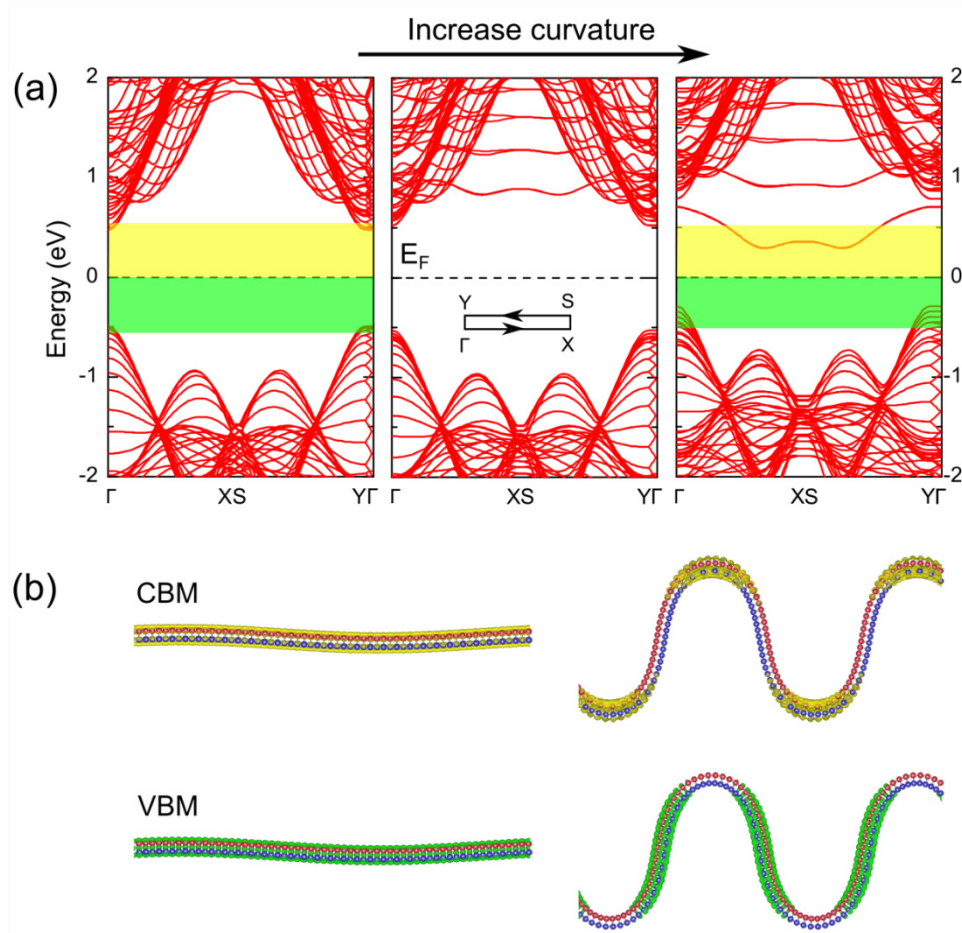
Figure 4.13 Electronic properties of phosphorene with buckling along zigzag direction: (a) band structures at different curvatures, (b) charge density at VBM and CBM. The inset is the Brillouin zone. (Reprinted with permission from reference [172]. Copyright 2016 IOP Publishing.)

In order to investigate the electronic properties of buckled phosphorene, DFT calculations were

performed on the buckled structures with various curvatures obtained at the classical MD

simulations. Note that the buckled structures at low temperature were chosen to enable the fast

convergence during DFT calculations. Strain-free phosphorene has a direct band gap of ~1 eV in our calculations, which agrees with the previously predicted values [11, 175].

Figure 4.12 shows the band structures and charge density at conduction band minimum (CBM) and at valence band maximum (VBM) with buckling along the armchair direction. Low buckled phosphorene has a direct band gap at Γ. The charge density at VBM and CBM are evenly distributed over the surface as seen in Figure 4.12 (b). The semiconducting property, direct band gap, and evenly distributed charge density are retained in largely buckled phosphorene suggesting the electronic robustness of phosphorene to the buckling along the armchair direction.

As seen in Figure 4.13, low buckled structure along the zigzag direction has a direct band gap, the charge density at VBM and CBM is evenly distributed over the surface as expected. Upon increase in the curvature of buckling, some conduction states approach Fermi level, thus reducing the band gap and thereby inducing a direct-indirect band gap transition. The decrease of the band gap with increasing curvature has also been predicted in a recently published report on non-planar phosphorene [176]. We observe unevenly distributed charge density at VBM and CBM at large curvature. The conduction states contributing to the decrease of the band gap come from the convex region of the buckled surface due to accumulated local strains in these regions (Figure 4.13 (b)). Therefore, compared to the buckling in the armchair direction, buckled phosphorene along the zigzag direction is less robust in terms of the structural and electronic properties of a candidate two-dimensional material for device applications.

4.3.4. Summary
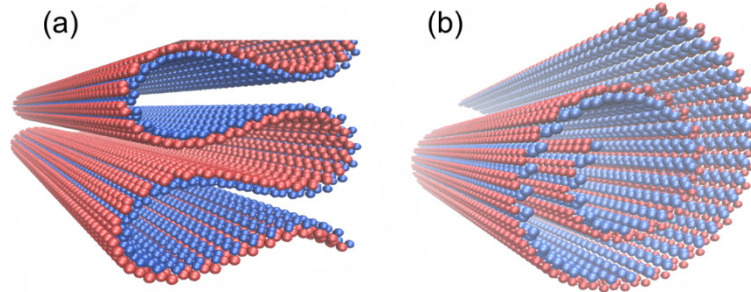
Figure 4.14. (a) Folded phosphorene, and (b) phosphorene nano-scroll. (Reprinted with permission from reference [172]. Copyright 2016 IOP Publishing.)

In summary, we investigate buckling in phosphorene under compressive strains by using classical MD simulation combined with first-principles calculations. A few interesting results are obtained from present study. (i) Buckling will form in phosphorene unsder a compressive strain along the armchair and the zigzag direction. The buckling critical strain satisfies the Euler's buckling theory. (ii) Phosphorene shows superior out-of-plane structural flexibility along the armchair direction, which allows the formation of buckling with large curvature; the buckling along the zigzag direction may break the structural integrity at large curvatures. (iii) The semiconducting and direct band gap nature of phosphorene are robust with the formation of buckling along the armchair direction; while buckling with large curvature along the zigzag direction will induce a direct to indirect band gap transition. The out-of-plane structural flexibility and electronic robustness of phosphorene along the armchair direction allow the fabrication of phosphorene based devices with complex shapes, such as folded structures and nano-scrolls in Figure 4.14. Also, the tunability of the band gap by the curvature along the zigzag offers great potential for electronics and optoelectronics device applications. Our results contribute to the understanding of mechanical properties of phosphorene, and guide the design of phosphorene-based devices for flexible electronics and optoelectronics.

Chapter 5   Group V elemental 2D materials – oxidation and degradation of phosphorene[*]

5.1.   Introduction

In the previous chapter, the properties of phosphorene and engineering of its properties with external defects and strain are discussed. Although phosphorene is a promising material among the 2D material family, it is found to be chemically unstable in air [161, 177, 178], which presents challenges for its synthesis, characterization and integration into active devices. The degradation of phosphorene is related to its interaction with oxygen and water in the air. In this chapter, I will first explore the oxidation of phosphorene by molecular oxygen and propose the possible formation of phosphorene oxides. Then, the degradation of phosphorene will be discussed in terms of its interaction with O_2 and H_2O.

5.2.   Formation of phosphorene oxide

5.2.1. Introduction

The chemical modification of 2D materials has now routinely been performed to tailor their physical, chemical and electronic properties. In the case of graphene, surface modifications by H, O, and F atoms often lead to substantial changes in its electronic structure. For example, H- and F-functionalized graphene are wide band gap materials, whereas graphene has zero-gap at the Dirac point [179-181]. Also, graphene oxides are the structures with the presence of the oxygen functional

---

[*] The contents in this chapter were previously published in Nanoscale, 2015, 7, 524-531 and 2D Mater, 2016, 3, 025011. Refer Appendix E for granted permission to be republished.

groups on graphene which show remarkable mechanical strength and tunable optoelectronic properties and have broadly used for large scale fabrication of graphene [182-184].

In this section, I will first look into the interaction of oxygen in both atomic and molecular form with the bare phosphorene predicting the preferred binding site and energy barrier to dissociate the oxygen molecule adsorbed on the monolayer. The effect of the coverage of oxygen on the stability and electronic structure of phosphorene will be examined latter. Then, the electron transport properties of the oxide configurations are calculated in a model setup mimicking the Scanning Tunneling Microscopy (STM) experiment.

5.2.2. Computational methods

Electronic structure calculations were performed using the density functional theory (DFT) method with the norm-conserving Troullier-Martins pseudopotential as implemented in SIESTA [33]. The Perdew-Burke-Ernzerhof (PBE) [137] exchange correlation functional was employed. A double-ζ basis including polarization orbitals was used. The energy convergence was set to 10^{-5} eV. The mesh cutoff energy was chosen to be 500 Ry. The geometry optimization was considered to be converged when the residual force on each atom was smaller than 0.01 eV/Å. In our periodic supercell approach, the vacuum distance normal to the plane was larger than 20 Å to eliminate interaction between the replicas. A dipole correction was employed to eliminate the artificial electrostatic field between the periodic supercells.

For calculations describing interaction of an O atom and an O_2 molecule with phosphorene, we used a (3×4) supercell with a total of 48 phosphorus atom in the cell and the reciprocal space was sampled by a grid of (5×5×1) k points in the Brillouin zone. On the other hand, PO, P_2O_1 and P_4O_1 configurations were calculated with a (1×1) supercell consisting of 4 phosphorus atoms, and the

P_8O_1 configuration was calculated with a (1×2) supercell consisting of 8 phosphorus atoms in the cell. The *k*-point mesh of (11×11×1) was used for these oxide configurations. The phonon dispersion calculation was based on Vibra of SIESTA utility [185].

Phosphorene has a puckered surface due to the sp^3 character of the chemical bonds at the surface. We find the bond lengths and the bond angles to be (2.29, 2.26 Å), (103.7°, 95.6°) which are in agreement with the previously reported values obtained at the PBE-DFT level of theory [15, 186]. Likewise, calculations using the same modeling elements reproduced the structural and electronic properties of graphene-based systems [111, 187], thereby showing accuracy and reliability of our computational model in describing 2D materials.

5.2.3. Results and conclusions

Monoatomic Oxygen (O)

Figure 5.1 shows the lattice sites considered for the oxygen approaching phosphorene e.g. (i) the ring site - above the center of hexagonal ring, (ii) the top site - above the top of P atom, and (iii) the bridge site - above the bridge of P-P bonds. Interestingly, O atoms approaching either top or ring sites prefer the same equivalent positions in their equilibrium configurations having tetrahedral coordination for P atoms.

In the equilibrium configuration, $R_{(P-O)}$ is ~1.54 Å, and the bridge site configuration is ~2.3 eV higher in energy. The predicted most stable configuration and bond length are the same to the result in section 4.2. Notice that the equilibrium configuration is in contrast to the case of graphene oxide where the bridge site is found to be the preferred binding site for oxygen [188].
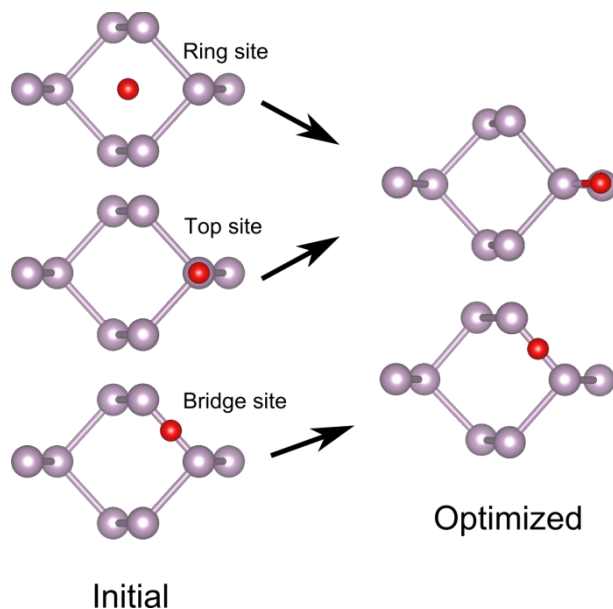
Figure 5.1 Single oxygen atom absorption on phosphorene. The left panel shows the initial configurations and the right panel shows the optimized configurations. The oxygen atoms are in red, and phosphorus atoms in purple. (Reprinted with permission from reference [189]. Copyright 2015 Royal Society of Chemistry.)

Molecular Oxygen (O$_2$)

Next, the interaction of an oxygen molecule with phosphorene is investigated by considering both adsorption and dissociation processes on the surface. Figure 5.2(a) shows the calculated ground state configuration of the adsorbed oxygen molecule. Here, O$_2$ prefers a tilted orientation with $R_{(P-O1)}$=1.69 Å and $R_{(P-O2)}$=1.75 Å. Note that the adsorbed O$_2$ gets stretched out on the surface with $R_{(O-O)}$ of 1.60, which is substantially larger than that of O$_2$ (~1.24 Å). The binding energy defined as ($E_{(Phosphorene)}$+$E_{(O2\ molecule)}$ − $E_{(Phosphorene+O2\ molecule)}$) is found to be about 0.78 eV/oxygen molecule. The binding energy of an oxygen molecule is smaller than the binding energy of two separated oxygen atoms due to the energy needed to stretch the $R_{(O-O)}$ to 1.60 Å. Note that the spin polarization was considered for the binding energy calculations.
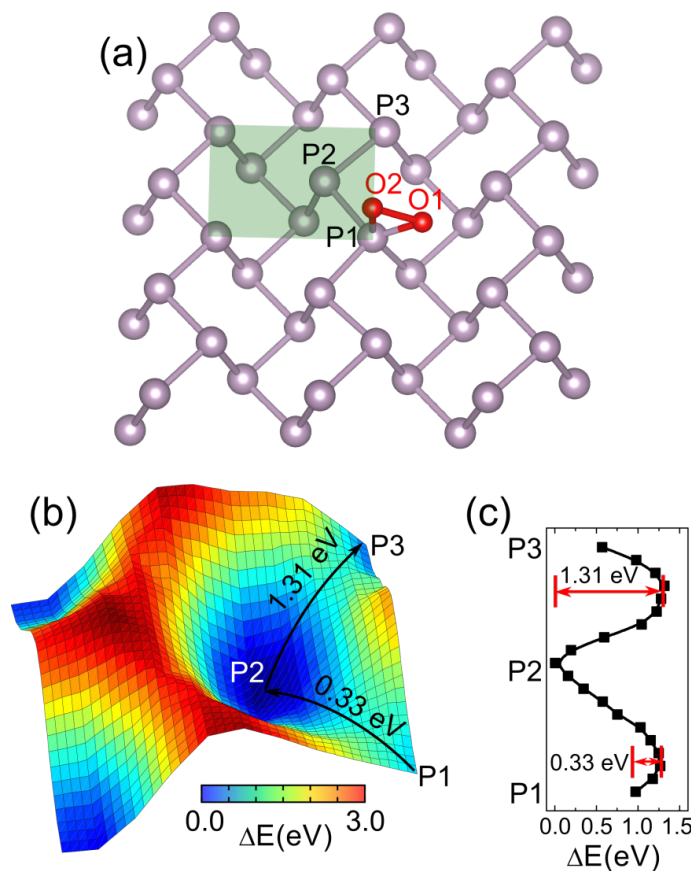
Figure 5.2 O₂ on phosphorene: (a) the ground state configuration, (b) the energy surface showing displacement of an O atom from P1 to P2 to P3 atomic sites, and (c) the calculated energy barrier along the paths as shown by the arrows in (b). The oxygen atoms are in red, and phosphorus atoms in purple. (Reprinted with permission from reference[189]. Copyright 2015 Royal Society of Chemistry.)

The dissociation process of the adsorbed O_2 is simulated by fixing an O atom (i.e. O1), and moving the other atom (i.e. O2) laterally in the unit cell (shadowed region) as shown in the inset of Figure 5.2(a). A minimum occurs in the corresponding energy surface as shown in Figure 5.2(b) when O2 moves toward the P2 site. The calculated energy barrier is 0.33 eV along the path illustrated by the arrows in the inset, Figure 5.2(c). The energy barrier increases to 1.31 eV when we move O2 to a new atomic site, P3. Note that the dissociation energy of an O_2 molecule on the bare graphene is about 2.39 eV [190], which is much larger than the dissociation energy of the O_2 molecule on

phosphorene (~0.3 eV). Dissociation of the adsorbed O_2 on phosphorene can therefore be one of the possible chemical routes to form the phosphorene oxide [191].

Stoichiometric phosphorene oxide (PO)

Phosphorene has a puckered surface (Figure 5.3(a)), and addition of an O atom at each atomic site leads to a configuration of PO with a slight increase in the P-P bond length (2.32, 2.37 Å) as compared those for the bare phosphorene. The length of P-O bond is 1.51 Å (Figure 5.3(b)) which is similar to the C-O bond length of 1.47 Å in graphene oxide [192], and is slightly larger than the distance between B-O of 1.40 Å for O_2 adsorbed on the B_{13} cluster [193].

As seen from the side view of Figure 5.3(b), PO is deformed compared to the bare phosphorene with changes in bond angles between P atoms. However, the structure retains its original configuration without cleavage of P-P bonds. This is different from the cases of H, F, and -OH absorption which act as chemical scissors and break down phosphorene into nanoribbons [194].

In the stoichiometric PO configuration, the $\angle$P-P-P bond angles are 121.2°, 93.6° and 100.9°. The change in the $\angle$P-P-P bond angles, relative to the bare phosphorene, is closely related to the charge redistribution. Analysis of the Mulliken charges finds that ~0.2 e is transferred from a P atom to an O atom. This is different from the case of graphene oxide where O tends to bind on the bridge of C-C bond forming epoxy groups, and the accumulated electron density around O comes from two neighboring C atoms of graphene [192, 195, 196].
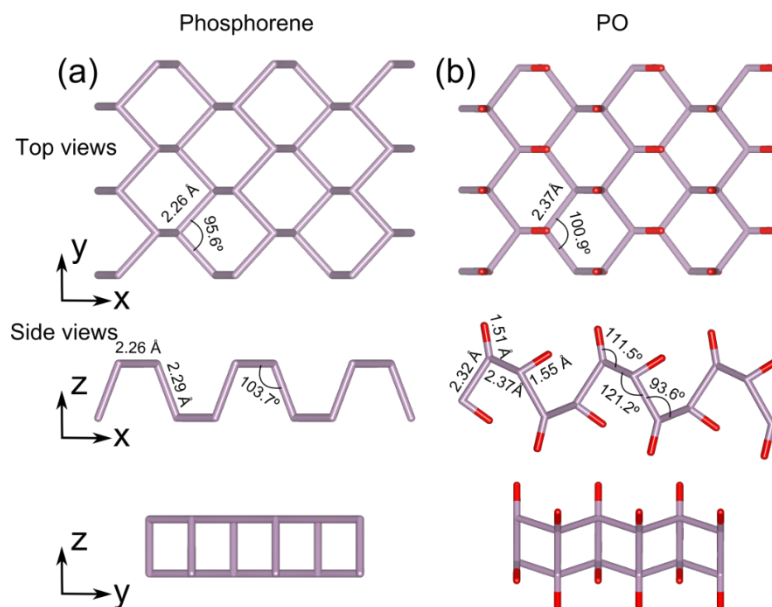
Figure 5.3 Top and side views of (a) phosphorene, and (b) phosphorene oxide. (Reprinted with permission from reference[189]. Copyright 2015 Royal Society of Chemistry.)

The stability of the phosphorene oxide is confirmed by the calculated phonon dispersion curves showing no negative frequencies (Figure 5.4). The phonon dispersion of PO is greatly different from that of phosphorene; it can be grouped into three regions (Figure 5.4(b)) with the highest vibrational frequency of about ~1160 cm^{-1}. On the other hand, the phonon dispersion curves of the bare phosphorene have separated acoustic and optical modes with the maximum vibrational frequency of ~460 cm^{-1}. In the lower acoustic region for PO, the vibrational modes are associated with the constituent P and O atoms. The modes associated with the P atoms dominate in the middle region of the spectrum. The high frequency modes correspond to the P-O stretching modes indicating a relative high strength of the P-O bond in the 2D lattice.
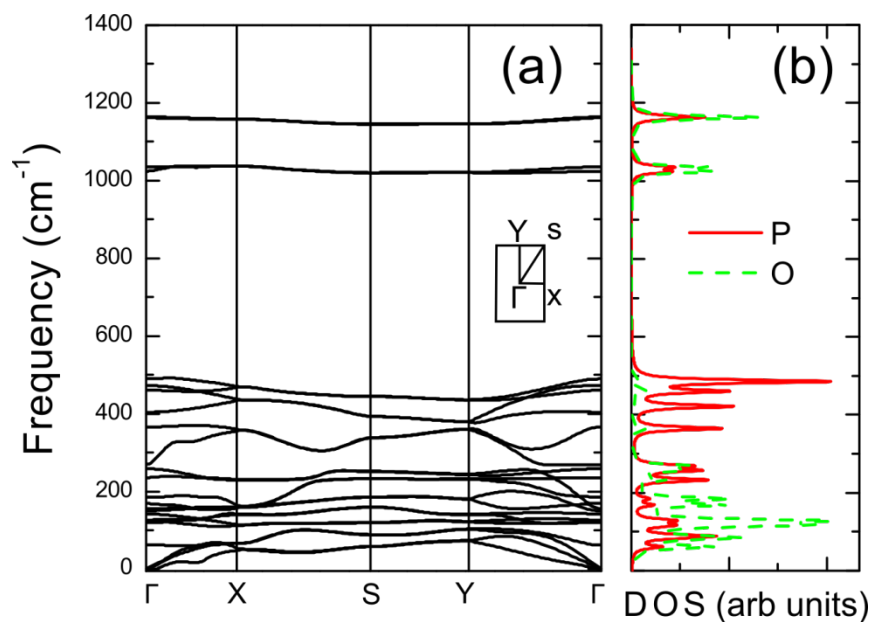
Figure 5.4 Phosphorene oxide (a) the phonon dispersion curves, and (b) density of states. (Reprinted with permission from reference [189]. Copyright 2015 Royal Society of Chemistry.)

In our study, we consider the oxygen adsorption on phosphorene to be more-like an ordered absorption of adsorbates on graphene, such as the case of graphane, fluorographene, and chlorographene [180, 181, 197]. In graphene oxide, the oxygen functional groups form a inhomogeneous lattice as revealed by the transmission electron microscopy (TEM) measurements [196]. This may be due to interaction of oxygen atoms at the top and bottom sides of graphene leading to clustering of oxygen atoms. A recent theoretical study predicts the formation of ordered, homogenous of single surface graphene oxides by oxidizing only the top layer of graphene [188]. A formation of the homogenous graphene oxides is also observed after the oxidation of epitaxial graphene grown on a SiC substrate [198].

The calculated band structure of PO is shown in Figure 5.5. The valence band maximum (VBM) has p_y character associated with both P and O atoms (Figure 5.5(c)), and the conduction band minimum (CBM) is formed by P-s orbitals and O-p_z orbitals (Figure 5.5(c)). The calculated band

gap is direct at Γ with a value of ~0.6 eV. It is smaller in magnitude than that calculated for the

bare phosphorene (~1 eV at the PBE-DFT level of theory). Anisotropy in the band structure of the

2D lattice is predicted; the hole effective masses are 4.56 and 1.74 m_e along Γ-X and Γ-Y directions,

respectively. On the other hand, the electron effective mass does not show anisotropy and has a

magnitude of 0.18 m_e.
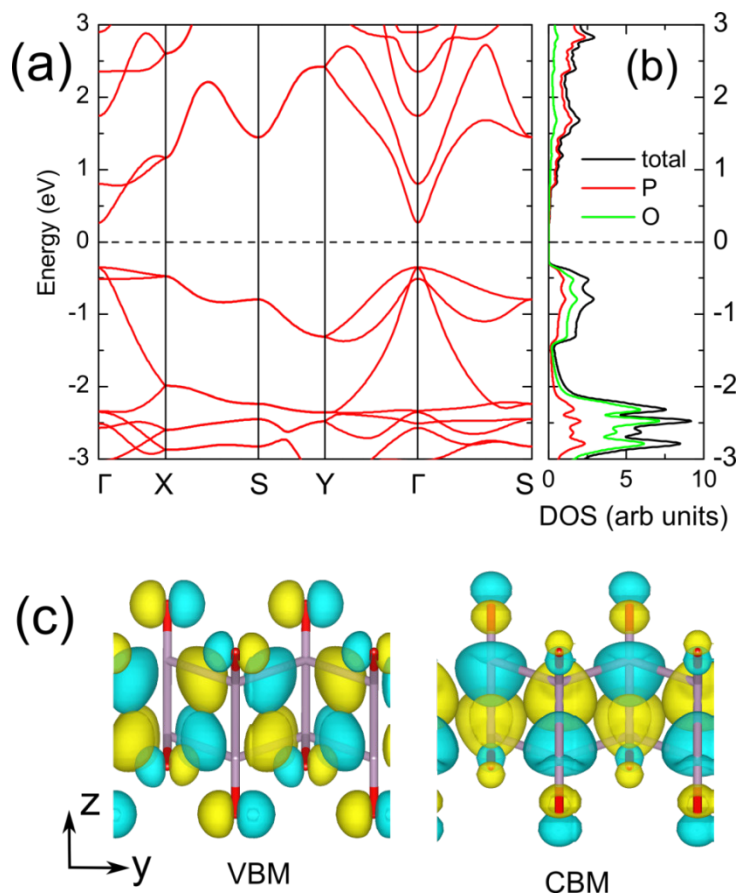
Figure 5.5 Electronic properties of phosphorene oxide: (a) band structure, (b) density of states, and (c) Kohn-Sham wave functions at Γ associated with states corresponding to top of the valence band (VBM) and bottom of the conduction band (CBM). (Reprinted with permission from reference [189]. Copyright 2015 Royal Society of Chemistry.)
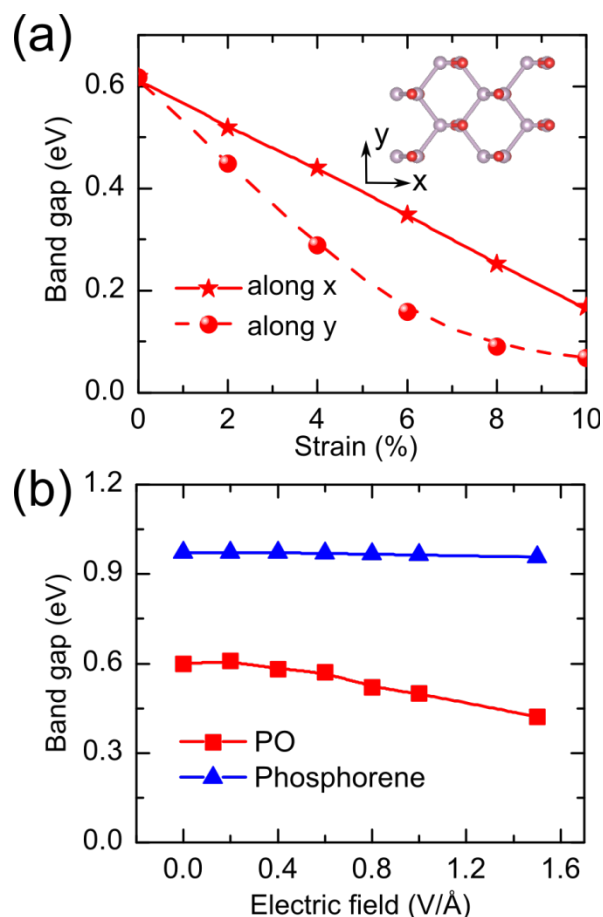
Figure 5.6 Phosphorene oxide: Band gap vs. in-plane tensile strain, and (b) band gap vs. electric field applied perpendicular to the 2D lattice. (Reprinted with permission from reference [189]. Copyright 2015 Royal Society of Chemistry.)

Application of the strain along *x* yields a linear variation of the band gap in a range of values (0.1-0.6 eV) for the tensile strain values of 0% to 8% (Figure 5.6(a)). The predicted variation in the band gap is mainly due to variation of the conduction band minimum (CBM). The top of the valence band (VBM), mainly formed by the oxygen atoms, does not appear to be sensitive to the external strain. Likewise, the external electric field modifies the band gap reducing it to be 0.4 eV at 1.5 V/Å, while it does not change the band gap in the bare phosphorene (Figure 5.6(b)). This is due to the reduced symmetry in the oxide configuration compared to its bare configuration. Thus, the

oxygen functionalization of phosphorene yields tunability of the band gap with both strain and electric field.

The in-plane stiffness of the 2D lattice is calculated by fitting the strain energy within the strain range of -2% to 2% [111]. The calculated stiffness constant for phosphorene is 21 and 66 N/m along x and y directions, respectively. For the phosphorene oxide, the stiffness constant is decreased to 16 and 33 N/m along x and y directions due to the increased P-P bond length in the oxide lattice. These values are much smaller those associated with graphene (340 N/m [125]) which suggest the softness of phosphorene-based 2D materials [199].

Non-stoichiometric phosphorene oxide

We now investigate stabilities and electronic properties of non-stoichiometric phosphorene oxides representing the cases of the partial functionalization of the phosphorene. Figure 5.7 shows the considered non-stoichiometric oxide configurations including P_8O_1 (i.e. $PO_{0.125}$), P_4O_1 (i.e. $PO_{0.25}$), and P_2O_1 (i.e. $PO_{0.5}$), with a single side absorption of the oxygen atoms.

Figure 5.8 shows the variation of the band gap with the degree of the functionalization of phosphorene. Bare phosphorene is a direct gap 2D material. This is not the case with phosphorene oxides where the nature of the band gap depends on the degree of functionalization; an indirect band gap is predicted for $PO_{0.125}$, $PO_{0.25}$, and $PO_{0.5}$. Finally, a crossover from indirect to direct band gap is seen for the stoichiometric PO configuration. The direct band gap is defined as the energy gap at Γ and the indirect band gap is the minimum energy gap from VB to CB.
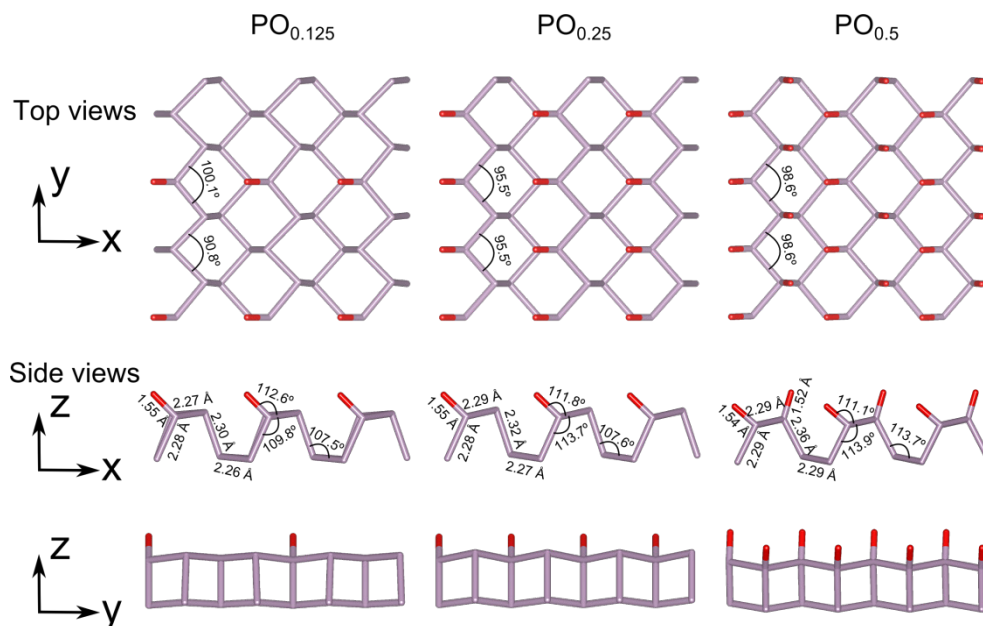
Figure 5.7 Structures of non-stoichiometric oxide configurations: $PO_{0.125}$, $PO_{0.25}$, and $PO_{0.5}$. (Reprinted with permission from reference [189]. Copyright 2015 Royal Society of Chemistry.)

The work function is a crucial physical quantity to determine the emission properties of materials and have considerable impact on device performance. It is defined as energy difference between the vacuum level and Fermi energy. For the oxide configurations, the work function shows a monotonous increase which is expected with the increased degree of oxygen functionalization of the bare phosphorene. This is due to the fact that the charge transfer from P to O will lead to formation of dipoles between the phosphorus layer and oxygen layer, thus preventing electrons moving toward the vacuum [200]. The calculated values of the work function for bare phosphorene, $PO_{0.125}$, $PO_{0.25}$, $PO_{0.5}$, and PO are 4.5, 4.9, 5.2, 5.8, and 7.2 eV, respectively. Therefore, the work function can be tailored effectively with the degree of oxygen functionalization of phosphorene. Similar tunable work function has already been reported for graphene; the work function increases from 4.2 eV to 5.5 eV with 20% concentration of oxygen functionalization [200, 201].
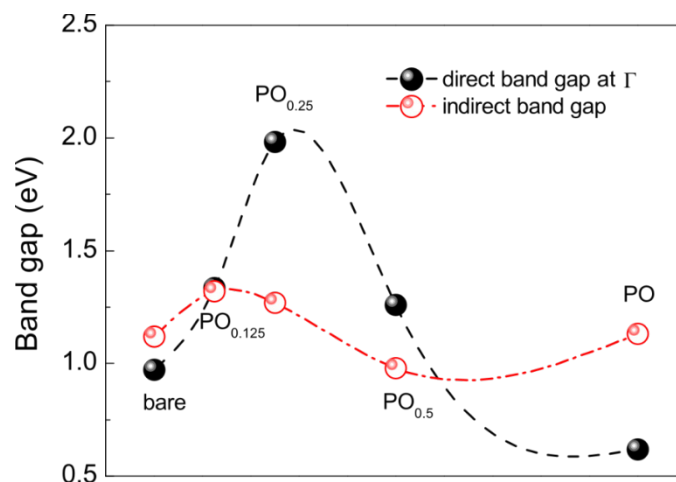
Figure 5.8 The variation of band gap as a degree of functionalization of the bare phosphorene. Open and solid circles represent the values of indirect and direct band gaps, respectively. The direct band gap is taken to be at Γ. The indirect band gap for P, $PO_{0.125}$, $PO_{0.25}$, $PO_{0.5}$ and PO are the minimum energy gap between CB and VB. (Reprinted with permission from reference [189]. Copyright 2015 Royal Society of Chemistry.)

Tunneling characteristics

Finally, the tunneling characteristics of the phosphorene oxides are investigated. The tunneling current from the sample to the tip at location $\vec{r}_t$ based on the Tersoff and Hamann approximation [140] is

$$I(\vec{r}_t; V) \approx \frac{2\pi e}{\hbar} \int_{-\infty}^{+\infty} \rho_t \left(E - \frac{eV}{2}\right) \rho_s \left(\vec{r}_t; E + \frac{eV}{2}\right) F(E) dE, \qquad (5.1)$$

where ρ_t is the electron density of the tip, ρ_s is the electron density of the sample at the location of the tip. $F(E)$ is the term to include the effect of thermally excited electrons as proposed by He *et al*. [149, 150] In order to mimic the scanning tunneling micriscope (STM) measurements, we use the constant current mode with the gold tip represented by a Au_{13} cluster. The size of the STM images is 20 Å×20 Å, and a positive bias between the sample and the tip was applied. It is to be noted here

71

that a positive bias between the sample and the tip will lead to tunneling of electrons from tip-VB to sample-CB. With a negative bias, the electrons will tunnel from sample-VB to tip-CB.
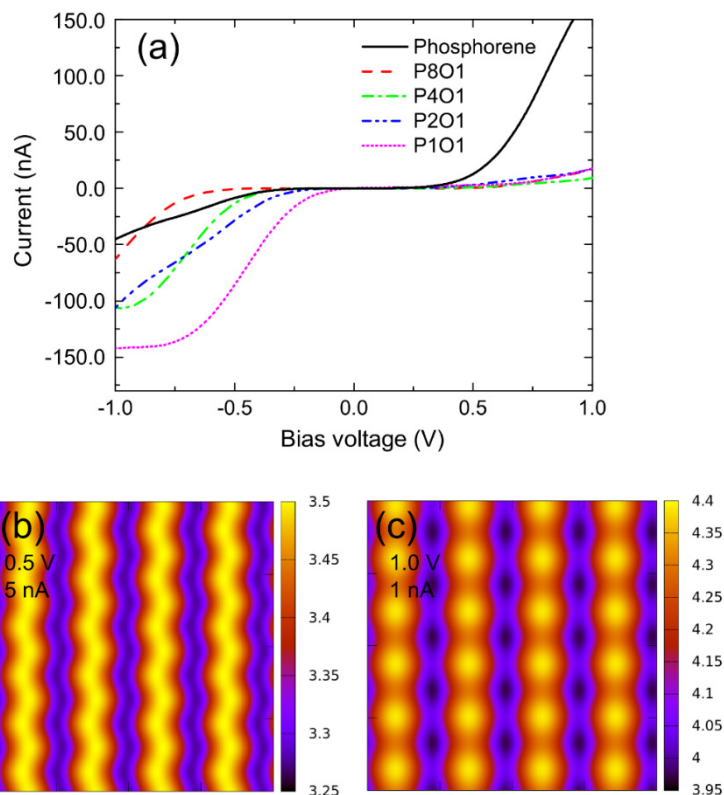
Figure 5.9 (a) Tunneling characteristics of the phosphorene oxide configurations. (b) The simulated STM images of phosphorene and the phosphorene oxide. The current is calculated using a Au13 tip located at 3 Å above the surface. The side scale bar shows the distance from the tip to the surface in unit of angstrom. (Reprinted with permission from reference [189]. Copyright 2015 Royal Society of Chemistry.)

The electron transport studies offer some intriguing insight into electron tunneling in the direction perpendicular to the stable phosphorene oxide plane. Asymmetric current-voltage (IV) semiconducting characteristics (Figure 5.9(a)) are seen for both stoichiometric and non-stoichiometric oxide configurations. To start, a bare phosphorene shows strong diode like behavior with large tunneling current in the positive bias regime. Upon oxygen adsorption, this behavior

completely changes, with high current in the negative bias regime. The high tunneling current of PO in the negative bias region is due to the contribution of oxygen atoms in the top of valance band (Figure 5.5(b)).

The dependence of the threshold voltage onset of the tunneling current on the degree of functionalization suggests that tunable electronic properties can be achieved by the oxygen functionalization of phosphorene. In the negative bias region, the threshold voltage decreases from -0.55 V (P_8O_1) to -0.15 V (PO) which is related to variation in the band gap of oxides. Furthermore, the STM images as seen in Figures 5.9 (b) and (c) can help in identifying formation of the phosphorene oxide from the bare phosphorene.

5.2.4. Summary

The interaction of phosphorene with oxygen and the formation of 2D phosphorene oxide were investigated with the use of the density functional theory. A number of key findings have emerged from this study based on density functional theory. First, our calculations predict that the 2D phosphorene oxide to be stable in both stoichiometric and non-stoichiometric configurations. Second, a fully functionalized phosphorene is a direct band gap material with tunable band gaps by external strain and electric field. Partially functionalized phosphorene has an indirect band gap. Third, the dissociation energy of an oxygen molecule is calculated to be ~0.33 eV, suggesting possible, low-energy oxidation of phosphorene which is likely to lead to the 2D phosphorene-based structures. Finally, electron transport studies offer some intriguing insight into electron tunneling in the direction perpendicular to the phosphorene oxide plane with dependence of the current on the degree of functionalization of phosphorene. We believe that the results of this study would

73

inspire experimental efforts into the synthesis and electronic device physics studies of phosphorene oxide.

5.3. Degradation of phosphorene in air

5.3.1. Introduction

The chemical degradation of phosphorene upon exposure to ambient conditions is a challenge to the stability and performance of phosphorene-based devices [161, 177, 178]. The presence of oxygen and humidity is suggested to be the main cause of the degradation process [139, 202, 203]. Recent experiments have also demonstrated the photo-assisted degradation of phosphorene [204], which is predicted to be related to intrinsic defects [205]. Theoretically, it was reported that H_2O adsorbed on phosphorene will induce a significant distortion to its structure [206]. Contradictory results were obtained suggesting that phosphorene is stable in the presence of H_2O [207]. Despite these experimental and theoretical efforts, there are still some unanswered questions regarding the degradation of phosphorene, including (i) atomic level of understanding on the degradation process of phosphorene; (ii) the role of H_2O in the degradation process; and (3) the environmental stability of other theoretical phosphorene allotropes (e.g., blue phosphorene [208] which has not been realized in experiments).

In order to address these questions, density functional theory (DFT) calculations combined with *ab initio* molecular dynamics (AIMD) simulations were performed to investigate the interactions of O_2 and H_2O with phosphorene. We first focus on the interaction of O_2 with phosphorene using AIMD. Since surface reaction of black phosphorene with O_2 has established in the previous section, we will extend the discussion to blue phosphorene. Then, the adsorption of H_2O on phosphorene allotropes is investigated in terms of adsorption configuration, binding energy, and bonding characteristics. Finally, we discuss the degradation of phosphorene by calculating the relative

energies along a likely interaction pathway. Our calculated results show that O_2 can spontaneously dissociate on phosphorene at room temperature; H_2O will not strongly interact with pristine phosphorene, however, an exothermic reaction could occur if phosphorene is first oxidized. Other allotropes of phosphorene, e.g. blue phosphorene are also expected to deteriorate in air.

5.3.2. Computational methods

The electronic structure calculations were performed using the Vienna *ab initio* simulation package (VASP) [30, 31]. The exchange-correlation was treated within the generalized gradient approximation (GGA) using Perdew−Burke−Ernzerhof (PBE) [137] functional for the calculations. We also employed the DFT-D2 method of Grimme [209] to include contributions from the van der Waals (vdW) interactions. The energy of convergence was set to 1×10^{-6} eV and the residual force on each atom was smaller than 0.01 eV/Å during the structural optimization. The cutoff energy for the plane-wave basis was set to 500 eV. The vacuum distance normal to the plane was larger than 30 Å to eliminate interaction between the periodic replicas. A rectangular supercell of (3×4) was used for the black phosphorene, and a parallelogram supercell of (4×4) was used for the blue phosphorene. The reciprocal space was sampled by a grid of (2×2×1) *k* points in the Brillouin Zone.

First principles molecular dynamics (MD) simulations were also performed to simulate the interaction processes considered. The MD simulation was based on the norm-conserving Troullier-Martins pseudopotential together with Nosé thermostat[210] as implemented in the SIESTA program package[33]. In order to minimize the constraints induced by periodicity in the slab model for MD simulations, (5×6) and (5×5) supercells were used for black and blue phosphorene, respectively. The time step was set to 1 *fs*, and the simulation temperature was set to 300 K. It is to be noted that most of the experiments on degradation of phosphorene were done in the air. In our MD

simulations, the number density of gas molecules was about $65.8 \times 10^{25}/m^3$ considering 9 O_2 molecules in a simulation cell of (22.9 Å × 19.9 Å × 30 Å). Such high pressure conditions were also used for MD simulations to study oxidation of SiC[211] and graphene [212].

5.3.3. Results and discussions

Black phosphorene has a puckered surface with two sub-layers of phosphorus atoms which are arranged in a rectangular lattice. At GGA-PBE level of theory, the lattice constants along the armchair and the zigzag direction are 4.57 Å and 3.31 Å, respectively. The bond lengths are 2.22 Å and 2.25 Å. Blue phosphorene has a buckled honeycomb structure with lattice constant of 3.28 Å and bond length of 2.26 Å. Our results are in agreement with the reported lattice constants and bond lengths of black and blue phosphorene [175, 208], thereby, demonstrating the reliability of the modeling elements used in the calculations.

O_2 interacting with phosphorene
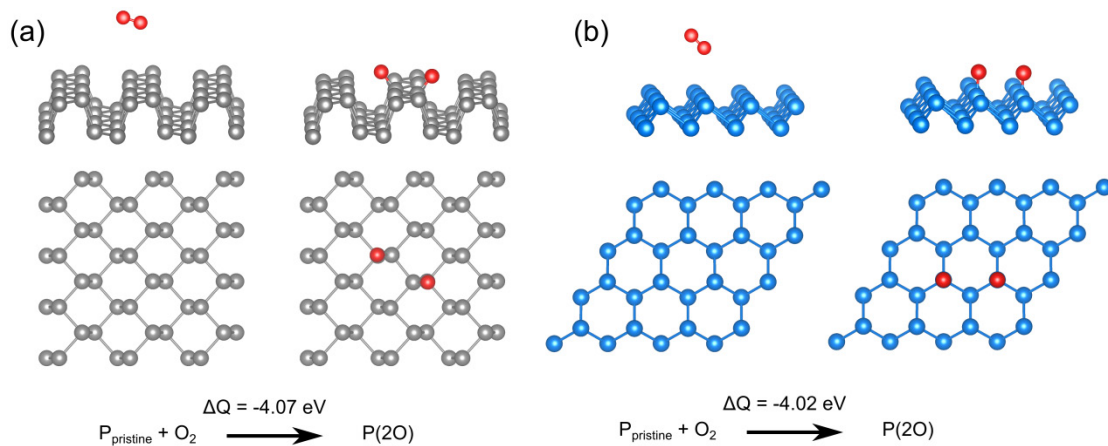
Figure 5.10 O_2 dissociation on phosphorene: (a) black phosphorene, (b) blue phosphroene. P(2O) represents black or blue phosphorene with two O adatoms. (Reprinted with permission from reference [213]. Copyright 2016 IOP Publishing.)

Table 5.1. Structural properties of atomic O adsorbed on phosphorene. (Reprinted with permission from reference [213]. Copyright 2016 IOP Publishing.)

Phosphorene	Black	Blue
Bond length R_{P-O} (Å)	1.50 Å	1.50 Å
Bond angle $\angle$P-P-O (°)	112°, 117°	123°
Bader charge, Oxygen	-1.31e	-1.32e

From section 5.2, we know that that O_2 can easily dissociate on black phosphorene [139, 214] leading to the formation the oxidized lattice [189]. As shown in Figure 5.10, O_2 tends to dissociate on the surface with exothermic energy (ΔQ) of -4.07 eV/O_2 molecule on black phosphorene, and -4.02 eV/O_2 molecule on blue phosphorene. Note that the dissociation energy is obtained by comparison with the most stable triplet O_2.

Ziletti et al. have found the dissociation barrier of O_2 on phosphorene is only 0.54 eV [139]. Considering that chemical reaction with an energy barrier less than 0.9 eV ($\approx$21 kcal/mol) from DFT calculations could occur at room temperature [215], the oxidation of phosphorene is expected to occur readily at room temperature. Other external sources such as photon radiation may speed up the dissociation process. After dissociation, atomic oxygen finds the dangling position to be the preferred site on black phosphorene which is consistent with previous theoretical studies [139, 142].

This is not the case with blue phosphorene where the preferred site is the top site. The P-O bond shows similar bonding character as seen from the bond length and Bader charges [216] given in Table 5.1. Overall, the nature of interaction of oxygen with phosphorene stems from the sp^3 bonds which leave a lone electron pair on each phosphorous atom, and the preferred binding site follows the direction of the lone electron pair on both allotropes.
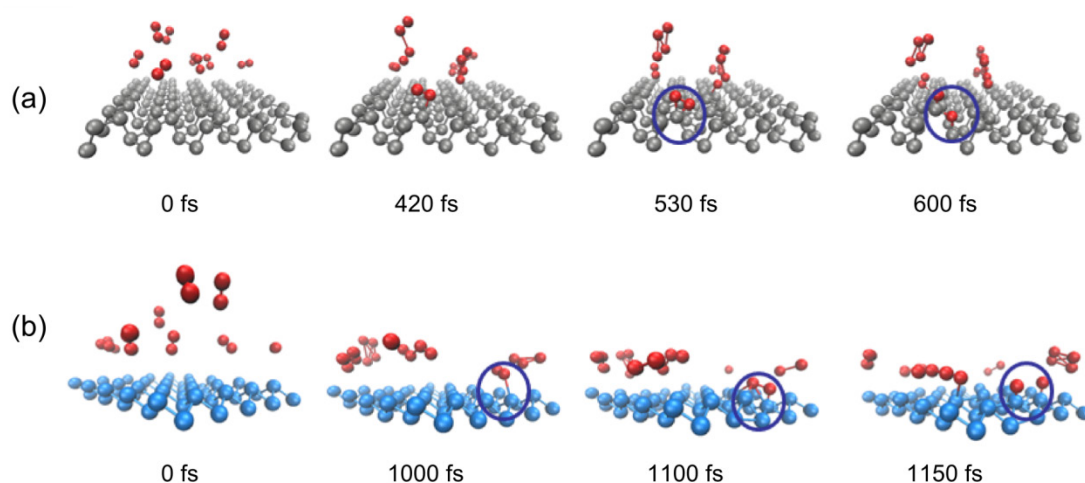
Figure 5.11 Snapshots of O_2 interacting with phosphorene during MD simulations: (a) black phosphorene, (b) blue phosphorene. Reprinted with permission from reference [213]. (Copyright 2016 IOP Publishing.)

The calculated results based on AIMD simulations further affirm the dissociation of O_2 on phosphorene. Figure 5.11 shows time-dependent snapshots of the configurations showing interaction of oxygen with phosphorene during MD simulations. These configurations were obtained by placing a few O_2 molecules 4 Å initially above the surface at a constant temperature of 300 K. For the case of black phosphorene, some O_2 molecules will first move closer to the native phosphorus atoms, then dissociate into atomic oxygen atoms after 600 fs. A similar O_2 dissociation process is seen on the blue phosphorene after 1150 fs.

Considering that we have used relatively high pressure conditions in our MD simulations, we have performed additional MD calculations with only one O_2 molecule in the simulation box of (22.9 Å × 19.9 Å × 85 Å) which appears to mimic number density of gas molecules of $2.5\times10^{25}/m^3$ under standard atmospheric conditions. The dissociation of O_2 on the surface does occur under the relatively reduced pressure conditions. We may therefore conclude that both allotropes of phosphorene will go through the spontaneous oxidation process upon exposure to O_2 at room temperature due to the affinity of P and O atoms forming P=O bonds with a large exothermic energy.

H_2O interacting with phosphorene

Figure 5.12 shows the configurations of H_2O interacting with phosphorene considered for the calculations: one leg, two leg, and O closer. The configuration referred to as "one leg" is the configuration in which one of the H atoms is closer to the surface, "two leg" means both H atoms are closer to the surface, and "O closer" means the O atom is closer to the surface.

The calculated binding energy profiles with vdW correction using DFT-D2 method of Grimme [209] are shown in Figure 5.13. Some of the results deduced are:

(i). The 'two leg' configuration is the most stable configuration suggesting that H atoms prefer to move towards the surface. This is due to the well-known polar nature of the H_2O molecule in which H atoms tend to attract the lone electron pairs of phosphorene.

(ii). The calculated binding energy including vdW correction term is about 180 and 125 meV for H_2O on the black and blue phosphorene, respectively. It is larger than that of H_2O on graphene

at the same level of theory (in the range from 60 to 120 meV [217]), mainly because of the presence of the lone electron pairs on phosphorene.
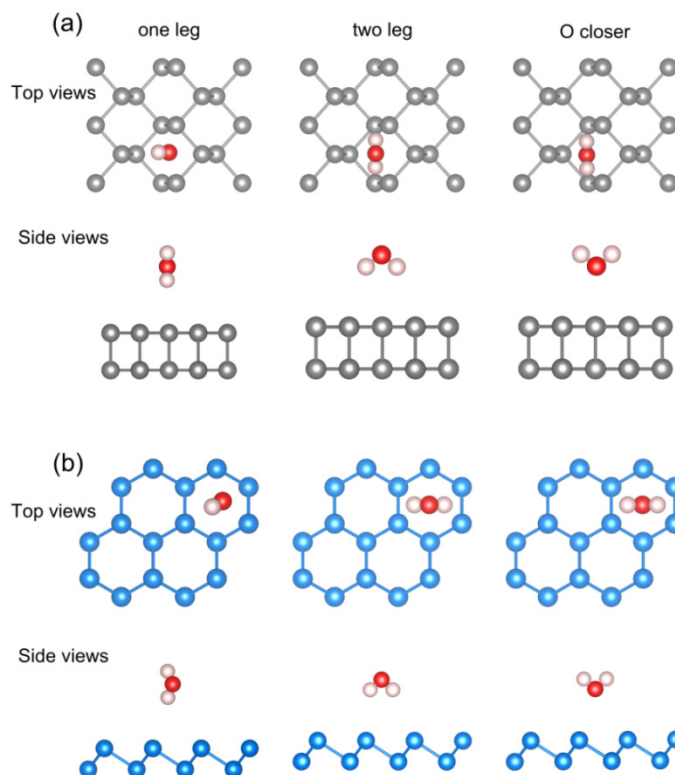
Figure 5.12 Top and side views of the configurations considered for H_2O interacting with phosphorene: (a) black phosphorene, (b) blue phosphorene. Reprinted with permission from reference [213]. Copyright 2016 IOP Publishing.)

In order to further examine the interaction of H_2O with phosphorene, we considered the initial configuration to consist of a "forced" H_2O molecule at the interstitial site of the phosphorene lattice. If H_2O prefers to interact strongly with phosphorene, then the optimized configuration should show that H and O atoms remain in the lattice. This is not the case as H_2O moves out of the lattice to a surface site without distorting the surface for both allotropes. Our first principles MD simulations up to 10 *ps* also find that H_2O molecules stay near the phosphorene surface without any chemical

interaction within 10 *ps*. Therefore, instead of strongly interacting with phosphorene, H_2O prefers to bind to the surface through hydrogen bonds.
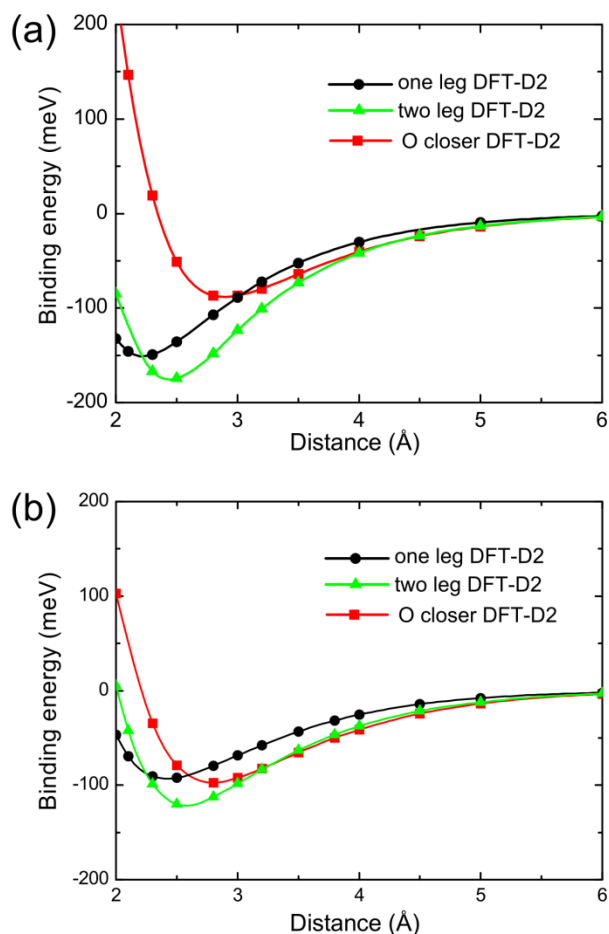
Figure 5.13 The calculated binding energy profiles of a H_2O molecule approaching phosphorene: (a) black phosphorene, (b) blue phosphorene. Reprinted with permission from reference [213]. Copyright 2016 IOP Publishing.)

Stability of phosphorene in air : Exposure to O_2 and H_2O

The dissociation of H_2O on pristine black and blue phosphorene is endothermic with energy increase of 1.24 eV and 1.37 eV, respectively (Figure 5.14). This is not the case with the oxidized phosphorene monolayers for which the endothermic energy significantly decreases to 0.26 eV and

0.48 eV, respectively. Therefore, oxidation of phosphorene may enable dissociation of H_2O on the surface. Also considering that the phosphorous oxides (e.g., P_3O_6, P_4O_{10}) are reactive with H_2O [218], a simple intuitive view of the degradation of phosphorene in air based on energetic considerations can be offered: first, oxidation of the 2D lattice of phosphorene will occur in air; then, the oxide species will interact with H_2O.
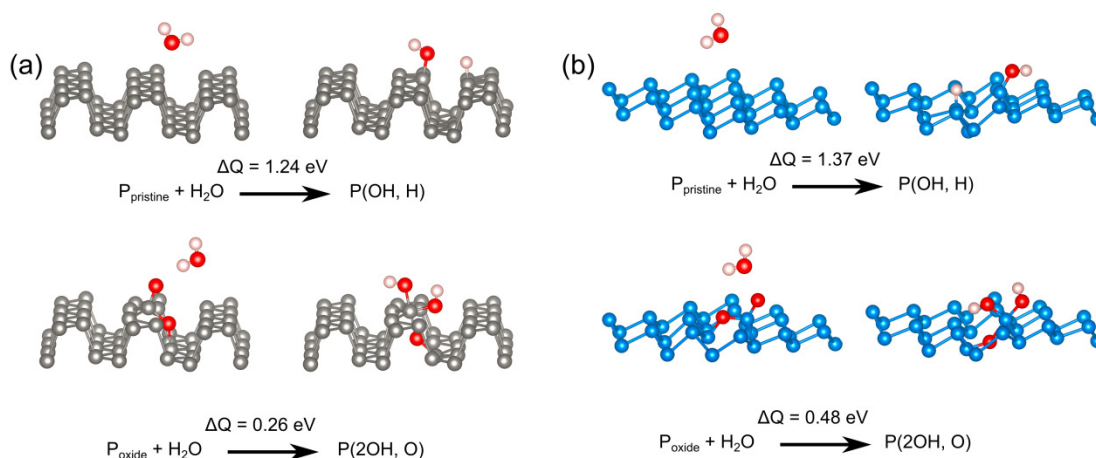
Figure 5.14 H_2O dissocation on pristine and oxide phosphorene: (a) black phosphorene, (b) blue phosphorene. P(OH,O) represents black or blue phosphorene with OH group and O adatom. (Reprinted with permission from reference[213]. Copyright 2016 IOP Publishing.)

In order to validate our view of this interaction process, the relative energy of the initial and final chemical species along the pathway are calculated. The reactants are phosphorene, 3 O_2 molecules, and 3 H_2O molecules and the products are 2 phosphoric acid and phosphorene with defects including di-vacancy and O adatom (Figure 5.15). For black phosphorene, the total energy release during this process is 15.60 eV. The oxidation process is exothermic with energy release of about 12.21 eV, and the reaction of phosphorene oxide species with 3 H_2O molecule further releases 3.39 eV of energy. The reaction process for blue phosphorene is also exothermic, which suggests the similarity of black and blue phases in terms of the environmental stability. Overall, the exothermic

process implies that H_2O will react with phosphorene if it is oxidized on the surface. The proposed

pathway will lead to the formation of phosphoric acid and defective phosphorene. The defective

phosphorene could further be photo-oxidized [205], and then the oxide species will further react with

H_2O. This reaction circle results in the fast degradation of phosphorene in air. Different from

graphene where the dangling bonds near the defects initiate its degradation[219], the degradation of

phosphorene is expected to occur without any initial intrinsic defects.
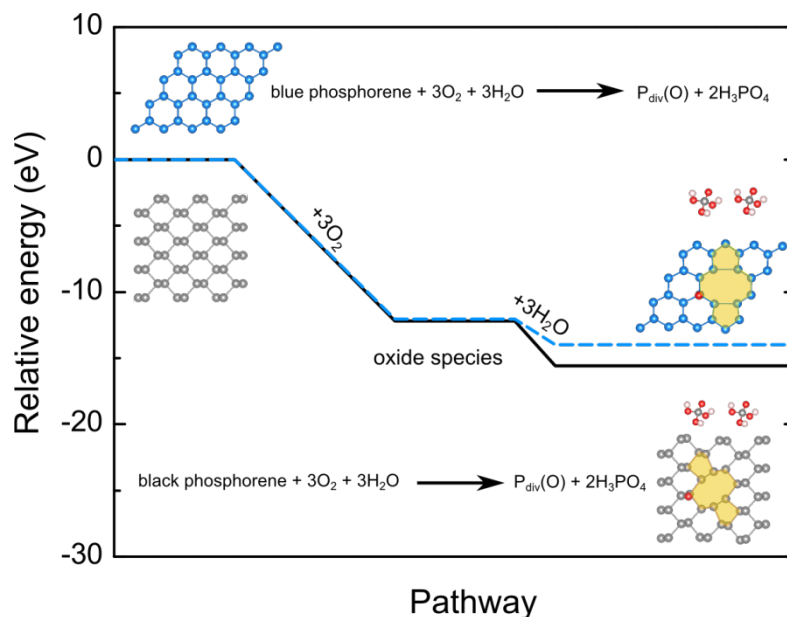
Figure 5.15 Relative energy during the interaction process of black (solid curve) and blue (dashed curve) phosphorene with O_2 and H_2O. The insets show the structure of initial phosphorene structure and the products. $P_{div}(O)$ represents defective phosphorene with one divacancy and one O adatom. (Reprinted with permission from reference [213]. Copyright 2016 IOP Publishing.)

5.3.4. Summary

In order to investigate the stability of phosphorene in air, the interaction of O_2 and H_2O with

phosphorene was studied by using density functional theory combined with first-principles

molecular dynamics simulations. We find that (i) O_2 will spontaneously dissociate on phosphorene

at room temperature. The exposure of phosphorene to O_2 will induce its oxidation forming an oxidized phosphorene lattice; (ii) H_2O does not interact directly (chemically) with the pristine phosphorene lattice. It prefers to bind to the surface of phosphorene though hydrogen bonds; (iii) H_2O will exothermically interact with phosphorene if it has first been oxidized; (iv) Other theoretically predicted 2D phosphorene allotropes, e.g. blue phosphorene, are also expected to be unstable in air.

Our calculations are supported by several experimental results; e.g. experiments have shown that fast degradation of phosphorene occurs with the existence of both O_2 and H_2O, the degradation process slows down with the exposure of phosphorene to only O_2 or H_2O [204, 220]; experiments have shown a drop of pH after water addition to phosphorene [221], which is a clear identification of the formation of phosphoric acid. Considering the rapid growth of research on 2D materials based on the group V semiconductors, our study provides an atomic scale understanding of the stability of phosphorene in air, which will aid in determining the degradation and aging effects of phosphorene-based devices.

Chapter 6   Group V elemental 2D materials – antimonene and its allotropes[*]

6.1. Introduction

Group-V elemental monolayers have recently emerged as novel two dimensional (2D) materials with semiconducting electronic properties. For example, the monolayer form of black phosphorous, phosphorene (α-P), has a direct band gap and high carrier mobility [13, 222], which can be exploited in the electronics [175, 223]. Additionally, the stability of phosphorene in the other allotropes including β, γ, and δ phases was predicted [186, 208]. The equilibrium configuration of α-P is puckered due to the intralayer sp^3 bonding character in the lattice. The 2D form of the so-called blue phosphorene is refereed to as β-P [208] which possesses the hexagonal honeycomb structure maintaining the sp^3 character of bonds. Each atom is three-fold coordinated forming silicene-like 2D structure with buckling at the surface [73]. γ-P and δ-P have rectangular Wigner-Seitz cells [224].

Considering the chemical similarity of elements belonging to the same column in the periodic table, the other group-V elemental monolayers have also been investigated. Arsenene in α and β phases is predicted to be stable [225, 226]. Ultrathin Bi (111) and Bi (110) films have been assembled on Si substrate or pyrolytic graphite in experiments [227, 228]. It is important to note that, unlike group-IV monolayers which are semi-metallic including graphene [229], silicene [73], and germanene [7], group-V monolayers are found to be semiconductors [225, 226, 230], thereby offering prospects for device applications at nanoscale.

In the bulk form, various allotropes exist for group-V elements at ambient conditions. For example, the most stable allotrope for P is black phosphorus which is composed of AB stacked α-P monolayers. Bulk black phosphorus possesses an intrinsic band gap of ~0.3 eV [222, 231] which increases to ~2 eV in its monolayer form [10]. The other group-V elements, As, Sb, and Bi, crystallize in a rhombohedral structure at ambient conditions, where the (111) direction is composed of ABC stacked β- phase monolayers [232].

In this chapter, I will focus on the 2D antimony (Sb), referred to as antimonene. Recently, Zhang et al. have shown that the Sb (111) films (i.e. β-Sb) undergo a thickness dependent transition from topological semimetal to topological insulator to normal semiconductor with decreasing thickness [232]. The semiconducting electronic properties of β-Sb monolayer is also confirmed by a recent theoretical investigation [233]. However, stability and electronic properties of antimonene in other allotropes (i.e. α, γ, and δ-Sb) have not yet been investigated.

We consider antimonene allotropes including α-, β-, γ-, and δ-Sb examining their stability by phonon dispersion calculations based on density functional theory (DFT). Furthermore, we will investigate the effect of mechanical strain on the electronic properties of antimonene allotropes. We will also calculate Raman spectra and scanning tunneling microscope (STM) images to gain further insights into the electronic structure and surface morphology.

6.2. Computational methods

The calculations were performed with the use of VASP program package [30]. We employed the local density approximation (LDA) together with the projector-augmented-wave (PAW) [234] method which has been shown to correctly describe Sb films [232]. For bulk Sb, our calculations find the

lattice constant of 4.31 Å is in excellent agreement with the experimental value of 4.30 Å [235] giving

confidence in the calculated results with the proposed approach based on the LDA-DFT level of

theory. To compare stability and structural parameters of different allotropes of antimonene, the

Perdew-Burke-Ernzerhof (PBE) [137] functional and the DFT-D2 method of Grimme [209] were also

employed to describe the weak vdW interaction.

In calculations, the energy convergence was set to 10^{-6} eV and the residual force on each atom was

smaller than 0.01 eV/Å. The cutoff energy for the plane-wave basis was set to 500 eV. The

reciprocal space was sampled by a grid of (15×15×1) k points in the Brillouin zone. The vacuum

distance normal to the plane was larger than 20 Å to eliminate interaction between the replicas due

to the period boundary conditions in the supercell approach of our model. The spin-orbit coupling

(SOC) was included in calculations for the band structure. The Phonopy code [40] was used for the

phonon dispersion calculation considering supercell of (4×5) for α-Sb, (5×5) for β-Sb, (5×4) for γ-

Sb, and (3×3) for δ-Sb. The non-resonance Raman spectra were obtained within density-functional

perturbation theory (DFPT) by second order response to an electric field as implemented in

Quantum Espresso [236]. The scanning tunneling microscope (STM) images are based on BTH

approximation [140], which has been successfully used to investigate tunneling characteristics of

several nanomaterials [142, 189].

6.3. Results and discussions

The structural configurations of antimonene allotropes are shown in Figure 6.1. The α-Sb has a

distorted atomic structure with two sub-layers, where atoms belonging to the same sub-layer are

not in the same planes (Figure 6.1(a)). The four atoms in the unit cell are arranged in a rectangular

lattice with a puckered surface. The calculated bond lengths are 2.83 and 2.91 Å and the calculated

bond angles are 95.0 and 102.5° at LDA-DFT level of theory for α-Sb (Table 6.1).
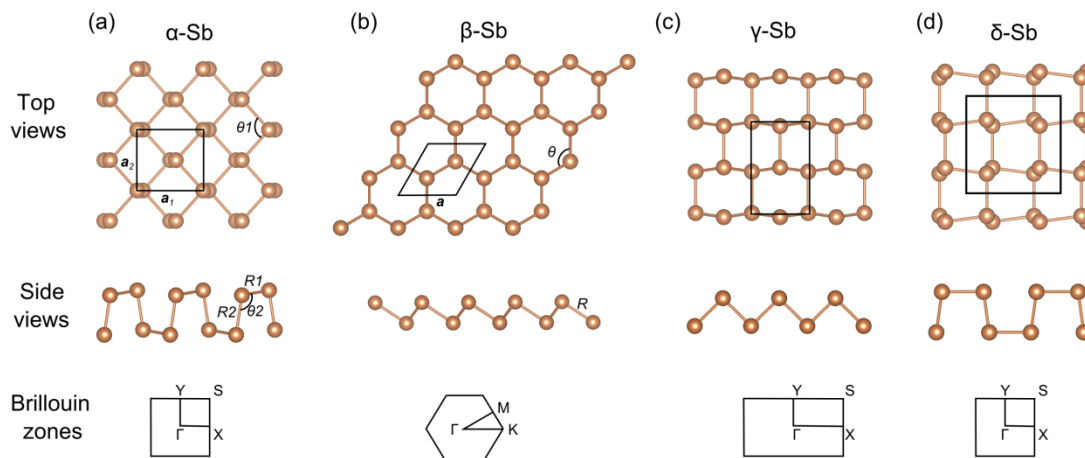
Figure 6.1 The structural configurations of antimonene allotropes: (a) α-Sb, (b) β-Sb, (c) γ-Sb, and (d) δ-Sb. (Reprinted with permission from reference [237]. Copyright 2015 American Chemical Society.)
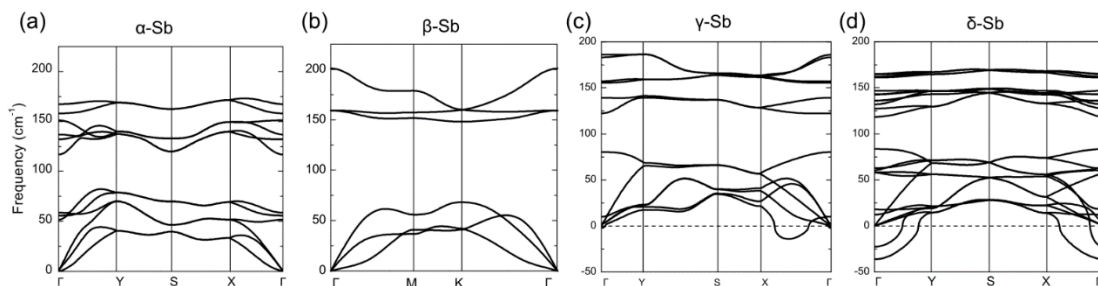
Figure 6.2 The calculated phonon dispersions of antimonene allotropes: (a) α-Sb, (b) β-Sb, (c) γ-Sb, and (d) δ-Sb. (Reprinted with permission from reference [237]. Copyright 2015 American Chemical Society.)

The ground state configuration of β-Sb mimics the metallic Sb (111) surface (Figure 6.1(b)). It has

a hexagonal lattice with the buckled surface similar to what was predicted for β-P. The bond length

between neighboring Sb atoms is 2.84 Å, and the bond angle is 89.9° (Table 6.1). The results are

in agreement with previous theoretical calculations on β-Sb monolayer [233, 238]. Similar to γ- and δ-

P [224], the γ- and δ-Sb have the rectangular unit cells which are shown in Figure 6.1(c) and (d). The

optimized bond lengths are 2.82 and 2.94 Å for γ-Sb, and the corresponding bond lengths are 2.87

and 2.93 Å for δ-Sb at LDA-DFT level of theory.

Table 6.1. The ground state structural parameters (see Figure 1) of antimonene allotropes: a is the lattice constant, R is the near-neighbor distance, θ is the bond angle, and Ec is the cohesive energy which is taken to be the total energy difference between the 2D material and its constituting atoms. (Reprinted with permission from reference [237]. Copyright 2015 American Chemical Society.)

Level of theory	α-Sb							β-Sb			
	a_1	a_2	R_1	R_2	θ_1	θ_1	E_c	a	R	θ	E_c
	(Å)	(Å)	(Å)	(Å)	(°)	(°)	(eV/atom)	(Å)	(Å)	(°)	(eV/atom)
LDA	4.48	4.31	2.83	2.91	95.0	102.5	-4.63	4.01	2.84	89.9	-4.57
GGA(PBE)	4.74	4.36	2.87	2.94	95.3	102.4	-4.03	4.12	2.89	90.8	-4.03
DFT-D2	4.77	4.28	2.86	2.91	94.6	103.5	-4.29	4.04	2.87	89.6	-4.26

The stability of these antimonene allotropes is first investigated by the calculation of the phonon

dispersion curves as shown in Figure 6.2. No imaginary vibrating mode is observed for α-Sb and

β-Sb illustrating their stability as the free-standing monolayers. The phonon dispersion curve of β-

Sb is similar to that of phosphorene with separated acoustic and optical modes. The maximum

vibrational frequency in α-Sb and β-Sb is 170 and 200 cm⁻¹, respectively. Our calculations show

that γ-Sb has imaginary mode along Γ-X, and δ-Sb has imaginary modes at Γ. Employing a larger

supercell model with higher convergence criteria also yielded imaginary frequencies for γ- and δ-

Sb, thus confirming their structural instabilities.

The stability of α- and β-Sb monolayers is further examined by the cohesive energy calculations at different levels of DFT. As listed in Table 6.1, α-Sb has larger cohesive energy than β-Sb at the LDA-DFT (≈60 meV) and DFT-D2 (≈30 meV) levels of theory, though both monolayers are nearly degenerate at GGA(PBE)-DFT level of calculation.
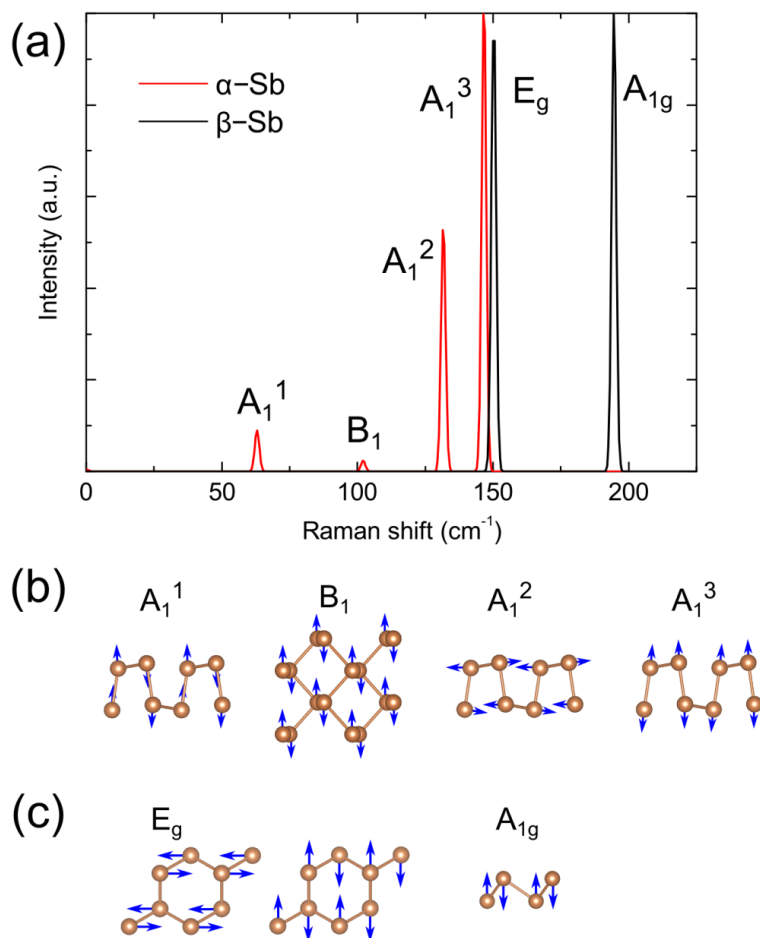
Figure 6.3 The calculated Raman spectra (a) and the corresponding vibrational modes of antimonene allotropes (b and c). (Reprinted with permission from reference [237]. Copyright 2015 American Chemical Society.)

The phonon free energy difference in the temperature range of 0-600 K is calculated to be less than 15 meV/atom between α-Sb and β-Sb suggesting stabilization of both monolayers in experiments.

Interestingly, a crossover in the cohesive energies of α-Sb and β-Sb multilayers at 3 atomic layers is predicted which suggests that β-Sb is more stable than α-Sb in multilayers with more than 3 atomic layers. The thickness dependent phase transition is mainly due to the stronger interlayer interaction in β multilayers (as will be shown later), resulting into their stability over α-Sb multilayers. The experimental results on ultrathin Bi films show stability of β-Bi over α-Bi for films with thickness more than 4 atomic layers [239].
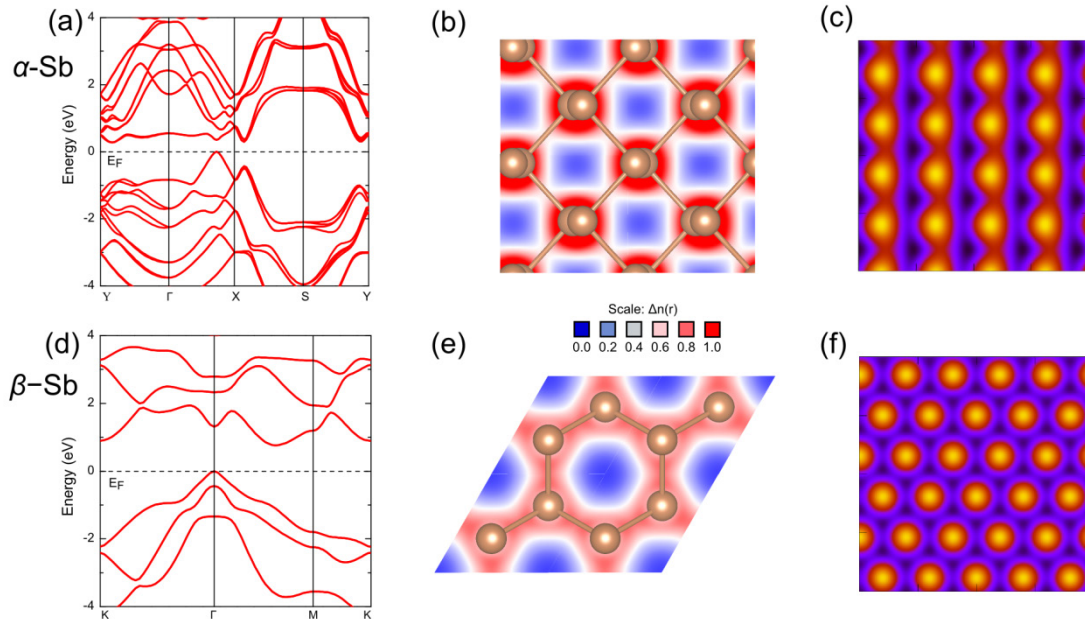
Figure 6.4 Electronic properties of α-Sb (a, b, and c) and β-Sb (d, e, and f) monolayers: (a and d) band structure, (b and e) charge density projected in the plane, and (c and f) simulated STM images. (Reprinted with permission from reference [237]. Copyright 2015 American Chemical Society.)

Considering that the Raman measurements are widely used to characterize 2D materials, such as graphene [240], we have calculated the Raman spectra for α- and β-Sb monolayers at the LDA-DFT level of theory which are shown in Figure 3. In order to assess the reliability of our approach, we first calculated the Raman spectrum of the bulk Sb. Two Raman peaks, E_g at ~100 cm^{-1} and A_{1g} at

~148 cm^{-1} are in agreement with experiments [241]. This gives confidence in our calculated results for the Raman spectra of antimonene.

α-Sb belongs to C$_{2v}$ group, and the modes, A$_1^1$ at 63 cm^{-1}, B$_1$ at 102 cm^{-1}, A$_1^2$ at 132 cm^{-1}, and A$_1^3$ at 147 cm^{-1}, exhibit prominent Raman scattering. A$_1^1$ and A$_1^3$ are out-of-plane modes. For the A$_1^1$ mode, atoms belonging to the same sub-layer vibrate along opposite directions. A$_1^3$ is the most dominating Raman peak for α-Sb for which atoms belonging to the same sub-layer vibrate along the same direction and the two sub-layers vibrate opposite each other. B$_1$ and A$_1^2$ are both in-plane modes in α-Sb. The β-Sb monolayer belongs to D$_{3d}$ group and the Raman active modes are at 150 cm^{-1} (E$_g$) and 195 cm^{-1} (A$_{1g}$). The E$_g$ modes are doubly degenerate in-plane modes with two atoms in the unit cell vibrating along opposite directions, and A$_{1g}$ is an out-of-plane vibrating mode.

The calculated band structure, charge density and STM images are shown in (Figure 6.4). The α-Sb monolayer has a relatively small indirect band gap of ~0.28 eV. The valence band maximum (VBM) has a hybrid character of s orbitals and in-plane p_x and p_y orbitals, which shows an almost linear dispersion at VBM. Due to the puckered structure, α-Sb has a stripe like STM surface characteristic (Figure 6.4(c)). The electronic band structure (Figure 6.4(d)) for the β-Sb monolayer shows it to be semiconducting with an indirect band gap of ~0.76 eV. A dot-like feature in the simulated STM image (Figure 6.4(f)) of the β-Sb monolayer results from its buckled surface.

Figure 6.5 shows atomic arrangements of antimonene multilayers. β-Sb multilayers prefer an ABC stacking similar to the bulk Sb (Figure 6.5(d)); the AA-stacked bilayer is higher in energy by ≈24 meV/atom than the AB-stacked bilayer. The calculated layer distance is found to be 3.65 Å. The band gap of the bilayer and trilayer β-Sb decreases significantly due to the small surface states splitting as predicted in the previous theoretical report on ultrathin β-Sb [232]. It is interesting to note

that the binding energy of β-Sb bilayer is 124 meV/atom, which is much larger than that of other vdW layered materials, such as graphite (≈20 meV/atom [242]) and MoS_2 (≈60 meV/atom [242]). This is due to the partially overlapping of lone pair orbitals from the neighboring layers as seen from the charge density plot (Figure 6.5(e)). This is also confirmed by the deformation change density shown in Figure 6.5(f). Therefore, the mechanical exfoliation of bulk Sb is not expected to be relatively easier than that of graphite or MoS_2.
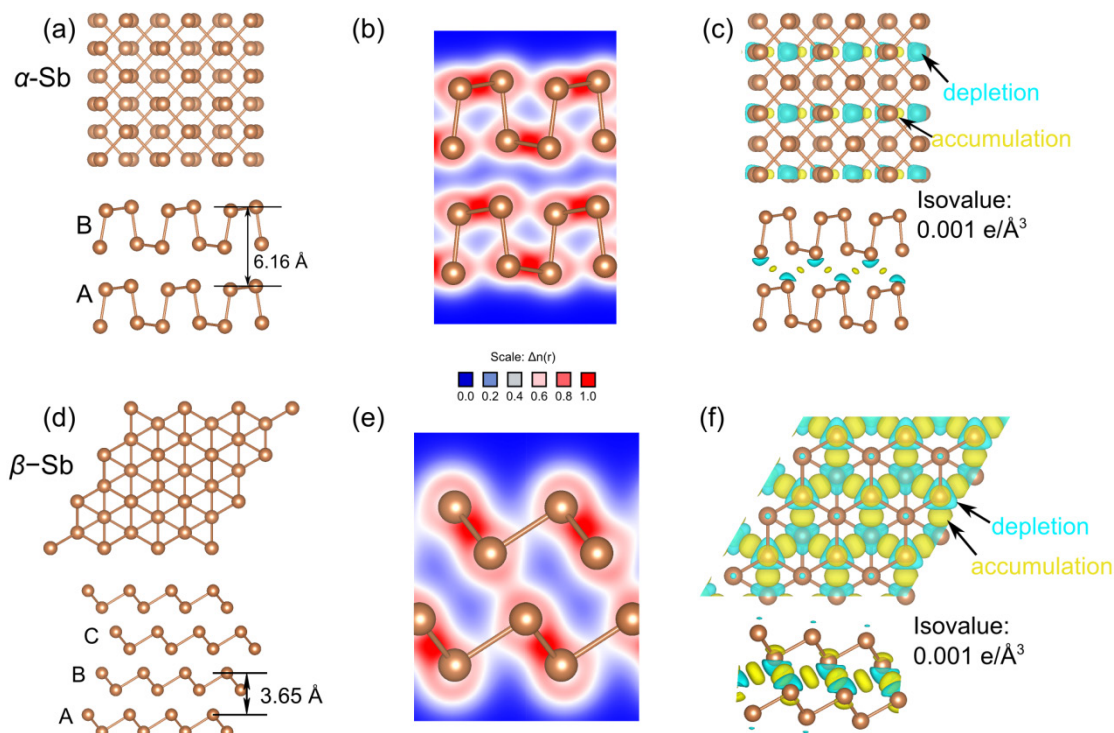
Figure 6.5 α-Sb and β-Sb multilayers: (a) atomic structure, (b) charge density projected perpendicular to the layers, (c) deformation charge density for α-Sb bilayer; (d) atomic structure, (e) charge density projected perpendicular to the layers, and (f) the deformation charge density for β-Sb bilayer. (Reprinted with permission from reference [237]. Copyright 2015 American Chemical Society.)

α-Sb multilayers prefer an AB stacking similar to that of black phosphorus (Figure 6.5(a)). The layer distance in α-Sb bilayer is calculated to be 6.16 Å. The binding energy of the AB-stacked α-

Sb bilayer is calculated to be 68 meV/atom, which is close to those of other layered materials, e.g. MoS$_2$ [242]. The charge density in the region between the bilayer is very small (Figure 6.5(b)), and the electron redistribution in α-Sb bilayer (Figure 6.5(c)) is not as obvious as that in β-Sb bilayer. All these features indicate that the interlayer interaction is dominated by vdW interaction in α-Sb multilayers. The AA-stacked bilayer is calculated to be 8 meV/atom higher in energy than the AB-stacked bilayer. The α-Sb bilayer and trilayer are calculated to be metallic with VBM and CBM crossing the Fermi level.

It is well known that strain can be introduced spontaneously by deposition of ultra-thin films on substrates with mismatched lattice constants. Application of strain to 2D atomic layers is also one of the possible approaches to tailor their electronic properties. Previous calculations on silicene, which has similar structure to β-Sb, have predicted it to sustain under the strain up to 20% [243, 244]. Likewise, α-P shows superior mechanical properties due to its puckered structure, sustaining under the strain up to 30% along the armchair direction [167]. Experimentally, a large strain up to 30% could be applied to 2D materials by the use of stretchable substrates [105].

The tensile strain is defined as $\varepsilon = (a-a_0)/a_0$, where a_0 and a are the lattice constants of the relaxed and strained structure, respectively. The stress-strain curve for antimonene allotropes is calculated following the procedure of Wei and Peng [167] are shown in Figure 6.6. The stress is rescaled by the factor Z/d to get the equivalent stress, where Z is the cell length along z direction and d is the interlayer spacing. d is calculated to be 3.65 and 6.16 Å for β-Sb and α-Sb, respectively. It should be noted that the inter layer distance predicted for β-P and α-P are 4.20 and 5.30 Å, respectively [224].

For α-Sb, the ideal strengths, which are defined as the maximum stress in the stress-strain curve, are ~10 GPa and ~4 GPa along the zigzag and armchair directions (Figure 6.6(a)). The corresponding critical strains are 18% and 32%, respectively. For β-Sb, the ideal strengths are ~10 and ~11 GPa along zigzag and armchair directions, respectively (Figure 6.6(b)). The corresponding critical strains are 15% (zigzag direction) and 18% (armchair direction). Both the ideal strength and critical strain are quite close along the zigzag and armchair directions. This clearly shows that β-Sb has nearly isotropic mechanical properties while α-Sb exhibits strongly anisotropic mechanical characteristics. The critical strain along the armchair direction is extremely large in α-Sb, which will lead to strain engineering of its electronic properties.
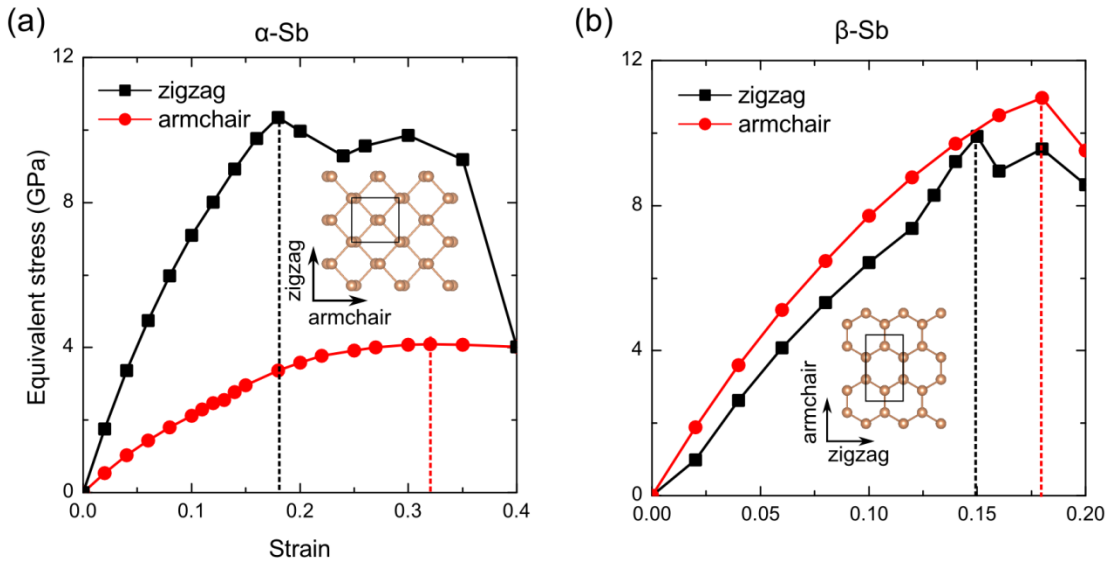
Figure 6.6 Stress-strain relationship for antimonene monolayers: (a) α-Sb and (b) β-Sb. (Reprinted with permission from reference [237]. *Copyright 2015 American Chemical Society.)*

Next, we examine the tensile strain effect on the electronic properties of both Sb monolayers within the critical strain region. α-Sb has an indirect band gap and the tensile strain along the armchair direction induces an indirect-direct band gap transition (Figure 6.7(a)). With strain larger than 6%,

a direct band gap at *V1* is predicted. For 11% strain, the band gap at *V1* decreases to 0.05 eV.

Thereafter, the band gap gradually increases with strain larger than 11%, and reaches to 0.45 eV at

20% strain. For the tensile strain along zigzag direction (Figure 6.7(b)), CBM moves to *V2* point,

and VBM moving to *Γ* for 8% of strain. The strain induced indirect-direct band transition is mainly

due to competition of states at *Γ*, *V1* and *V2*. Similar theoretical results have also been reported for

α-P [16] and *α*-As layers [225].
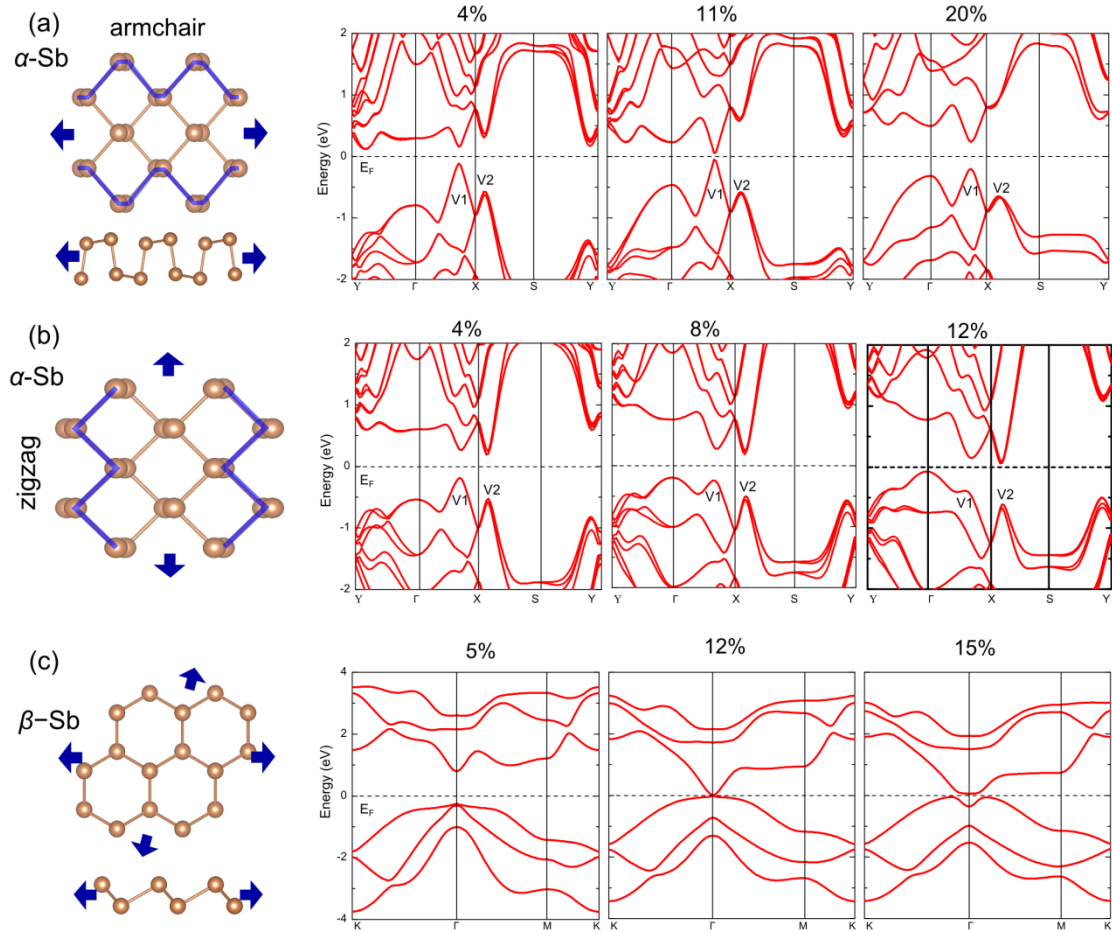
Figure 6.7 Electronic band structures of α-Sb and β-Sb monolayers under various strains: (a) α-Sb under strain along armchair direction, (b) α-Sb under strain along zigzag direction, and (c) β-Sb under biaxial strain. (Reprinted with permission from reference [237]. Copyright 2015 American Chemical Society.)

Since *β*-Sb monolayer shows isotropic mechanical properties along the zigzag and armchair directions, a biaxial tensile strain was applied to the lattice as shown in Figure 6.7(c). *β*-Sb monolayer has (minimum) indirect band gap of 0.76 eV at the equilibrium configuration. Under 5% of strain, its band gap becomes direct at *Γ*. The band gap closes under 12% of strain, and reopens for strain of 20%. Considering that *β*-Sb monolayer still preserves its buckled structure under 15% of strain, its band gap can be effectively tuned by the in-plane strain.

Figure 6.8 Structural and electronic properties of antimonene monolayers on graphene substrates: (a) and (b) β-Sb on graphene; (b) and (d) α-Sb on graphene. (Reprinted with permission from reference [237]. Copyright 2015 American Chemical Society.)

Considering that the mechanical exfoliation (scotch tape) approach will be difficult to fabricate antimonene due to much larger predicte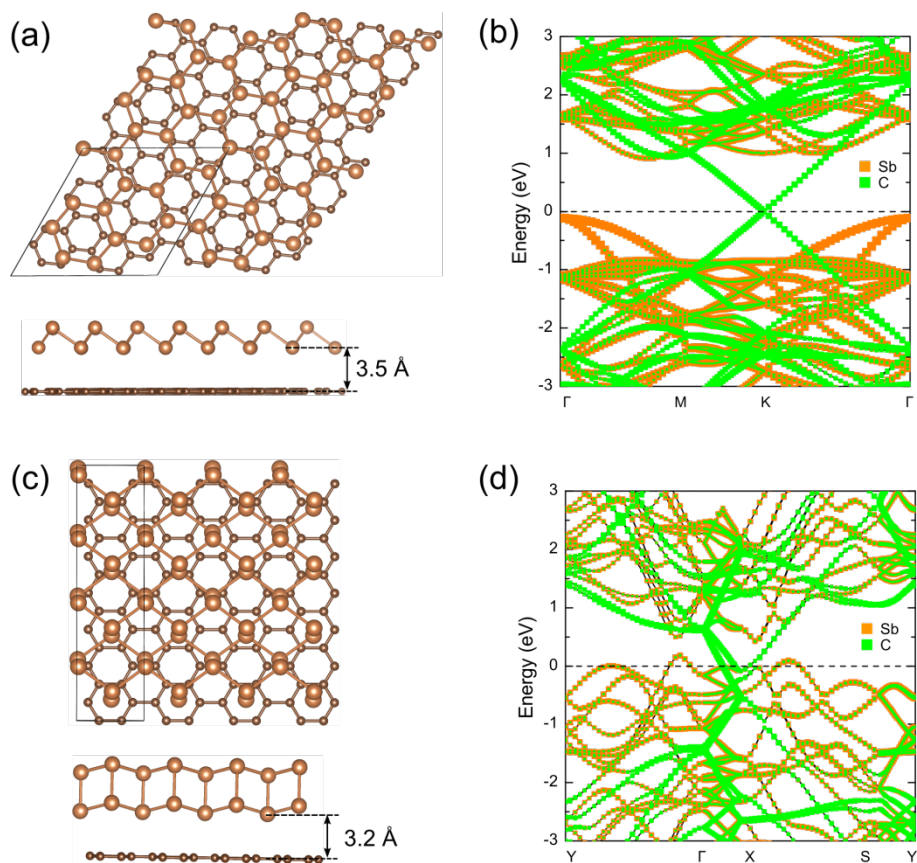d binding energy of the bilayers, the standard chemical techniques are likely to play a major role in the synthesis of 2D antimonene system. For example, the ultrathin Bi(111) and Bi(110) films have been assembled on Si or highly ordered pyrolytic graphite (HOPG) substrate by vapor deposition [245, 246]. In our work, we have considered a graphene substrate for the fabrication of Sb monolayers. α-Sb/graphene is simulated with a rectangular supercell of 4.5 Å×17.1 Å, and β-Sb/graphene is simulated with a parallelogram supercell of 10.6 Å×10.6 Å as shown in Figure 6.8. The large supercells are chosen to reduce the lattice mismatch between graphene and antimonene to 5%.

As seen from the relaxed structures, the distance between the antimonene and the graphene substrate is larger than 3.2 Å at LDA-DFT level of theory. The corresponding binding energies of α- and β-Sb on graphene substrate are 16 meV/atom and 14 meV/atom, respectively. The Sb-Sb bond lengths are 2.82 Å and 2.86 Å in α-Sb/graphene, and 2.83 Å in β-Sb/graphene, which are close to the bond lengths in antimonene monolayer without a substrate. From the projected band structures (see Figure 6.8), the electronic property of β-Sb monolayer is maintained on graphene substrate; and slightly charge transfer from α-Sb to graphene is observed as indicated by the shifting of the Fermi level (see Figure 6.8). Therefore, graphene could possibly serve as a substrate for the epitaxial growth of antimonene allotropes.

6.4. Summary

In conclusion, DFT calculations were performed on 2D antimonene atomic layers. Our results show that α- and β-Sb monolayers to be stable and can be realized experimentally. Both monolayers are semiconductors with indirect band gap. β-Sb has nearly isotropic mechanical properties whereas α-

Sb exhibits strongly anisotropic mechanical characteristics. Moderate tensile strain would induce indirect to direct band gap transition in antimonene. The calculated Raman spectrum prominently shows in-plane and out of plane vibrating modes that can be used to characterize experimentally synthesized antimonene monolayers.

Chapter 7   Group IV-V binary 2D materials– carbon phosphide[*]

7.1.   Introduction

Since the discovery of graphene [58, 247], two dimensional (2D) materials have sparked an extraordinary level of interest due to their unique properties and novel applications in electronics and optoelectronics. Among the 2D material family, the group IV elemental monolayers, graphene, silicene and germanene stand out due to presence of the Dirac cones [63, 248], which endow the massless Dirac fermions with extremely high carrier mobility. However, the gapless nature of group IV monolayers is one of the major obstacles for their applications in transistors. Recently, the group V elemental monolayers such as phosphorene [11, 175], arsenene [225, 226] and antimonene [237, 249] were established as promising 2D materials with electronic properties which are significantly different from those of the group IV elemental monolayers. For example, phosphorene is a direct band gap semiconductor with anisotropic electronic conductance and high hole mobility [19, 175]. However, due to the fast degradation of phosphorene in air, its application in electronic devices has been challenging [161, 177, 178].

Interestingly, the group IV and V elemental monolayers show noticeable structural similarities including three-fold coordinated atoms and a hexagonal network. In graphene, each C atom is sp^2 hybridized connecting to three neighboring C atoms in a planar hexagonal structure through σ bonds. The out-of-plane p_z orbitals form π and π^* bands leading to its band structure with Dirac cones [63].   In phosphorene, P atom is sp^3 hybridized sharing three of its valence electrons with

---

neighboring P atoms forming a puckered hexagonal lattice. The remaining two valence electrons form a lone pair in one of the sp^3 orbitals. Since preference of C and P atoms appears to be three-fold coordination in the 2D monolayer, the following intriguing questions arise: Is it possible to form a stable carbon phosphide (CP) monolayer? If yes, then how will the binary monolayer be like in terms of mechanical and electronic properties including nature of the band gap and carrier mobility?

It is to be noted that experimental efforts are being made to produce carbon phosphide (or phosphorus carbide). Initial attempts to synthesize bulk CP were made by producing P-doped diamond-like carbon [250]. Later, synthesis of amorphous CP films using radio frequency plasma deposition with CH_4 and PH_3 gas mixtures was reported [251, 252]. The ratio of P/C in their samples can be widely controlled via the ratio of PH_3/PH_4 gas [251, 252], which led to the efforts of producing CP films using pulsed laser deposition [253, 254] and magnetron sputtering techniques [255]. In these experiments, the presence of direct C-P bonds was established. Theoretically, the properties of bulk phases of crystalline carbon phosphide with a range of stoichiometric compositions were investigated via density functional theory [253, 256]. Various phases with three- and four-fold coordinated P atoms have been predicted [256].

To the best of our knowledge, no experimental or theoretical study has been made on CP monolayer. In this paper, we consider structure, stability, mechanical and electronic properties of the low-energy phases of CP monolayer obtained by an exhaustive structural search performed using a recently developed CALYPSO code with particle swarm optimization method [51].

7.2. Computational methods

The CP monolayers with different stoichiometric compositions are obtained with CALYPSO code [51]. The number of structures (e.g., population) that produced at each step is set to 24, and the number of CALYPSO steps (e.g., generation) is fixed to 20. The number of atoms in the unit cells is up to 10. The stoichiometric monolayers with composition ratio of C_1P_1 have attracted our particular attentions due to their compact structural configurations. We classify these hexagonal configurations to be α-, β-, and γ-phases of CP monolayer (Figure 7.1) in analogy to the classification used for phosphorene, α-P (black) and β-P (blue) monolayers [208]. The α-P has a puckered surface due to the intralayer sp^3 bonding character in the lattice. β-P possesses a buckled hexagonal honeycomb structure maintaining the sp^3 character of bonds. Note that the cohesive energies of these structures are 60-90 meV/atom lower than the average cohesive energy of α-P and graphene, which implies these structures are metastable compared to α-P and graphene. However, this does not necessarily mean that CP monolayers cannot be synthesized in experiments. For examples, the layered $As_{1-x}P_x$ compounds, which are predicted to be metastable compared to layered As and layered P compounds [141], have been synthesized [257]. Moreover, the stability of these monolayers is verified by the vibration spectra calculations and *ab initio* molecular dynamics (AIMD) simulations in the present study.

Calculations of electronic properties were performed using the projector-augmented-wave (PAW) method and the generalized-gradient approximation (GGA-PBE) for electron exchange-correlation interaction [137] as implemented in the Vienna *Ab initio* Simulation Package (VASP) [258]. The electronic and mechanical properties were obtained with GGA-PBE functional throughout this paper. Since GGA usually underestimates the band gap, we also used the hybrid Heyd-Scuseria-

Ernzerhof (HSE06) functional form [29] to get relatively accurate values of the band gap. The energy convergence was set to 10^{-6} eV and the residual force on each atom was smaller than 0.01 eV/Å. The energy cutoff for the plane-wave basis was set to 500 eV. The reciprocal space was sampled by *k*-point meshes of (11×11×1) for geometry optimization, and (45×45×1) for density of states (DOS) calculations. The vacuum distance normal to the plane was larger than 20 Å to eliminate interaction between the replicas due to the periodic boundary conditions in the supercell approach of our model. The vibration spectra calculations were performed by means of finite displacement method as implemented in the PHONOPY program [40] with supercell size of (3×4×1), (8×5×1), and (4×5×1) for α-, β-, and γ-CP, respectively. The AIMD simulations were based on the NVT ensemble with a time step of 1 *fs*. The temperature was controlled to 300 K with Nośe-Hoover thermostat [210]. In this work, the van der Waals (vdW) term was also included as in the DFT-D2 method of Grimme [209] to check the structure, stability and electronic properties of α-, β-, and γ-CP. Consistent results were obtained with GGA-PBE and DFT-D2 functional forms.
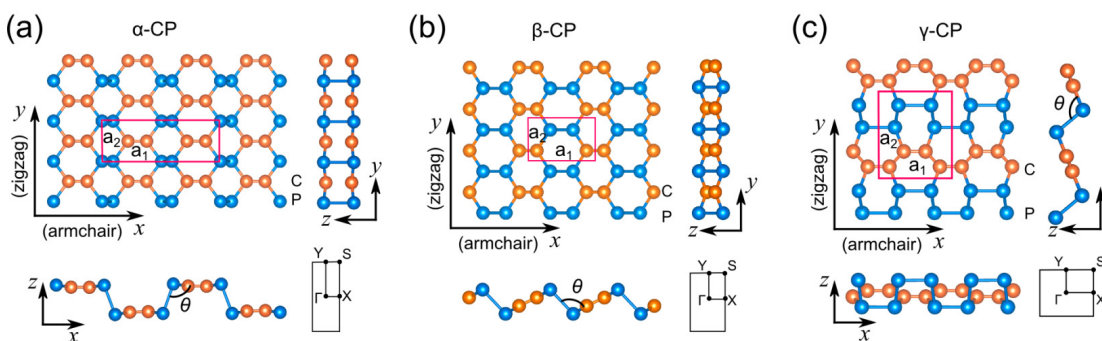
7.3. Results and discussions

Figure 7.1 The structural geometry including top view, side view, and the Brillouin zone of (a) α-CP, (b) β-CP, and (c) γ-CP. a_1 and a_2 are the lattice constants, R is the nearest neighbor distance, θ is the bond angle of C-P-P. (Reprinted with permission from reference [259]. Copyright 2016 Royal Society of Chemistry.)

In α-, β-, and γ-CP, each C atom bonds with three nearest neighbors in a planar configuration (see the side views in Figure 7.1) implying the C atoms are sp^2 hybridized. On the other hand, each P atom bonds with three neighboring atoms in a buckled configuration suggesting sp^3 hybridization of P atoms in the 2D lattice. For α- and β-CP, the zigzag (i.e. y) direction is composed of alternating C and P atoms, and the armchair (i.e. x) direction is composed of alternating C-C and P-P dimers. Overall, α-CP has a puckered surface, and β-CP has a buckled surface as seen from the side views in Figures 7.1(a) and 1(b). The γ-CP is composed of alternating P chain and C chain along the armchair direction (Figure 7.1(c)). Due to mismatch in C-C and P-P bonds, the γ-CP has a distorted hexagonal network.

Table 7.1. Calculated structural parameters of CP monolayers (see Figure 1) at the GGA-PBE level of theory. (Reprinted with permission from reference [259]. Copyright 2016 Royal Society of Chemistry.)

	a_1 (Å)	a_2 (Å)	R_{C-C} (Å)	R_{C-P} (Å)	R_{P-P} (Å)	θ (°)	*Cohesive energy (eV/atom)*
α-CP	8.68	2.92	1.36	1.83	2.32	97.40	5.32
β-CP	4.72	2.91	1.37	1.82	2.33	97.78	5.33
γ-CP	4.80	5.63	1.45, 1.43	1.82	2.30, 2.17	104.00	5.35

All three phases of CP monolayer have nearly degenerate cohesive energy with the rectangular unit cells as summarized in Table 7.1. The length of C-C, C-P, P-P bonds in α- and β-CP are 1.36-1.37 Å, 1.82-1.83 Å, and 2.32-2.22 Å, respectively. The C-C bond in CP monolayer is slightly shorter than that of 1.42 Å in graphene [63], and the P-P bond is slightly longer than that of 2.26 (2.22) Å in

phosphorene calculated at the same level of theory [175]. In γ-CP, the length of C-C and P-P bonds vary in the range 1.43-1.45 Å and 2.17-2.30 Å, respectively which are very close to those of graphene and phosphorene. Typical C-P bond lengths of 1.85 Å were reported in the bulk CP by the GGA-PBE calculations [256].

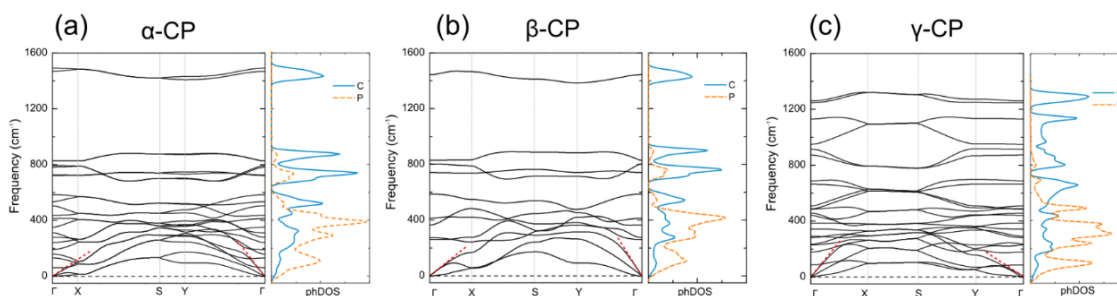*Figure 7.2 The phonon dispersion and phonon density of states (phDOS) calculated for (a) α-CP, (b) β-CP, and (c) γ-CP. (Reprinted with permission from reference [259]. Copyright 2016 Royal Society of Chemistry.)*

The phonon dispersion curves are displayed in Figure 7.2 showing no imaginary (negative) vibration mode in the Brillouin zone. AIMD simulations show that α-, β-, and γ-CP maintain their structural integrity up to 5 *ps* demonstrating the dynamical stability of α-, β-, and γ-CP. It is to be noticed that the slopes of the longitudinal acoustic (LA) branch along Γ-X is significantly different from those along Γ-Y near Γ. The speed of sound derived from the LA branch along Γ-X (armchair) and Γ-Y (zigzag) directions are found to be (5.9, 12.0 km/s), (6.3, 12.3 km/s), and (13.3, 6.8 km/s) for α-, β-, and γ-CP, respectively, reflecting the anisotropic nature of the in-plane stiffness in the hexagonal network. The maximum vibrational frequency at 1450 cm^{-1} for the optical branches of α-, and β-CP is associated with C atoms as seen in the phonon density of states affirming a high strength of C-C bonds in the hexagonal network. Additional calculations based on the strain energy curves [111, 260] reveal the in-plane stiffness along the armchair and zigzag directions to be (18.8, 171.5 N/m), (46.6, 158.3 N/m), and (233.2, 51.9 N/m) for α-, β-, and γ-CP, respectively confirming

the anisotropy nature of the mechanical properties. The lower stiffness along the armchair direction is due to the puckered or buckled nature of α- and β-CP lattice (Figures 7.1(a) and (b)) which could accommodate external strains by changing the puckered or buckled angle without much distortion of the bond length. This is similar to the anisotropic mechanical properties observed for phosphorene [172, 261]. For the γ-CP, the stiffness along the armchair direction is large because of the C chains. The in-plane stiffness of CP monolayers is smaller than that of 340 N/m in graphene [111, 125], while it is larger than that of 28.9 N/m and 101.6 N/m in phosphorene [19] (except for the α-CP along the armchair direction) due to the existence of stronger C-C and C-P bonds with sp^2 hybridization in the hexagonal lattice.

The electronic properties of α-CP monolayer are presented in Figure 7.3. The calculated band structure and density of states (DOS) indicate α-CP monolayer to be a semiconductor with an indirect band gap of 0.63 eV at the GGA-PBE level of theory. The valence band maximum (VBM) is at Γ with a value of -4.05 eV. The conduction band minimum (CBM) is located at Y with a value of -3.42 eV. The direct energy gap at Γ is 40 meV larger than the indirect gap from Γ to S. The C-p_z and P-p_z orbitals dominate the VBM and the CBM.

The band structure and DOS indicate β-CP monolayer to be a semiconductor with a band gap of 0.39 eV (Figure 7.4(a)). CBM is at X point with a value of -3.76 eV, and VBM at -4.15 eV lies very close to X point. Since the energy of the first VB at X point is only 10 meV lower than VBM, we may identify the gap to be a quasi-direct band gap for β-CP monolayer. The C-p_z and P-p_z orbitals dominate VBM, and C-p_z and P-p_x orbitals mainly contribute to CBM. Bader charge analyses reveal a similar charge transfer of 0.92e and 0.99e from P atom to C atom in α- and β-CP, respectively.
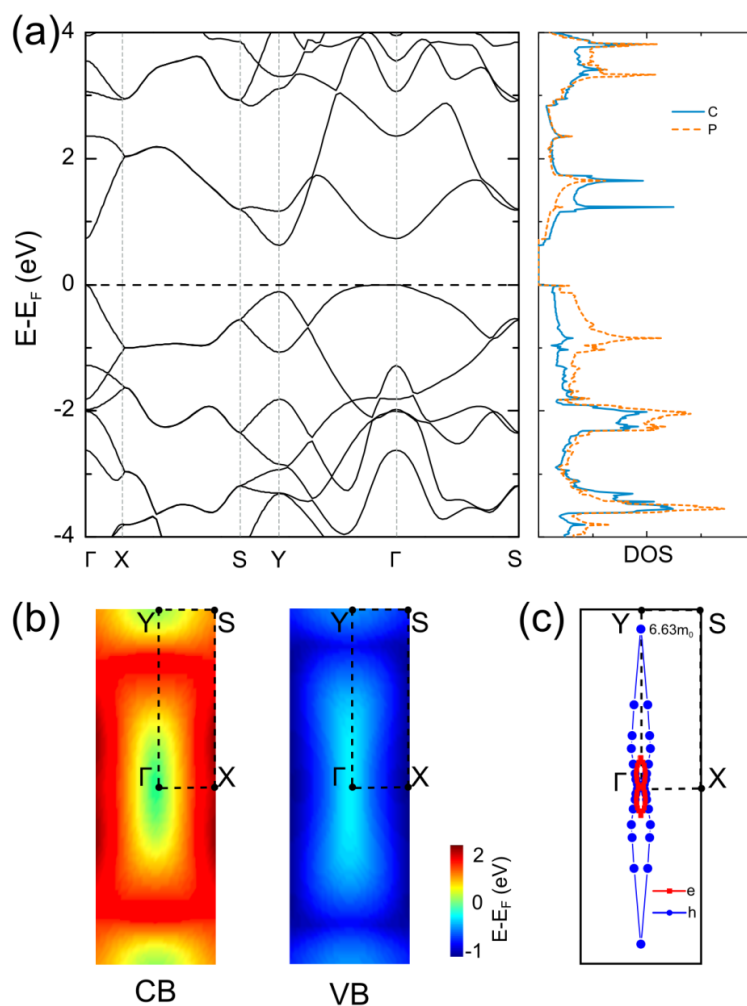
Figure 7.3 Electronic properties of α-CP: (a) band structure and density of states, the inset is the zoomed figure around V point, (b) 2D energy profiles of the first valence band (VB) and the first conduction band (CB), and (c) effective mass of electrons and holes at Γ along different directions; distance from a data point to Γ is proportional to the magnitude of the effective mass. The solid line acts as a guide to the eye. (Reprinted with permission from reference [259]. Copyright 2016 Royal Society of Chemistry.)

α- and β-CP monolayers are found to show high anisotropy in their electronic properties. For example, valence and conduction bands around Fermi level have different slopes along the X-Γ (armchair) and X-S (zigzag) directions (Figure 7.4(a)), which reflects directional dependence of effective mass of electrons and holes in β-CP. From the 2D plots of the energy dispersion of the

first valence and conduction bands shown in Figure 7.4(b), we see elongated shape along X-S. In contrast, the bands encounter a higher degree of dispersion along X-Γ reflecting a smaller effective mass of carriers.
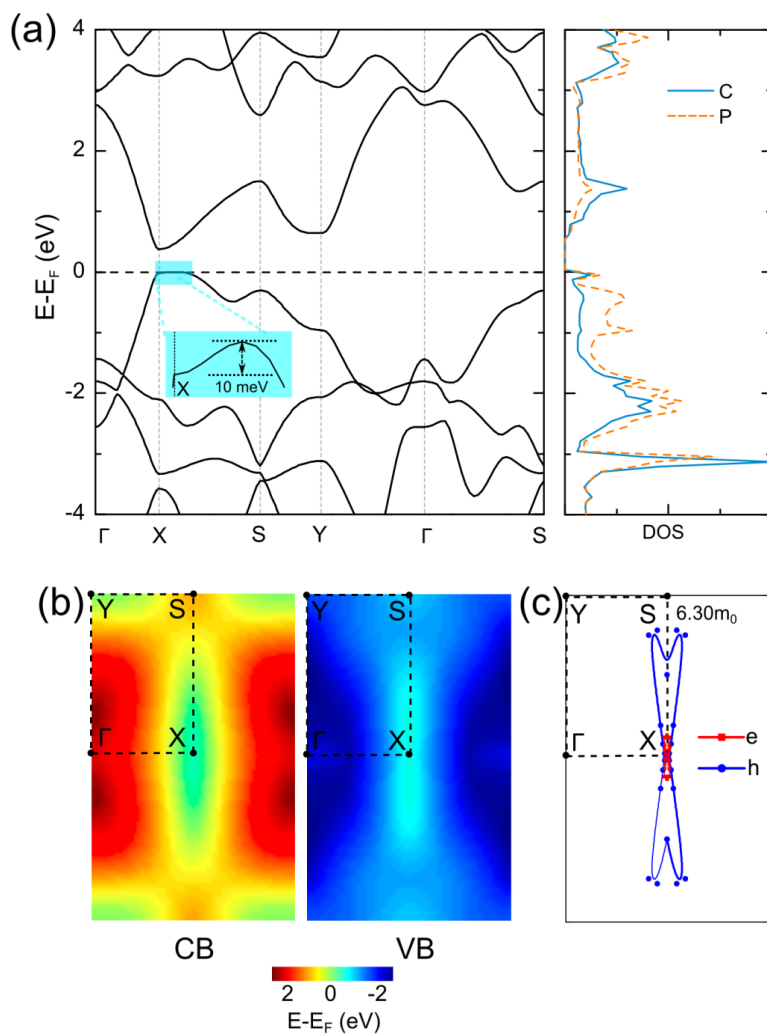

Figure 7.4 Electronic properties of β-CP monolayer: (a) band structure and density of states, (b) 2D energy dispersion of the first valence band (VB) and the first conduction band (CB), and (c) effective mass of electrons and holes along different directions at X; distance from a data point to X is proportional to the magnitude of the effective mass. The solid line acts as a guide to the eye. (Reprinted with permission from reference [259]. Copyright 2016 Royal Society of Chemistry.)

The calculated directional dependence of effective mass of the carriers is shown in Figure 7.4(c). The values are significantly larger in the X-S (zigzag) direction than the X-Γ (armchair) direction. Along the X-Γ (armchair) direction, electrons and holes have effective masses smaller than $0.05m_0$. The values along X-S (zigzag) direction are $1.10m_0$ and $4.10m_0$, respectively. The effective mass of holes could reach a maximum of $6.30m_0$ nearby the X-S direction. α-CP also has significant anisotropic effective mass as demonstrated in Figures 7.2(a), (b) and (c).

The effective masses of carries in α- and β-CP along the zigzag (y) direction are comparable to the values in phosphorene ($1.12m_0$ and $6.35m_0$ [16, 17, 19]), while the values along the armchair (x) direction are even smaller than those in phosphorene ($0.17m_0$ and $0.15m_0$ [16, 19]). The heavier holes along the zigzag direction are mostly contributed by the P-p_z orbital, and the lighter holes along the armchair direction Sare mainly associated with C-p_z and P-p_z orbitals. Therefore, contributions of C-p_z electrons appear to decrease the effective mass of carriers in the binary carbon phosphide monolayer which are extremely important for nanoscale devices requiring semiconducting materials with high carrier mobility.

An understanding of the electronic conductance of the material can be gained from the carrier mobility calculations based on the deformation potentials (DP) theory as proposed by Bardeen and Shockley [262]. According to the DP theory, the carrier mobility of 2D materials can be evaluated according to the following expression [16, 17, 19, 263]

$$\mu_x = \frac{e\hbar^3 C_x}{(2\pi)^3 k_B T m_x^* m_d (E_{1x}^2)}, \tag{7.1}$$

where e is the electron charge, h is the Planck's constant, T is the temperature and m^* is the effective mass. m_d is determined by $m_d = (m_x^* m_y^*)^{1/2}$. E_{1x} is the deformation potential defined as $E_{1x} =$

109

$\Delta V/(\Delta a_x/a_x)$, and is obtained by varying the lattice constant a_x along the direction of electron conduction. ΔV is the change of the band energy. The in-plane stiffness constant C_x is obtained by evaluating the strain energy curve [111, 260]. Equation 7.1 has been demonstrated previously to give a reliable estimate for the upper limit of the carrier mobility in phosphorene [17, 19].

Table 7.2. Calculated carrier mobility in α-CP monolayer at T = 300 K along x (armchair) and y (zigzag) direction obtained at GGA-PBE level of theory. m_e^* and m_h^* are the effective masses of electron (e) and hole (h), respectively. (Reprinted with permission from reference [259]. Copyright 2016 Royal Society of Chemistry.)

	m_e^*/m_0	m_e^*/m_0	E_{1x}	E_{1y}	C_x	C_y	μ_x	μ_y
	x	y	(eV)		(Nm^{-1})		(10^3 cm^{2}V^{-1}s^{-1})	
e	0.10	1.22	1.72	10.55	18.75	171.47	3.87	0.08
h	0.12	6.63	0.18	1.75	18.75	171.47	115.18	0.20

The calculated carrier mobility using Equation 7.1 at room temperature ($T = 300$K) for α- and β-CP is summarized in Tables 7.2 and 7.3, respectively. The carrier mobility shows strongly directional dependence as one would expect from the anisotropic nature of the calculated effective masses for α- and β-CP. The electron and hole mobility along the armchair direction is significantly larger than those obtained along the zigzag direction suggesting the presence of an anisotropic conductance in α- and β-CP. Such strong anisotropy in carrier mobility can be measured in experiments [175] and may facilitate fabrication of the anisotropic electronic devices. More interesting than the anisotropic electronic conductance is the large value of the carrier mobility in CP monolayers. For example, the hole mobility at room temperature in α-CP could potentially reach 1.15×10^5 cm^{2}V^{-1}s^{-1}, which is approximately five times larger than the maximum value in

phosphorene (0.26×10^5 cm^{2}V^{-1}s^{-1} [35]), and significantly larger than other 2D materials, such as MoS$_2$ [14]. Such a large hole mobility in α-CP is attributed to a small effective mass together with a small deformation potential along the armchair direction (Table 7.2). β-CP has comparable hole mobility to phosphorene, while the electron mobility is much larger that in phosphorene [35].

Table 7.3. Calculated carrier mobility in β-CP monolayer at T = 300 K along x (armchair) and y (zigzag) direction obtained at GGA-PBE level of theory. m_e^* and m_h^* are the effective masses of electrons (e) and holes (h), respectively. (Reprinted with permission from reference [259]. Copyright 2016 Royal Society of Chemistry.)

	m_e^*/m_0	m_e^*/m_0	E_{1x}	E_{1y}	C_x	C_y	μ_x	μ_y
	x	y	(eV)		(Nm^{-1})		(10^3 cm^{2}V^{-1}s^{-1})	
e	0.05	1.10	2.56	9.30	46.56	158.27	12.91	0.15
h	0.05	4.10	1.68	1.66	46.56	158.27	15.52	0.66

Distinct from α- and β-CP, γ-CP is found to be a semimetal as shown in Figure 7.5. From the band structure in Figure 7.5(a), the VB and CB cross at V point on the Γ-X. The 2D and 3D energy dispersion plots in Figures 7.5(b) and (c) illustrate that VB and CB touch at V and V' in the Brillouin zone forming distorted Dirac cones. An average of 0.46e is transferred from P atom to C atom from Bader charge analysis. Calculations with a step size of 0.0013 1/Å along Γ-X were performed to calculate Fermi velocity ($v_k = \left(\frac{1}{\hbar}\right)\left(\frac{\partial E_k}{\partial k}\right)|_{E_k=E_F}$). The calculated v_F values for of electrons and holes along the V-X direction are 0.78×10^6 m/s and 0.40×10^6 m/s, respectively. The Fermi velocity of electrons is close to the value in graphene ($v_F = 0.85\times10^6$ m/s [112]) implying the high electron mobility in γ-CP.
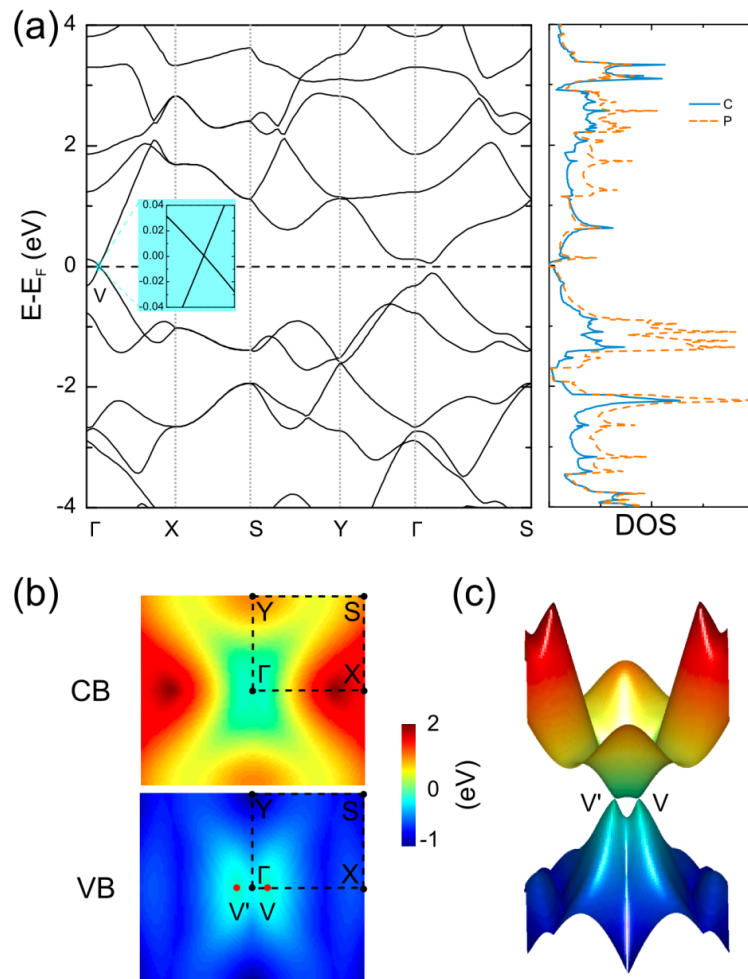
Figure 7.5 Electronic properties of γ-CP monolayer: (a) band structure and density of states, (b) 2D energy dispersion of the first CB and first VB, and (c) 3D plot for first VB and first CB. V and V' are the Dirac points in the Brillouin zone. (Reprinted with permission from reference [259]. Copyright 2016 Royal Society of Chemistry.)

The band structures of α-, β-, and γ-CP based on the hybrid HSE06 functional reveal a relatively large band gap of 1.26 eV (0.87 eV) for α-CP (β-CP). Note that the hybrid HSE06 functional finds nearly the same shape of the band structure which is obtained by the GGA-PBE functional form. The semi-metallic property of γ-CP is also verified with HSE06 functional form. Therefore, γ-CP is like graphyne showing Dirac Fermions in a rectangular lattice [98, 111].

112

The most appealing properties which make carbon phosphide monolayers intriguing members of the 2D material family are the anisotropic nature of electronic conductance and high carrier mobility. α- and β-CP monolayers are predicted to have strongly anisotropic electronic properties together with the smallest effective mass of carriers ($\approx 0.10 m_0$, and $0.05 m_0$, respectively) among the known 2D semiconductors such as phosphorene ($0.15 m_0$) [16, 19] and MoS$_2$ ($0.45 m_0$) [264].

α-, β-, and γ-CP monolayers cannot be fabricated with the mechanical exfoliation methods due to the absence of layered bulk counterparts. The possible synthesis approach can be chemical vapor deposition (CVD) which has been successfully used to synthesize 2D materials including group IV monolayers, such as graphene [65, 66] and silicene [72-74], and group V thin films, such as Bi(111) and Bi(110) [245, 246]. We also notice recent progress in the fabrication of carbon phosphide thin films including strong evidence of the formation of C-P bonded regions in samples prepared with the pulsed laser deposition method has been found [254]; The black phosphorus-graphite composites with sp^2 hybridized P-C bonds using mechanical milling process have also been reported [265]. The present work will further inspire the experimental realization of CP monolayers.

7.4. Summary

In summary, structure, stability and electronic properties of CP monolayers, namely α-, β-, and γ-CP, have been predicted. The structural configurations are comprised of sp^2 hybridized C and sp^3 hybridized P atoms in hexagonal networks. α- and β-CP are semiconductors with high anisotropy in electronic and mechanical properties. A large carrier mobility is predicted due to the small effective mass of the carriers. γ-CP is semi-metallic with Dirac cones. Our results suggest the yet unexplored binary carbon phosphide monolayers to hold great promises for applications in high-performance electronics and optoelectronics at nanoscale.

Chapter 8   Summary and future perspectives

8.1. Summary

In this thesis, the electronic properties of group IV and group V related 2D materials are investigated using *first-principles* calculations based on density functional theory. We started with one of the group IV elemental monolayer, graphyne. Its electronic properties and strain effects on its properties were investigated. It is shown that graphyne is semi-metallic with a Dirac cone like band structure in the freestanding form. External strain can be used to tune the Dirac cones. However, opening the band gap is not feasible in group IV elemental monolayers, thus greatly hinders their applications in electronics such as transistors.

Next, we moved to the group V elemental monolayers which have a fundamental band gap. Engineering of electronic properties of phosphorene by strain and external defects such as adatoms were investigated. It is found that adsorption of B, C, N, O and F adatoms can modify the electronic properties of phosphorene by inducing various mid-gap states, which are related to the interplay between electronegativity values and electronic structure of phosphorene. Under compressive strain, buckling will form without breaking the chemical bonds in the crystal. The structure flexibility enables the formation of nano-scrolls like structures in phosphorene. Additionally, we found phosphorene can easily get oxidized in air, and we proposed the possible formation of phosphorene oxide with different level of oxidation. The oxidized phosphorene species could chemically react with water molecules in the air ultimately leading to the degradation of phosphorene.

Then, the other group V elemental monolayer, antimonene, was systematically studied. The stability of a few allotropes of antimonene was examined. Their electronic properties including the

band structure, charge density, STM images and Raman spectra were simulated to help the experimentalists to characterize this material. It is interesting to note that the proposed antimonene structure has recently been realized in experiments.

Finally, the stable structures of binary group IV-V monolayers, carbon phosphide, were proposed. These monolayers can be semiconducting or semi-metallic depending on the arrangements of the atoms in the lattice. The predicted semiconducting phases have very high carrier mobility and high anisotropic electronic properties, suggesting their potential applications in future electronic devices.

8.2. Future perspectives

In this work, *first-principles* calculations were performed to study group IV and group V related 2D materials. There are a few unsolved questions that are worthy of future investigations:

i) Going beyond GGA functional. The calculations in this thesis are mostly at the LDA/GGA level of theory. It is well-known that LDA/GGA underestimates the band gap of semiconducting materials. It would be interesting to check the band structures of these 2D materials with a higher level of theory such as GW calculations, explore the optical properties of these materials at a higher level of theory, and compare with existing experiments.

ii) Binary group IV-V monolayers. In the current thesis, we only studied the carbon phosphide monolayers as an example of the binary group IV-V monolayers. It would be interesting to extend to other possible combinations of the IV-V compounds with different chemical compositions.

iii)   Devices with 2D materials. The ultimate goal of material research is to fabricate devices for various applications. Hundreds of 2D materials have been discovered, making it possible to design devices with these materials at will. It would be interesting to design and optimize the performance of devices built on these 2D materials using computational methods. For example, we can construct transistors using the semiconducting 2D materials in this thesis, and simulate their performance as channel materials.

iv)   Stability and electronic properties of group V elemental monolayers. In this work, we have learned that phosphorene is not chemically stable in air. However, the chemical stability of the other group V elemental monolayers, such as arsenene and antimonene have not been systematically studied. Considering the increasing scientific interests on these materials, it is urgent to investigate their chemical stability and their interactions with gas molecules.

v)   Some of these 2D materials have been fabricated in experiments, such as phosphorene and antimonene; while some of them have not been fabricated yet, such as graphyne and carbon phosphide. Efforts to synthesize these materials would not only be invaluable to confirm the theoretical predictions, but also lead to novel materials for future applications.

Bibliography

1.	Peierls, R. In *Quelques propriétés typiques des corps solides*, Annales de l'institut Henri Poincaré, 1935; pp 177-222.
2.	Landau, L. *Phys. Z. Sowjetunion* **1937,** 11, 26-35.
3.	Mermin, N. D. *Physical Review* **1968,** 176, (1), 250.
4.	Novoselov, K. S.; Geim, A. K.; Morozov, S.; Jiang, D.; Zhang, Y.; Dubonos, S.; Grigorieva, I.; Firsov, A. *Science* **2004,** 306, (5696), 666-669.
5.	Geim, A. K.; Grigorieva, I. V. *Nature* **2013,** 499, (7459), 419-425.
6.	Van Noorden, R. *Nature* **2006,** 442, (7100), 228-229.
7.	Dávila, M.; Xian, L.; Cahangirov, S.; Rubio, A.; Le Lay, G. *New Journal of Physics* **2014,** 16, (9), 095002.
8.	Butler, S. Z.; Hollen, S. M.; Cao, L.; Cui, Y.; Gupta, J. A.; Gutiérrez, H. R.; Heinz, T. F.; Hong, S. S.; Huang, J.; Ismach, A. F.; Johnston-Halperin, E.; Kuno, M.; Plashnitsa, V. V.; Robinson, R. D.; Ruoff, R. S.; Salahuddin, S.; Shan, J.; Shi, L.; Spencer, M. G.; Terrones, M.; Windl, W.; Goldberger, J. E. *ACS Nano* **2013,** 7, (4), 2898-2926.
9.	Castellanos-Gomez, A. *The Journal of Physical Chemistry Letters* **2015,** 6, (21), 4280-4291.
10.	Tran, V.; Soklaski, R.; Liang, Y.; Yang, L. *Physical Review B* **2014,** 89, (23), 235319.
11.	Li, L.; Yu, Y.; Ye, G. J.; Ge, Q.; Ou, X.; Wu, H.; Feng, D.; Chen, X. H.; Zhang, Y. *Nature nanotechnology* **2014,** 9, (5), 372-377.
12.	Yasaei, P.; Kumar, B.; Foroozan, T.; Wang, C.; Asadi, M.; Tuschel, D.; Indacochea, J. E.; Klie, R. F.; Salehi‐Khojin, A. *Advanced Materials* **2015,** 27, (11), 1887-1892.
13.	Lu, W.; Nan, H.; Hong, J.; Chen, Y.; Zhu, C.; Liang, Z.; Ma, X.; Ni, Z.; Jin, C.; Zhang, Z. *Nano Research* **2014,** 7, (6), 853-859.
14.	Radisavljevic, B.; Radenovic, A.; Brivio, J.; Giacometti, V.; Kis, A. *Nature Nanotechnology* **2011,** 6, (3), 147-150.
15.	Rodin, A. S.; Carvalho, A.; Castro Neto, A. H. *Physical Review Letters* **2014,** 112, (17), 176801.
16.	Peng, X.; Wei, Q.; Copple, A. *Physical Review B* **2014,** 90, (8), 085402.
17.	Fei, R.; Yang, L. *Nano Letters* **2014,** 14, (5), 2884-2889.
18.	Buscema, M.; Groenendijk, D. J.; Blanter, S. I.; Steele, G. A.; van der Zant, H. S. J.; Castellanos-Gomez, A. *Nano Letters* **2014**.
19.	Qiao, J.; Kong, X.; Hu, Z.-X.; Yang, F.; Ji, W. *Nature Communications* **2014,** 5.
20.	Reich, E. S. *Nature* **2014,** 506, (7486), 19-19.
21.	Churchill, H. O.; Jarillo-Herrero, P. *Nature nanotechnology* **2014,** 9, (5), 330-331.
22.	Jones, R. O. *Reviews of Modern Physics* **2015,** 87, (3), 897-923.
23.	Born, M.; Oppenheimer, R. *Annalen der Physik* **1927,** 389, (20), 457-484.
24.	Giustino, F., *Materials modelling using density functional theory: properties and predictions*. Oxford University Press: 2014.
25.	Dirac, P. A. In *The quantum theory of the electron*, Proceedings of the Royal Society of London A: Mathematical, Physical and Engineering Sciences, 1928; The Royal Society: pp 610-624.
26.	Hohenberg, P.; Kohn, W. *Physical Review* **1964,** 136, (3B), B864.
27.	Kohn, W.; Sham, L. J. *Physical Review* **1965,** 140, (4A), A1133.
28.	Perdew, J. P.; Ruzsinszky, A.; Tao, J.; Staroverov, V. N.; Scuseria, G. E.; Csonka, G. I. *The

Journal of Chemical Physics **2005,** 123, (6), 062201.

29.   Heyd, J.; Scuseria, G. E.; Ernzerhof, M. *The Journal of Chemical Physics* **2003,** 118, (18), 8207-8215.

30.   Kresse, G.; Furthmüller, J. *Computational Materials Science* **1996,** 6, (1), 15-50.

31.   Kresse, G.; Hafner, J. *Physical Review B* **1993,** 48, (17), 13115-13118.

32.   Soler, J. M.; Artacho, E.; Gale, J. D.; García, A.; Junquera, J.; Ordejón, P.; Sánchez-Portal, D. *Journal of Physics: Condensed Matter* **2002,** 14, (11), 2745.

33.   José, M. S.; Emilio, A.; Julian, D. G.; Alberto, G.; Javier, J.; Pablo, O.; Daniel, S.-P. *Journal of Physics: Condensed Matter* **2002,** 14, (11), 2745.

34.   Hamann, D. *Physical Review B* **1989,** 40, (5), 2980.

35.   Hamann, D.; Schlüter, M.; Chiang, C. *Physical Review Letters* **1979,** 43, (20), 1494.

36.   Laasonen, K.; Car, R.; Lee, C.; Vanderbilt, D. *Physical Review B* **1991,** 43, (8), 6796.

37.   Vanderbilt, D. *Physical Review B* **1990,** 41, (11), 7892.

38.   Born, M.; Huang, K., Dynamic Theory of Crystal Lattice, Clarendon. Oxford: 1954.

39.   Sólyom, J., *Fundamentals of the Physics of Solids: Volume 1: Structure and Dynamics.* Springer Science & Business Media: 2007; Vol. 1.

40.   Togo, A.; Oba, F.; Tanaka, I. *Physical Review B* **2008,** 78, (13), 134106.

41.   Hansen, J.-P.; Verlet, L. *physical Review* **1969,** 184, (1), 151.

42.   Kirkpatrick, S.; Gelatt, C. D.; Vecchi, M. P. *Science* **1983,** 220, (4598), 671-680.

43.   Pannetier, J.; Bassas-Alsina, J.; Rodriguez-Carvajal, J.; Caignaert, V. *Nature* **1990,** 346, (6282), 343-345.

44.   Amsler, M.; Goedecker, S. *The Journal of Chemical Physics* **2010,** 133, (22), 224104.

45.   Wales, D. J.; Doye, J. P. *The Journal of Physical Chemistry A* **1997,** 101, (28), 5111-5116.

46.   Laio, A.; Rodriguez-Fortea, A.; Gervasio, F. L.; Ceccarelli, M.; Parrinello, M. *The Journal of Physical Chemistry B* **2005,** 109, (14), 6714-6721.

47.   Woodley, S.; Battle, P.; Gale, J.; Catlow, C. A. *Physical Chemistry Chemical Physics* **1999,** 1, (10), 2535-2542.

48.   Abraham, N.; Probert, M. *Physical Review B* **2006,** 73, (22), 224104.

49.   Pickard, C. J.; Needs, R. *Journal of Physics: Condensed Matter* **2011,** 23, (5), 053201.

50.   Oganov, A. R.; Lyakhov, A. O.; Valle, M. *Accounts of Chemical Research* **2011,** 44, (3), 227-237.

51.   Wang, Y.; Lv, J.; Zhu, L.; Ma, Y. *Physical Review B* **2010,** 82, (9), 094116.

52.   Wang, Y.; Lv, J.; Zhu, L.; Ma, Y. *Computer Physics Communications* **2012,** 183, (10), 2063-2070.

53.   Wang, Y.; Miao, M.; Lv, J.; Zhu, L.; Yin, K.; Liu, H.; Ma, Y. *The Journal of Chemical Physics* **2012,** 137, (22), 224108.

54.   Eberhart, R. C.; Kennedy, J. In *A new optimizer using particle swarm theory*, Proceedings of the sixth international symposium on micro machine and human science, 1995; New York, NY: pp 39-43.

55.   Eberhart, R. C.; Shi, Y. In *Comparing inertia weights and constriction factors in particle swarm optimization*, Evolutionary Computation, 2000. Proceedings of the 2000 Congress on, 2000; IEEE: pp 84-88.

56.   Peng, F.; Miao, M.; Wang, H.; Li, Q.; Ma, Y. *Journal of the American Chemical Society* **2012,** 134, (45), 18599-18605.

57.   Luo, X.; Yang, J.; Liu, H.; Wu, X.; Wang, Y.; Ma, Y.; Wei, S.-H.; Gong, X.; Xiang, H. *Journal of the American Chemical Society* **2011,** 133, (40), 16285-16290.

58. Geim, A. K.; Novoselov, K. S. *Nature Materials* **2007,** 6, (3), 183-191.
59. Schwierz, F. *Nature nanotechnology* **2010,** 5, (7), 487-496.
60. Britnell, L.; Gorbachev, R.; Jalil, R.; Belle, B.; Schedin, F.; Mishchenko, A.; Georgiou, T.; Katsnelson, M.; Eaves, L.; Morozov, S. *Science* **2012,** 335, (6071), 947-950.
61. Dan, Y.; Lu, Y.; Kybert, N. J.; Luo, Z.; Johnson, A. C. *Nano Letters* **2009,** 9, (4), 1472-1475.
62. Stoller, M. D.; Park, S.; Zhu, Y.; An, J.; Ruoff, R. S. *Nano Letters* **2008,** 8, (10), 3498-3502.
63. Neto, A. C.; Guinea, F.; Peres, N.; Novoselov, K. S.; Geim, A. K. *Reviews of Modern Physics* **2009,** 81, (1), 109.
64. Novoselov, K.; Geim, A. K.; Morozov, S.; Jiang, D.; Katsnelson, M.; Grigorieva, I.; Dubonos, S.; Firsov, A. *Nature* **2005,** 438, (7065), 197-200.
65. Yu, Q.; Lian, J.; Siriponglert, S.; Li, H.; Chen, Y. P.; Pei, S.-S. *Applied Physics Letters* **2008,** 93, (11), 113103.
66. Reina, A.; Jia, X.; Ho, J.; Nezich, D.; Son, H.; Bulovic, V.; Dresselhaus, M. S.; Kong, J. *Nano Letters* **2008,** 9, (1), 30-35.
67. Zhang, Y.; Zhang, L.; Zhou, C. *Accounts of Chemical Research* **2013,** 46, (10), 2329-2339.
68. Kang, K.; Xie, S.; Huang, L.; Han, Y.; Huang, P. Y.; Mak, K. F.; Kim, C.-J.; Muller, D.; Park, J. *Nature* **2015,** 520, (7549), 656-660.
69. Choi, W.; Lahiri, I.; Seelaboyina, R.; Kang, Y. S. *Critical Reviews in Solid State and Materials Sciences* **2010,** 35, (1), 52-71.
70. Shao, Y.; Wang, J.; Wu, H.; Liu, J.; Aksay, I. A.; Lin, Y. *Electroanalysis* **2010,** 22, (10), 1027-1036.
71. Mattevi, C.; Kim, H.; Chhowalla, M. *Journal of Materials Chemistry* **2011,** 21, (10), 3324-3334.
72. Kara, A.; Enriquez, H.; Seitsonen, A. P.; Voon, L. L. Y.; Vizzini, S.; Aufray, B.; Oughaddou, H. *Surface Science Reports* **2012,** 67, (1), 1-18.
73. Vogt, P.; De Padova, P.; Quaresima, C.; Avila, J.; Frantzeskakis, E.; Asensio, M. C.; Resta, A.; Ealet, B.; Le Lay, G. *Physical Review Letters* **2012,** 108, (15), 155501.
74. Lalmi, B.; Oughaddou, H.; Enriquez, H.; Kara, A.; Vizzini, S.; Ealet, B.; Aufray, B. *Applied Physics Letters* **2010,** 97, (22), 223109.
75. Liu, C.-C.; Feng, W.; Yao, Y. *Physical Review Letters* **2011,** 107, (7), 076802.
76. Ezawa, M. *Physical Review Letters* **2012,** 109, (5), 055502.
77. Ezawa, M. *New Journal of Physics* **2012,** 14, (3), 033003.
78. Takeda, K.; Shiraishi, K. *Physical Review B* **1994,** 50, (20), 14916-14922.
79. Yukiko, Y.-T.; Rainer, F. *Science and Technology of Advanced Materials* **2014,** 15, (6), 064404.
80. Cahangirov, S.; Topsakal, M.; Aktürk, E.; Şahin, H.; Ciraci, S. *Physical Review Letters* **2009,** 102, (23), 236804.
81. Drummond, N. D.; Zólyomi, V.; Fal'ko, V. I. *Physical Review B* **2012,** 85, (7), 075423.
82. Jose, D.; Datta, A. *Accounts of Chemical Research* **2014,** 47, (2), 593-602.
83. Fleurence, A.; Friedlein, R.; Ozaki, T.; Kawai, H.; Wang, Y.; Yamada-Takamura, Y. *Physical Review Letters* **2012,** 108, (24), 245501.
84. Chiappe, D.; Scalise, E.; Cinquanta, E.; Grazianetti, C.; van den Broek, B.; Fanciulli, M.; Houssa, M.; Molle, A. *Advanced Materials* **2014,** 26, (13), 2096-2101.
85. Nijamudheen, A.; Bhattacharjee, R.; Choudhury, S.; Datta, A. *The Journal of Physical Chemistry C* **2015,** 119, (7), 3802-3809.

86.   Ni, Z.; Liu, Q.; Tang, K.; Zheng, J.; Zhou, J.; Qin, R.; Gao, Z.; Yu, D.; Lu, J. *Nano Letters* **2011,** 12, (1), 113-118.

87.   Derivaz, M.; Dentel, D.; Stephan, R. g.; Hanf, M.-C.; Mehdaoui, A.; Sonnet, P.; Pirri, C. *Nano Letters* **2015,** 15, (4), 2510-2516.

88.   Li, L.; Lu, S. z.; Pan, J.; Qin, Z.; Wang, Y. q.; Wang, Y.; Cao, G. y.; Du, S.; Gao, H. J. *Advanced Materials* **2014,** 26, (28), 4820-4824.

89.   Castro Neto, A. H.; Guinea, F.; Peres, N. M. R.; Novoselov, K. S.; Geim, A. K. *Reviews of Modern Physics* **2009,** 81, (1), 109-162.

90.   Novoselov, K. S.; Geim, A. K.; Morozov, S. V.; Jiang, D.; Zhang, Y.; Dubonos, S. V.; Grigorieva, I. V.; Firsov, A. A. *Science* **2004,** 306, (5696), 666-669.

91.   Tans, S. J.; Verschueren, A. R. M.; Dekker, C. *Nature* **1998,** 393, (6680), 49-52.

92.   Kosynkin, D. V.; Higginbotham, A. L.; Sinitskii, A.; Lomeda, J. R.; Dimiev, A.; Price, B. K.; Tour, J. M. *Nature* **2009,** 458, (7240), 872-876.

93.   Smalley, H. W. K. J. R. H. S. C. O. B. R. F. C. R. E. *Nature* **1985,** 318, 2.

94.   Diederich, F.; Kivala, M. *Advanced Materials* **2010,** 22, (7), 803-812.

95.   Diederich, F. *Nature* **1994,** 369, (6477), 199-207.

96.   Baughman, R. H.; Eckhardt, H.; Kertesz, M. *The Journal of Chemical Physics* **1987,** 87, (11), 6687-6699.

97.   Li, G.; Li, Y.; Liu, H.; Guo, Y.; Li, Y.; Zhu, D. *Chemical Communications* **2010,** 46, (19), 3256-3258.

98.   Malko, D.; Neiss, C.; Viñes, F.; Görling, A. *Physical Review Letters* **2012,** 108, (8), 086804.

99.   Zhang, H.; Liu, C.-X.; Qi, X.-L.; Dai, X.; Fang, Z.; Zhang, S.-C. *Nat Phys* **2009,** 5, (6), 438-442.

100.   Schlom, D. G.; Chen, L.-Q.; Eom, C.-B.; Rabe, K. M.; Streiffer, S. K.; Triscone, J.-M. *Annu. Rev. Mater. Res.* **2007,** 37, 589-626.

101.   Chen, A.; Bi, Z.; Jia, Q.; MacManus-Driscoll, J. L.; Wang, H. *Acta Materialia* **2013,** 61, (8), 2783-2792.

102.   Gui, G.; Li, J.; Zhong, J. *Physical Review B* **2008,** 78, (7), 075435.

103.   Choi, S.-M.; Jhi, S.-H.; Son, Y.-W. *Nano Letters* **2010,** 10, (9), 3486-3489.

104.   Pereira, V. M.; Castro Neto, A. H. *Physical Review Letters* **2009,** 103, (4), 046801.

105.   Kim, K. S.; Zhao, Y.; Jang, H.; Lee, S. Y.; Kim, J. M.; Kim, K. S.; Ahn, J.-H.; Kim, P.; Choi, J.-Y.; Hong, B. H. *Nature* **2009,** 457, (7230), 706-710.

106.   Hohenberg, P.; Kohn, W. *Physical Review* **1964,** 136, (3B), B864-B871.

107.   Dion, M.; Rydberg, H.; Schröder, E.; Langreth, D. C.; Lundqvist, B. I. *Physical Review Letters* **2004,** 92, (24), 246401.

108.   Román-Pérez, G.; Soler, J. M. *Physical Review Letters* **2009,** 103, (9), 096102.

109.   Monkhorst, H. J.; Pack, J. D. *Physical Review B* **1976,** 13, (12), 5188-5192.

110.   Kim, B. G.; Choi, H. J. *Physical Review B* **2012,** 86, (11), 115435.

111.   Wang, G.; Si, M.; Kumar, A.; Pandey, R. *Applied Physics Letters* **2014,** 104, (21), 213107.

112.   Trevisanutto, P. E.; Giorgetti, C.; Reining, L.; Ladisa, M.; Olevano, V. *Physical Review Letters* **2008,** 101, (22), 226405.

113.   Hwang, C.; Siegel, D. A.; Mo, S.-K.; Regan, W.; Ismach, A.; Zhang, Y.; Zettl, A.; Lanzara, A. *Scientific Reports* **2012,** 2.

114.   Marom, N.; Bernstein, J.; Garel, J.; Tkatchenko, A.; Joselevich, E.; Kronik, L.; Hod, O. *Physical Review Letters* **2010,** 105, (4), 046801.

115.   Pereira, V. M.; Castro Neto, A. H.; Peres, N. M. R. *Physical Review B* **2009,** 80, (4), 045401.

116.   Dóra, B.; Herbut, I. F.; Moessner, R. *Physical Review B* **2013,** 88, (7), 075126.
117.   Gomes, K. K.; Mar, W.; Ko, W.; Guinea, F.; Manoharan, H. C. *Nature* **2012,** 483, (7389), 306-310.
118.   Tarruell, L.; Greif, D.; Uehlinger, T.; Jotzu, G.; Esslinger, T. *Nature* **2012,** 483, (7389), 302-305.
119.   Wang, Y.; Ding, Y. *Solid State Communications* **2013,** 155, (0), 6-11.
120.   Castro, E. V.; Novoselov, K. S.; Morozov, S. V.; Peres, N. M. R.; dos Santos, J. M. B. L.; Nilsson, J.; Guinea, F.; Geim, A. K.; Neto, A. H. C. *Physical Review Letters* **2007,** 99, (21), 216802.
121.   Leenaerts, O.; Partoens, B.; Peeters, F. M. *Applied Physics Letters* **2013,** 103, (1), 013105.
122.   Zeinalipour-Yazdi, C. D.; Christofides, C. *Journal of Applied Physics* **2009,** 106, (5), 054318.
123.   Yue, Q.; Chang, S.; Kang, J.; Qin, S.; Li, J. *The Journal of Physical Chemistry C* **2013,** 117, (28), 14804-14811.
124.   Cranford, S. W.; Brommer, D. B.; Buehler, M. J. *Nanoscale* **2012,** 4, (24), 7797-7809.
125.   Lee, C.; Wei, X.; Kysar, J. W.; Hone, J. *Science* **2008,** 321, (5887), 385-388.
126.   Bellec, M.; Kuhl, U.; Montambaux, G.; Mortessagne, F. *Physical Review Letters* **2013,** 110, (3), 033902.
127.   Chen, Z.; Lin, Y.-M.; Rooks, M. J.; Avouris, P. *Physica E: Low-dimensional Systems and Nanostructures* **2007,** 40, (2), 228-232.
128.   Oostinga, J. B.; Heersche, H. B.; Liu, X.; Morpurgo, A. F.; Vandersypen, L. M. *Nature Materials* **2008,** 7, (2), 151-157.
129.   Ugeda, M. M.; Brihuega, I.; Hiebel, F.; Mallet, P.; Veuillen, J.-Y.; Gómez-Rodríguez, J. M.; Ynduráin, F. *Physical Review B* **2012,** 85, (12), 121402.
130.   Hashimoto, A.; Suenaga, K.; Gloter, A.; Urita, K.; Iijima, S. *Nature* **2004,** 430, (7002), 870-873.
131.   Lusk, M. T.; Carr, L. D. *Physical Review Letters* **2008,** 100, (17), 175503.
132.   Kotakoski, J.; Krasheninnikov, A. V.; Kaiser, U.; Meyer, J. C. *Physical Review Letters* **2011,** 106, (10), 105505.
133.   Banhart, F.; Kotakoski, J.; Krasheninnikov, A. V. *ACS Nano* **2010,** 5, (1), 26-41.
134.   Kulish, V. V.; Malyi, O. I.; Persson, C.; Wu, P. *Physical Chemistry Chemical Physics* **2015,** 17, (2), 992-1000.
135.   Khan, I.; Hong, J. *New Journal of Physics* **2015,** 17, (2), 023056.
136.   Little, E. J.; Jones, M. M. *Journal of Chemical Education* **1960,** 37, (5), 231.
137.   Perdew, J. P.; Burke, K.; Ernzerhof, M. *Physical Review Letters* **1996,** 77, (18), 3865-3868.
138.   Chan, K. T.; Neaton, J.; Cohen, M. L. *Physical Review B* **2008,** 77, (23), 235430.
139.   Ziletti, A.; Carvalho, A.; Campbell, D. K.; Coker, D. F.; Castro Neto, A. H. *Physical Review Letters* **2015,** 114, (4), 046801.
140.   Tersoff, J.; Hamann, D. R. *Physical Review Letters* **1983,** 50, (25), 1998-2001.
141.   Zhu, Z.; Guan, J.; Tománek, D. *Nano Letters* **2015,** 15, (9), 6042-6046.
142.   Wang, G.; Pandey, R.; Karna, S. P. *Applied Physics Letters* **2015,** 106, (17), 173104.
143.   Nakada, K.; Ishii, A. *Solid State Communications* **2011,** 151, (1), 13-16.
144.   Lehtinen, P. O.; Foster, A. S.; Ayuela, A.; Krasheninnikov, A.; Nordlund, K.; Nieminen, R. M. *Physical Review Letters* **2003,** 91, (1), 017202.
145.   Wu, M.; Liu, E.-Z.; Jiang, J. Z. *Applied Physics Letters* **2008,** 93, (8), 082504.
146.   Sivek, J.; Sahin, H.; Partoens, B.; Peeters, F. M. *Physical Review B* **2013,** 87, (8), 085444.
147.   Özçelik, V. O.; Ciraci, S. *The Journal of Physical Chemistry C* **2013,** 117, (49), 26305-

26315.

148.   Denis, P. A. *Physical Chemistry Chemical Physics* **2015**.

149.   He, H.; Pandey, R.; Pati, R.; Karna, S. P. *Physical Review B* **2006,** 73, (19), 195311.

150.   Gupta, S. K.; He, H.; Banyai, D.; Kandalam, A. K.; Pandey, R. *The Journal of Chemical Physics* **2013,** 139, (24), 244307.

151.   Sakhaee-Pour, A. *Computational Materials Science* **2009,** 45, (2), 266-270.

152.   Frank, O.; Tsoukleri, G.; Parthenios, J.; Papagelis, K.; Riaz, I.; Jalil, R.; Novoselov, K. S.; Galiotis, C. *ACS Nano* **2010,** 4, (6), 3131-3138.

153.   Mao, Y.; Wang, W. L.; Wei, D.; Kaxiras, E.; Sodroski, J. G. *ACS nano* **2011,** 5, (2), 1395-1400.

154.   Jiang, T.; Huang, R.; Zhu, Y. *Advanced Functional Materials* **2014,** 24, (3), 396-402.

155.   Kim, K.; Lee, Z.; Malone, B. D.; Chan, K. T.; Alemán, B.; Regan, W.; Gannett, W.; Crommie, M.; Cohen, M. L.; Zettl, A. *Physical Review B* **2011,** 83, (24), 245433.

156.   Coraux, J.; N'Diaye, A. T.; Busse, C.; Michely, T. *Nano Letters* **2008,** 8, (2), 565-570.

157.   Geringer, V.; Liebmann, M.; Echtermeyer, T.; Runte, S.; Schmidt, M.; Rückamp, R.; Lemme, M. C.; Morgenstern, M. *Physical Review Letters* **2009,** 102, (7), 076102.

158.   Zhu, W.; Low, T.; Perebeinos, V.; Bol, A. A.; Zhu, Y.; Yan, H.; Tersoff, J.; Avouris, P. *Nano Letters* **2012,** 12, (7), 3431-3436.

159.   Runte, S.; Lazić, P.; Vo-Van, C.; Coraux, J.; Zegenhagen, J.; Busse, C. *Physical Review B* **2014,** 89, (15), 155427.

160.   Zang, J.; Ryu, S.; Pugno, N.; Wang, Q.; Tu, Q.; Buehler, M. J.; Zhao, X. *Nature materials* **2013,** 12, (4), 321-325.

161.   Wood, J. D.; Wells, S. A.; Jariwala, D.; Chen, K.-S.; Cho, E.; Sangwan, V. K.; Liu, X.; Lauhon, L. J.; Marks, T. J.; Hersam, M. C. *Nano letters* **2014,** 14, (12), 6964-6970.

162.   Li, X.; Cai, W.; An, J.; Kim, S.; Nah, J.; Yang, D.; Piner, R.; Velamakanni, A.; Jung, I.; Tutuc, E. *Science* **2009,** 324, (5932), 1312-1314.

163.   Wang, M. C.; Chun, S.; Han, R. S.; Ashraf, A.; Kang, P.; Nam, S. *Nano Letters* **2015,** 15, (3), 1829-1835.

164.   Zhang, H. X.; Feng, P. X. *ACS Applied Materials & Interfaces* **2012,** 4, (1), 30-33.

165.   Brivio, J.; Alexander, D. T.; Kis, A. *Nano Letters* **2011,** 11, (12), 5148-5153.

166.   Jin Wu, J. *Nanotechnology* **2014,** 25, (35), 355402.

167.   Wei, Q.; Peng, X. *Applied Physics Letters* **2014,** 104, (25), 251915.

168.   Jiang, J.-W.; Rabczuk, T.; Park, H. S. *Nanoscale* **2015,** 7, (14), 6059-6068.

169.   Kou, L.; Ma, Y.; Smith, S. C.; Chen, C. *The Journal of Physical Chemistry Letters* **2015,** 6, (9), 1509-1513.

170.   Plimpton, S. *Journal of Computational Physics* **1995,** 117, (1), 1-19.

171.   Stillinger, F. H.; Weber, T. A. *Physical Review B* **1985,** 31, (8), 5262.

172.   Gaoxue, W.; Loh, G. C.; Ravindra, P.; Shashi, P. K. *Nanotechnology* **2016,** 27, (5), 055701.

173.   Humphrey, W.; Dalke, A.; Schulten, K. *Journal of Molecular Graphics* **1996,** 14, (1), 33-38.

174.   Timoshenko, S.; Woinowsky-Krieger, S.; Woinowsky-Krieger, S., *Theory of plates and shells*. McGraw-hill New York: 1959; Vol. 2.

175.   Liu, H.; Neal, A. T.; Zhu, Z.; Luo, Z.; Xu, X.; Tománek, D.; Ye, P. D. *ACS nano* **2014,** 8, (4), 4033-4041.

176.   Mehboudi, M.; Utt, K.; Terrones, H.; Harriss, E. O.; SanJuan, A. A. P.; Barraza-Lopez, S. *Proceedings of the National Academy of Sciences* **2015,** 112, (19), 5888-5892.

177. Castellanos-Gomez, A.; Vicarelli, L.; Prada, E.; Island, J. O.; Narasimha-Acharya, K.; Blanter, S. I.; Groenendijk, D. J.; Buscema, M.; Steele, G. A.; Alvarez, J. *2D Materials* **2014,** 1, (2), 025001.

178. Island, J. O.; Steele, G. A.; van der Zant, H. S.; Castellanos-Gomez, A. *2D Materials* **2015,** 2, (1), 011002.

179. Elias, D. C.; Nair, R. R.; Mohiuddin, T.; Morozov, S.; Blake, P.; Halsall, M.; Ferrari, A.; Boukhvalov, D.; Katsnelson, M.; Geim, A. *Science* **2009,** 323, (5914), 610-613.

180. Nair, R. R.; Ren, W.; Jalil, R.; Riaz, I.; Kravets, V. G.; Britnell, L.; Blake, P.; Schedin, F.; Mayorov, A. S.; Yuan, S. *Small* **2010,** 6, (24), 2877-2884.

181. Jeon, K.-J.; Lee, Z.; Pollak, E.; Moreschini, L.; Bostwick, A.; Park, C.-M.; Mendelsberg, R.; Radmilovic, V.; Kostecki, R.; Richardson, T. J. *ACS Nano* **2011,** 5, (2), 1042-1046.

182. Eda, G.; Chhowalla, M. *Advanced Materials* **2010,** 22, (22), 2392-2415.

183. Robinson, J. T.; Zalalutdinov, M.; Baldwin, J. W.; Snow, E. S.; Wei, Z.; Sheehan, P.; Houston, B. H. *Nano Letters* **2008,** 8, (10), 3441-3445.

184. Robinson, J. T.; Perkins, F. K.; Snow, E. S.; Wei, Z.; Sheehan, P. E. *Nano Letters* **2008,** 8, (10), 3137-3140.

185. Postnikov, A.; Pagès, O.; Hugel, J. *Physical Review B* **2005,** 71, (11), 115206.

186. Guan, J.; Zhu, Z.; Tománek, D. *arXiv preprint arXiv:1407.1894* **2014**.

187. Zhong, X.; Yap, Y. K.; Pandey, R.; Karna, S. P. *Physical Review B* **2011,** 83, (19), 193403.

188. Huang, B.; Xiang, H.; Xu, Q.; Wei, S.-H. *Physical Review Letters* **2013,** 110, (8), 085501.

189. Wang, G.; Pandey, R.; Karna, S. P. *Nanoscale* **2015,** 7, (2), 524-531.

190. Yan, H.; Xu, B.; Shi, S.; Ouyang, C. *Journal of Applied Physics* **2012,** 112, (10), 104316.

191. Ziletti, A.; Carvalho, A.; Campbell, D. K.; Coker, D. F.; Castro Neto, A. H. *Physical Review Letters* **2015,** 114, (4), 046801.

192. Dai, Y.; Ni, S.; Li, Z.; Yang, J. *Journal of Physics: Condensed Matter* **2013,** 25, (40), 405301.

193. Slough, W. J.; Kandalam, A. K.; Pandey, R. *The Journal of chemical physics* **2010,** 132, (10), 104304.

194. Wei, Q.; Peng, X. *Applied Physics Letters* **2014,** 104, (25), 251915.

195. Ito, J.; Nakamura, J.; Natori, A. *Journal of Applied Physics* **2008,** 103, (11), 113712.

196. Nguyen, M.-T.; Erni, R.; Passerone, D. *Physical Review B* **2012,** 86, (11), 115406.

197. Sahin, H.; Ciraci, S. *The Journal of Physical Chemistry C* **2012,** 116, (45), 24075-24083.

198. Hossain, M. Z.; Johns, J. E.; Bevan, K. H.; Karmel, H. J.; Liang, Y. T.; Yoshimoto, S.; Mukai, K.; Koitaya, T.; Yoshinobu, J.; Kawai, M. *Nature Chemistry* **2012,** 4, (4), 305-309.

199. Wei, Q.; Peng, X. *arXiv preprint arXiv:1403.7882* **2014**.

200. Misra, A.; Kalita, H.; Kottantharayil, A. *ACS Applied Materials & Interfaces* **2013,** 6, (2), 786-794.

201. Kumar, P. V.; Bernardi, M.; Grossman, J. C. *ACS nano* **2013,** 7, (2), 1638-1645.

202. Yau, S.-L.; Moffat, T. P.; Bard, A. J.; Zhang, Z.; Lerner, M. M. *Chemical Physics Letters* **1992,** 198, (3-4), 383-388.

203. Hanlon, D.; Backes, C.; Doherty, E.; Cucinotta, C. S.; Berner, N. C.; Boland, C.; Lee, K.; Harvey, A.; Lynch, P.; Gholamvand, Z. *Nature Communications* **2015,** 6.

204. Favron, A.; Gaufres, E.; Fossard, F.; Phaneuf-Lheureux, A.-L.; Tang, N. Y. W.; Levesque, P. L.; Loiseau, A.; Leonelli, R.; Francoeur, S.; Martel, R. *Nat Mater* **2015,** advance online publication.

205. Utt, K. L.; Rivero, P.; Mehboudi, M.; Harriss, E. O.; Borunda, M. F.; Pacheco SanJuan, A.

A.; Barraza-Lopez, S. *ACS Cent. Sci.,* **2015**, 1, (6), 320–327.

206.   Andres, C.-G.; Leonardo, V.; Elsa, P.; Joshua, O. I.; Narasimha-Acharya, K. L.; Sofya, I. B.; Dirk, J. G.; Michele, B.; Gary, A. S.; Alvarez, J. V.; Henny, W. Z.; Palacios, J. J.; Herre, S. J. v. d. Z. *2D Materials* **2014,** 1, (2), 025001.

207.   Sa, B.; Li, Y.-L.; Qi, J.; Ahuja, R.; Sun, Z. *The Journal of Physical Chemistry C* **2014**, 118, (46), 26560-26568.

208.   Zhu, Z.; Tománek, D. *Physical Review Letters* **2014,** 112, (17), 176802.

209.   Grimme, S. *Journal of Computational Chemistry* **2006,** 27, (15), 1787-1799.

210.   Nosé, S. *The Journal of Chemical Physics* **1984,** 81, (1), 511-519.

211.   Newsome, D. A.; Sengupta, D.; Foroutan, H.; Russo, M. F.; van Duin, A. C. *The Journal of Physical Chemistry C* **2012,** 116, (30), 16111-16121.

212.   Zandiatashbar, A.; Lee, G.-H.; An, S. J.; Lee, S.; Mathew, N.; Terrones, M.; Hayashi, T.; Picu, C. R.; Hone, J.; Koratkar, N. *Nat Commun* **2014,** 5, 3186 .

213.   Wang, G.; Slough, W. J.; Pandey, R.; Karna, S. P. *2D Materials* **2016,** 3, (2), 025011.

214.   Kang, J.; Wood, J. D.; Wells, S. A.; Lee, J.-H.; Liu, X.; Chen, K.-S.; Hersam, M. C. *ACS Nano* **2015,** 9, (4), 3596-3604.

215.   Young, D., *Computational chemistry: a practical guide for applying techniques to real world problems*. John Wiley & Sons: 2004.

216.   Henkelman, G.; Arnaldsson, A.; Jónsson, H. *Computational Materials Science* **2006,** 36, (3), 354-360.

217.   Ambrosetti, A.; Silvestrelli, P. L. *The Journal of Physical Chemistry C* **2011,** 115, (9), 3695-3702.

218.   Twarowski, A. *Combustion and flame* **1995,** 102, (1), 41-54.

219.   Carlsson, J. M.; Hanke, F.; Linic, S.; Scheffler, M. *Physical Review Letters* **2009,** 102, (16), 166104.

220.   Kuntz K L et al., **2015** Understanding the effect of oxygen and water on 2D black phosphorus oxidation from photoelectron spectroscopy Abstract in Int. Phosphorene Symp. (Lansing, USA,) (http://nanotube.pa.msu.edu/IPS15/IPS15abstracts.pdf).

221.   Hanlon, D.; Backes, C.; Doherty, E.; Cucinotta, C. S.; Berner, N. C.; Boland, C.; Lee, K.; Lynch, P.; Gholamvand, Z.; Harvey, A. *arXiv preprint arXiv:1501.01881* **2015**.

222.   Takao, Y.; Morita, A. *Physica B+ C* **1981,** 105, (1-3), 93-98.

223.   Xia, F.; Wang, H.; Jia, Y. *Nature Communications* **2014,** 5.

224.   Guan, J.; Zhu, Z.; Tománek, D. *Physical Review Letters* **2014,** 113, (4), 046804.

225.   Kamal, C.; Ezawa, M. *Physical Review B* **2015,** 91, (8), 085423.

226.   Zhang, Z.; Xie, J.; Yang, D.; Wang, Y.; Si, M.; Xue, D. *Applied Physics Express* **2015,** 8, (5), 055201.

227.   Jnawali, G.; Klein, C.; Wagner, T.; Hattab, H.; Zahl, P.; Acharya, D.; Sutter, P.; Lorke, A.; Horn-von Hoegen, M. *Physical Review Letters* **2012,** 108, (26), 266804.

228.   Wang, D.; Chen, L.; Liu, H.; Wang, X. *Journal of the Physical Society of Japan* **2013,** 82, (9), 094712.

229.   Chandra Shekar, S.; Swathi, R. S. *The Journal of Physical Chemistry C* **2014,** 118, (8), 4516-4528.

230.   Zhu, Z.; Guan, J.; Tománek, D. *Physical Review B* **2015,** 91, (16), 161404.

231.   Warschauer, D. *Journal of Applied Physics* **1963,** 34, (7), 1853-1860.

232.   Zhang, P.; Liu, Z.; Duan, W.; Liu, F.; Wu, J. *Physical Review B* **2012,** 85, (20), 201410.

233.   Zhang, S.; Yan, Z.; Li, Y.; Chen, Z.; Zeng, H. *Angewandte Chemie* **2015**.

234.   Kresse, G.; Joubert, D. *Physical Review B* **1999,** 59, (3), 1758-1775.

235.   Barrett, C.; Cucka, P.; Haefner, K. *Acta Crystallographica* **1963,** 16, (6), 451-453.

236.   Lazzeri, M.; Mauri, F. *Physical Review Letters* **2003,** 90, (3), 036401.

237.   Wang, G.; Pandey, R.; Karna, S. P. *ACS Applied Materials & Interfaces* **2015,** 7 (21), 11490–11496.

238.   Liang, J.; Cheng, L.; Zhang, J.; Liu, H. *arXiv preprint arXiv:1502.01610* **2015**.

239.   Kokubo, I.; Yoshiike, Y.; Nakatsuji, K.; Hirayama, H. *Physical Review B* **2015,** 91, (7), 075429.

240.   Ferrari, A. C. *Solid State Communications* **2007,** 143, (1), 47-57.

241.   Wang, X.; Kunc, K.; Loa, I.; Schwarz, U.; Syassen, K. *Physical Review B* **2006,** 74, (13), 134305.

242.   Rydberg, H.; Dion, M.; Jacobson, N.; Schröder, E.; Hyldgaard, P.; Simak, S. I.; Langreth, D. C.; Lundqvist, B. I. *Physical Review Letters* **2003,** 91, (12), 126402.

243.   Topsakal, M.; Ciraci, S. *Physical Review B* **2010,** 81, (2), 024107.

244.   Qin, R.; Wang, C.-H.; Zhu, W.; Zhang, Y. *Aip Advances* **2012,** 2, (2), 022159.

245.   Lu, Y.; Xu, W.; Zeng, M.; Yao, G.; Shen, L.; Yang, M.; Luo, Z.; Pan, F.; Wu, K.; Das, T. *Nano Letters* **2014,** 15, (1), 80-87.

246.   Scott, S.; Kral, M.; Brown, S. *Surface Science* **2005,** 587, (3), 175-184.

247.   Novoselov, K. S.; Geim, A. K.; Morozov, S.; Jiang, D.; Zhang, Y.; Dubonos, S. a.; Grigorieva, I.; Firsov, A. *Science* **2004,** 306, (5696), 666-669.

248.   Cahangirov, S.; Topsakal, M.; Aktürk, E.; Şahin, H.; Ciraci, S. *Physical Review Letters* **2009,** 102, (23), 236804.

249.   Zhang, S.; Yan, Z.; Li, Y.; Chen, Z.; Zeng, H. *Angewandte Chemie* **2015,** 127, (10), 3155-3158.

250.   Jones, D.; Stewart, A. *Philosophical Magazine B* **1982,** 46, (5), 423-434.

251.   Kuo, M.; May, P.; Gunn, A.; Ashfold, M.; Wild, R. *Diamond and Related Materials* **2000,** 9, (3), 1222-1227.

252.   Pearce, S.; May, P.; Wild, R.; Hallam, K.; Heard, P. *Diamond and Related Materials* **2002,** 11, (3), 1041-1046.

253.   Claeyssens, F.; Fuge, G.; Allan, N.; May, P.; Ashfold, M. *Dalton Transactions* **2004**, (19), 3085-3092.

254.   Hart, J. N.; May, P. W.; Allan, N. L.; Hallam, K. R.; Claeyssens, F.; Fuge, G. M.; Ruda, M.; Heard, P. J. *Journal of Solid State Chemistry* **2013,** 198, 466-474.

255.   Furlan, A.; Gueorguiev, G. K.; Czigány, Z.; Högberg, H.; Braun, S.; Stafström, S.; Hultman, L. *Physica Status Solidi (RRL)-Rapid Research Letters* **2008,** 2, (4), 191-193.

256.   Claeyssens, F.; Hart, J. N.; Allan, N. L.; Oliva, J. M. *Physical Review B* **2009,** 79, (13), 134115.

257.   Liu, B.; Köpf, M.; Abbas, A. N.; Wang, X.; Guo, Q.; Jia, Y.; Xia, F.; Weihrich, R.; Bachhuber, F.; Pielnhofer, F. *Advanced Materials* **2015,** 27, (30), 4423-4429.

258.   Kresse, G.; Furthmüller, J. *Physical Review B* **1996,** 54, (16), 11169-11186.

259.   Wang, G.; Pandey, R.; Karna, S. P. *Nanoscale* **2016,** 8, (16), 8819-8825.

260.   Zeinalipour-Yazdi, C. D.; Christofides, C. *Journal of Applied Physics* **2009,** 106, (5), 054318.

261.   Wei, Q.; Peng, X. *Applied Physics Letters* **2014,** 104, (25), 251915.

262.   Bardeen, J.; Shockley, W. *Physical Review* **1950,** 80, (1), 72.

263.   Bruzzone, S.; Fiori, G. *Applied Physics Letters* **2011,** 99, (22), 222108.

264.   Yoon, Y.; Ganapathi, K.; Salahuddin, S. *Nano Letters* **2011,** 11, (9), 3768-3773.

265.   Sun, J.; Zheng, G.; Lee, H.-W.; Liu, N.; Wang, H.; Yao, H.; Yang, W.; Cui, Y. *Nano Letters* **2014,** 14, (8), 4573-4580.

Appendix A

List of Related Publications

1. Gaoxue Wang, Ravindra Pandey*, Shashi P Karna, Physics and Chemistry of Oxidation of Two-dimensional Nanomaterials by Molecular Oxygen, Wiley Interdiscip. Rev.: Comput. Mol. Sci., in press (DOI: 10.1002/wcms.1280, review article).

2. Gaoxue Wang, Ravindra Pandey*, Shashi P Karna, Carbon Phosphide Monolayer: A Novel Two Dimensional Binary Material with Superior Carrier Mobility, Nanoscale, 2016, 8, 8819-8825.

3. Gaoxue Wang, William J Slough, Ravindra Pandey*, Shashi P Karna, Degradation of Phosphorene in Air: Understanding at Atomic Level, 2D Mater, 2016, 3, 025011.

4. Gaoxue Wang, G. C. Loh, Ravindra Pandey*, and Shashi P Karna, Out-of-plane Structural Flexibility of Phosphorene, Nanotechnology, 2016, 27, 055701.

5. Gaoxue Wang, Ravindra Pandey*, Shashi P Karna*, Atomically Thin Group-V Elemental Films: Theoretical Investigations of Antimonene Allotropes, ACS Appl. Mater. Interfaces, 2015, 7, 11490–11496.

6. Gaoxue Wang, Ravindra Pandey*, and Shashi P Karna, Effects of Extrinsic Point Defects in Phosphorene: B, C, N, O and F Adatoms, Appl. Phys. Lett., 2015, 106, 173104.

7. Gaoxue Wang, G. C. Loh, Ravindra Pandey*, Shashi P Karna, Novel Two-Dimensional Silica Monolayers with Tetrahedral and Octahedral Configurations, J. Phys. Chem. C, 2015, 119, 15654–15660.

8. Gaoxue Wang, Ravindra Pandey*, Shashi P Karna, Phosphorene Oxide: Stability and Electronic Properties of a Novel Two-dimensional Material, Nanoscale, 2015, 7, 524-531.

9. Gaoxue Wang, DZ Yang, ZY Zhang, MS Si*, Desheng Xue, Haiying He*, Ravindra Pandey, Decoding the Mechanism of the Mechanical Transfer of a GaN-based Heterostructure via an h-BN Release Layer in a Device Configuration, Appl. Phys. Lett., 2014, 105, 121605.

10. Gaoxue Wang, Mingsu Si, Ashok Kumar, Ravindra Pandey*, Strain Engineering of Dirac Cones in Graphyne, Appl. Phys. Lett., 2014, 104, 213107.

Appendix B

Permission for use of Figure 1.1 and Table 1.1

**NATURE PUBLISHING GROUP LICENSE
TERMS AND CONDITIONS**

Sep 23, 2016

This Agreement between Gaoxue Wang ("You") and Nature Publishing Group ("Nature Publishing Group") consists of your license details and the terms and conditions provided by Nature Publishing Group and Copyright Clearance Center.

License Number	3954810939875
License date	Sep 23, 2016
Licensed Content Publisher	Nature Publishing Group
Licensed Content Publication	Nature
Licensed Content Title	Van der Waals heterostructures
Licensed Content Author	A. K. Geim, I. V. Grigorieva
Licensed Content Date	Jul 24, 2013
Licensed Content Volume Number	499
Licensed Content Issue Number	7459
Type of Use	reuse in a dissertation / thesis
Requestor type	non-commercial (non-profit)
Format	print and electronic
Portion	figures/tables/illustrations
Number of figures/tables/illustrations	2
High-res required	no
Figures	Figure 1 and Figure 2
Author of this NPG article	no
Your reference number	
Title of your thesis / dissertation	FIRST-PRINCIPLES STUDIES OF GROUP IV AND GROUP V RELATED TWO DIMESIONAL MATERIALS
Expected completion date	Dec 2016
Estimated size (number of pages)	100
Requestor Location	Gaoxue Wang 2003 Woodmar Dr. Apt. D

Permission for use of Figure 1.2

Permission for use of Figure 2.1

Permission for use of Figure 2.3

Permission for use of Figure 2.6

Order Completed

Thank you for your order.

This Agreement between Gaoxue Wang ("You") and AIP Publishing LLC ("AIP Publishing LLC") consists of your license details and the terms and conditions provided by AIP Publishing LLC and Copyright Clearance Center.

Your confirmation email will contain your order number for future reference.

Get the printable license.
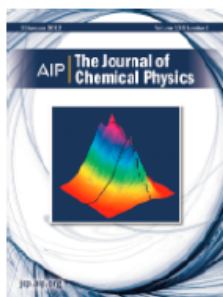
License Number	3956640252931
License date	Sep 26, 2016
Licensed Content Publisher	AIP Publishing LLC
Licensed Content Publication	Journal of Chemical Physics
Licensed Content Title	An effective structure prediction method for layered materials based on 2D particle swarm optimization algorithm
Licensed Content Author	Yanchao Wang, Maosheng Miao, Jian Lv, et al.
Licensed Content Date	Dec 12, 2012
Licensed Content Volume	137
Licensed Content Issue	22
Requestor type	Student
Format	Print and electronic
Portion	Figure/Table
Number of figures/tables	1
Requestor Location	Gaoxue Wang 2003 Woodmar Dr. Apt. D
	HOUGHTON, MI 49931 United States Attn: Gaoxue Wang
Billing Type	Invoice
Billing address	Gaoxue Wang 2003 Woodmar Dr. Apt. D
	HOUGHTON, MI 49931 United States Attn: Gaoxue Wang
Total	0.00 USD

Appendix C

Permission for use of materials in Chapter 3 and Chapter 4.2

Gaoxue Wang <gaoxuew@mtu.edu>
to rights

Sep 25 (4 days ago)

Dear sir or madam,

I would like to request the permission to reprint the following article for my Ph.D. thesis:

Appl. Phys. Lett. **106**, 173104 (2015).

I am the first author of the article.

Thanks for your time and assistance! I would really appreciate if you could grant me the permission.

Best regards,
Gaoxue Wang
Department of Physics
Michigan Technological University,
Houghton, MI 49931

Gaoxue Wang <gaoxuew@mtu.edu>
to rights

Sep 25 (4 days ago)

Dear sir or madam,

I would like to request the permission to reprint the following article for my Ph.D. thesis:

Appl. Phys. Lett. **104**, 213107 (2014).

AIPRights Permissions
to me

2:17 PM (32 minutes ago)

Dear Dr. Wang:

Thank you for requesting permission to reproduce material from AIP Publishing publications.

Material to be reproduced:

Appl. Phys. Lett. 104, 213107 (2014)
Appl. Phys. Lett. 106, 173104 (2015)

For use in the following manner:

Reproduced in your PhD thesis.

Permission is granted subject to these conditions:

1. AIP Publishing grants you non-exclusive world rights in all languages and media. This permission extends to all subsequent and future editions of the new work.

2. The following notice must appear with the material (please fill in the citation information):

"Reproduced from [FULL CITATION], with the permission of AIP Publishing."

When reusing a full article, the notice must be printed on the first page of the reprinted article or book chapter. When reusing figures, photographs, covers, or tables, the notice may appear in the caption, in a footnote, or in the reference list.

In cases where the new publication is licensed under a Creative Commons license, the full notice as stated above must appear with the reproduced material.

3. If the material is published in electronic format, we ask that a link be created pointing back to the abstract of the article on the journal website. This can be accomplished through the use of the article's DOI.
4. This permission does not apply to any materials credited to another source.

Please let us know if you have any questions.

Sincerely,
Susann Brailey
Manager, Rights & Permissions

Appendix D

Permission for use of materials in Chapter 4.3

Gaoxue Wang <gaoxuew@mtu.edu>   Sep 25 (3 days ago)

to permissions

Dear sir or madam,

I would like to request the permission to reprint the following article for my Ph.D. thesis:

Nanotechnology, 27, 055701 (2016).

I am the first author of the article.

Thanks for your time and assistance! I would really appreciate if you could grant me the permission.

Best regards,
Gaoxue Wang
Department of Physics
Michigan Technological University,
Houghton, MI 49931

Permissions   Sep 26 (2 days ago)

to me

Dear Gaoxue Wang,

Thank you for your email and for taking the time to seek this permission.

Regarding:

Gaoxue Wang et al 2016 Nanotechnology 27 055701

When you transferred the copyright in your article to IOP, we granted back to you certain rights, including the right to include the Final Published Version of the article within any thesis or dissertation. Please note you may need to obtain separate permission for any third party content you included within your article.

Please include citation details, "© IOP Publishing. Reproduced with permission. All rights reserved" and for online use, a link to the Version of Record.

The only restriction is that if, at a later date, your thesis were to be published commercially, further permission would be required.

Please let me know if you have any further questions.

In the meantime, I wish you the best of luck with the completion of your dissertation.

Kind regards,

Kathryn Shaw

Copyright & Permissions Team
Gemma Alaway – Rights & Permissions Adviser
Kathryn Shaw - Editorial Assistant

Contact Details
E-mail: permissions@iop.org

Appendix E

Permission for use of materials in Chapter 5.2

Gaoxue Wang <gaoxuew@mtu.edu   2:45 PM (17 hours ago)
to contracts-copy.

Dear sir or madam,

I would like to request the permission to reprint the following article for my Ph.D. thesis:

Nanoscale, 2015, 7, 524-531.

I am the first author of the article.

Thanks for your time and assistance! I would really appreciate if you could grant me the permission.

Best regards,
Gaoxue Wang
Department of Physics
Michigan Technological University,
Houghton, MI 49931

CONTRACTS-COPYRIGHT (shared) <Contracts-Copy   4:31 AM (3 hours ago)
to me

Dear Gaouxe,

As an author of the article you may reuse the figure(s) without seeking permission from the RSC. Please refer to the Rights Retained by Journals Authors on our website at http://www.rsc.org/AboutUs/Copyright/RightsRetainedbyJournalsauthors.asp. However, all cases of republication/reproduction must be accompanied by an acknowledgement of first publication of the Work by the RSC in the form:

(Original citation, including DOI link to the article on the Royal Society of Chemistry's website) – Reproduced by permission of The Royal Society of Chemistry

If you have any further queries do not hesitate to contact me.

Regards,

Antonella Tesoro
Customer Sales Support
Royal Society of Chemistry
Thomas Graham House,
Science Park, Milton Road,
Cambridge-CB4 0WF

Permission for use of materials in Chapter 5.3

Gaoxue Wang <gaoxuew@mtu.edu>   3:46 PM (16 hours ago)

to permissions

Dear sir or madam,

I would like to request the permission to reprint the following article for my Ph.D. thesis:

Gaoxue Wang et al., 2D Mater 2016, 3:025011.

I am the first author of the article.

Thanks for your time and assistance! I would really appreciate if you could grant me the permission.

Best regards,
Gaoxue Wang
Department of Physics
Michigan Technological University,
Houghton, MI 49931

Permissions   5:04 AM (2 hours ago)

to me

Dear Gaoxue Wang,

Thank you for your email and for taking the time to seek this permission.

Gaoxue Wang et al 2016 2D Mater. 3 025011

When you transferred the copyright in your article to IOP, we granted back to you certain rights, including the right to include the Final Published Versionof the article within any thesis or dissertation. Please note you may need to obtain separate permission for any third party content you included within your article.

Please include citation details, "© IOP Publishing. Reproduced with permission. All rights reserved" and for online use, a link to the Version of Record.

The only restriction is that if, at a later date, your thesis were to be published commercially, further permission would be required.

In regards to your queries to reuse Applied Physics Letters content, please note that the publisher of this journal is the American Institute of Physics (AIP) rather than the Institute of Physics (IOP). Therefore, you will need to contact the AIP.

Please let me know if you have any further questions.

In the meantime, I wish you the best of luck with the completion of your dissertation.

Kind regards,

Kathryn Shaw

Copyright & Permissions Team
Gemma Alaway – Rights & Permissions Adviser
Kathryn Shaw - Editorial Assistant

Appendix F

Permission for use of materials in Chapter 6

Copyright Clearance Center **RightsLink®**

Home | Create Account | Help

ACS Publications Most Trusted. Most Cited. Most Read.

Title: Atomically Thin Group V Elemental Films: Theoretical Investigations of Antimonene Allotropes

Author: Gaoxue Wang, Ravindra Pandey, Shashi P. Karna

Publication: Applied Materials

Publisher: American Chemical Society

Date: Jun 1, 2015

Copyright © 2015, American Chemical Society

LOGIN

If you're a copyright.com user, you can login to RightsLink using your copyright.com credentials. Already **a RightsLink user** or want to learn more?

PERMISSION/LICENSE IS GRANTED FOR YOUR ORDER AT NO CHARGE

This type of permission/license, instead of the standard Terms & Conditions, is sent to you because no fee is being charged for your order. Please note the following:

- Permission is granted for your request in both print and electronic formats, and translations.
- If figures and/or tables were requested, they may be adapted or used in part.
- Please print this page for your records and send a copy of it to your publisher/graduate school.
- Appropriate credit for the requested material should be given as follows: "Reprinted (adapted) with permission from (COMPLETE REFERENCE CITATION). Copyright (YEAR) American Chemical Society." Insert appropriate information in place of the capitalized words.
- One-time permission is granted only for the use specified in your request. No additional uses are granted (such as derivative works or other editions). For any other uses, please submit a new request.

137

Appendix G

Permission for use of materials in Chapter 7

Gaoxue Wang <gaoxuew@mtu.edu>   8:09 AM (7 hours ago)

to contracts-copy.

Dear sir or madam,

I would like to request the permission to reprint the following article for my Ph.D. thesis:

Nanoscale, 2016, **8**, 8819-8825

I am the first author of the article.

Thanks for your time and assistance! I would really appreciate if you could grant me the permission.

Best regards,
Gaoxue Wang
Department of Physics
Michigan Technological University,
Houghton, MI 49931

CONTRACTS-COPYRIGHT (shared) <Contracts-Copyright@rsc.org>   9:59 AM (5 hours ago)

to me

Dear Gaoxue,

The Royal Society of Chemistry (RSC) hereby grants permission for the use of your paper(s) specified below in the printed and microfilm version of your thesis. You may also make available the PDF version of your paper(s) that the RSC sent to the corresponding author(s) of your paper(s) upon publication of the paper(s) in the following ways: in your thesis via any website that your university may have for the deposition of theses, via your university's Intranet or via your own personal website. We are however unable to grant you permission to include the PDF version of the paper(s) on its own in your institutional repository. The Royal Society of Chemistry is a signatory to the STM Guidelines on Permissions (available on request).

Please note that if the material specified below or any part of it appears with credit or acknowledgement to a third party then you must also secure permission from that third party before reproducing that material.

Please ensure that the thesis states the following:
Reproduced by permission of The Royal Society of Chemistry
and include a link to the paper on the Royal Society of Chemistry's website.

Please ensure that your co-authors are aware that you are including the paper in your thesis.

Regards,

Antonella Tesoro

Customer Sales Support

Royal Society of Chemistry

Thomas Graham House,

Science Park, Milton Road,

Cambridge-CB4 0WF